Universidade de Brasília
Instituto de Geociências
Programa de Pós-Graduação em Geociências Aplicadas e Geodinâmica

Tomografia de velocidade de grupo de ondas Rayleigh na América do Sul

André Vinícius de Sousa Nascimento

Dissertação de Mestrado N° 165

Orientador
Prof. Dr. George Sand Leão Araújo de França

Brasília
2019

Universidade de Brasília — UnB
Instituto de Geociências
Programa de Pós-Graduação em Geociências Aplicadas e Geodinâmica

Banca examinadora:

Prof. Dr. George Sand Leão Araújo de França (Orientador) — IG/UnB
Prof. Dr. Marcelo Peres Rocha — IG/UnB
Prof. Dr. Paulo Araújo de Azevedo — IEG/UFOPA

Nascimento, André Vinícius de Sousa.

Tomografia de velocidade de grupo de ondas Rayleigh na América do Sul / André Vinícius de Sousa Nascimento. Brasília : UnB, 2019.
92 p. : il. ; 29,5 cm.

Dissertação (Mestrado) — Universidade de Brasília, Brasília, 2019.

1. ondas Rayleigh, 2. inversão, 3. *Fast Marching Method*,
4. sismicidade intraplaca, 5. Bloco Paleocontinental São Francisco,
6. Bloco Paranapanema

Endereço: Universidade de Brasília
Campus Universitário Darcy Ribeiro — Asa Norte
CEP 70910-900
Brasília–DF — Brasil

Universidade de Brasília
Instituto de Geociências
Programa de Pós-Graduação em Geociências Aplicadas e Geodinâmica

Tomografia de velocidade de grupo de ondas Rayleigh na América do Sul

André Vinícius de Sousa Nascimento

Dissertação apresentada ao Instituto de Geociências da
Universidade de Brasília como requisito parcial para a obtenção
do título de Mestre em Ciências.
Área de concentração: Geofísica Aplicada

Prof. Dr. George Sand Leão Araújo de França (Orientador)
IG/UnB

Prof. Dr. Marcelo Peres Rocha
IG/UnB

Prof. Dr. Paulo Araújo de Azevedo
IEG/UFOPA

Brasília, 17 de julho de 2019

"By striving to do the impossible, man has always achieved what is possible. Those who have cautiously done no more than they believed possible have never taken a single step forward."

Mikhail Bakunin

Agradecimentos

Gostaria de agradecer ao meu orientador, George Sand França, pela amizade e pela confiança, e por vir acompanhando minha carreira científica desde que eu entrei no Observatório Sismológico como bolsista, durante a graduação. Agradeço por tudo que aprendi durante o mestrado, especialmente na parte de programação.

Aos meus pais, Joaquim e Joana, por todo o apoio e incentivo para que eu chegasse até aqui e pudesse ter um bom futuro. Ao meu irmão Fábio pelo companheirismo.

Agradeço aos meus amigos pelo suporte e por vários momentos de descontração, evitando em diversas ocasiões que eu colapsasse: Jorge, Glaucia, Isabele, Vitória, Matheus Canedo, Matheus Cunha, Isaac, Alice, Aline, Rayssa, *et al.*

I would like to thank Robert Herrmann for the Computer Programs in Seismology, which allowed our group velocity measurements and Nick Rawlinson for the surface wave tomography code. Yury Kashnitsky should also be thanked for heading the mlcourse.ai, an amazing machine learning course that completely changed the way I deal with data analysis.

Ao Observatório Sismológico da Universidade de Brasília e seus funcionários, que sempre me acolheram de braços abertos.

Aos membros da banca, professores Marcelo Rocha e Paulo Azevedo, pelas valiosas sugestões para aprimorar o texto.

Ao professor Marcelo Assumpção, por permitir que nós utilizássemos dados do seu projeto, relativo à região das bacias do Paraná, Chaco-Paraná e Pantanal.

À CAPES pelo auxílio financeiro, por meio da concessão de uma bolsa de estudos.

Resumo

Baseado em novos dados de redes permanentes e temporárias, nós apresentamos novas imagens tomográficas da América do Sul, construídas a partir da inversão de velocidade de grupo do modo fundamental de ondas Rayleigh. Uma combinação iterativa do *Fast Marching Method* para resolver o problema direto com um método de subespaço para resolver o problema inverso leva em consideração a não-linearidade do problema tomográfico e foi usada para construir mapas de velocidade de grupo dentro do intervalo de períodos de 10 a 150 s. Um máximo de $\sim$ 17000 medidas foram obtidas em 30 s de período e dados de 282 estações foram empregados. A resolução lateral do nosso modelo foi avaliada por meio de testes sintéticos de tabuleiro, onde o tamanho das anomalias foi variado de 2° x 2° a 4° x 4° em cada teste. Esses testes mostraram que as anomalias de velocidade sintéticas foram em geral bem recuperadas, apesar de existir alguma perda de amplitude e efeitos de alongamento de anomalias em algumas partes do modelo, provavelmente causadas pela inclusão de termos de regularização durante a inversão e pela ausência de estações em algumas áreas, respectivamente. Nos nossos resultados, há uma grande correlação entre os mapas de período curto e a geologia de superfície, onde regiões de embasamento exposto estão relacionadas a altas velocidades e bacias sedimentares apresentam baixas velocidades. Períodos longos amostram profundidades litosféricas e revelaram que áreas cratônicas antigas e estáveis da América do Sul, como os Crátons Amazônico e São Francisco, se correlacionam bem com altas velocidades. Nós também propusemos limites para o Bloco Paleocontinental São Francisco e para o Bloco Paranapanema com base nos nossos mapas de 100 e 150 s de período, que são consistentes com anomalias gravimétricas e com os limites recentemente propostos por Rocha et al., baseados em tomografia de ondas de corpo. Várias anomalias de baixa velocidade são consistentes com regiões de concentração de sismicidade intraplaca na Plataforma Sul-Americana, incluindo a Zona Sísmica Goiás-Tocantins, a Bacia do Pantanal e a Província Borborema, o que sugere que o afinamento litosférico pode ser uma causa importante da sismicidade intraplaca.

Palavras-chave: ondas Rayleigh, inversão, *Fast Marching Method*, sismicidade intraplaca, Bloco Paleocontinental São Francisco, Bloco Paranapanema

Abstract

Based on new data from permanent and temporary networks, we present new tomographic images of the South American continent, constructed from inversion of fundamental mode group velocities of Rayleigh waves. An iterative combination of the Fast Marching Method to solve the direct step with a subspace method to solve the inverse step takes into account the nonlinearity of the tomographic problem and is used to obtain group velocity maps in the period range 10-150 s. A maximum of $\sim$ 17000 measurements was achieved at 30 s period and data from 282 stations were employed. The lateral resolution of our model is assessed by synthetic checkerboard tests, where the size of the anomalies is varied from 2° x 2° to 4° x 4° in each test. Those tests showed that the synthetic velocity anomalies were generally well recovered, despite the presence of some amplitude loss and smearing effects in some portions of the model, probably caused by the inclusion of regularization terms and areas devoid of stations, respectively. In our results, there is a great correlation between short period maps and surface geology, where regions of exposed basement are related to high velocities, while sedimentary basins present low velocities. Long period maps sample lithospheric depths, revealing that old and stable cratonic areas of South America, such as the Amazonian and São Francisco Cratons, correlate well with high velocities. Limits for the São Francisco Paleocontinental Block and for the Paranapanema Block are also proposed based on our 100 and 150 s period maps and are consistent with gravity anomalies and with the limits recently proposed by Rocha et al., derived from body wave tomography. Several low-velocity anomalies are consistent with regions of concentration of intraplate seismicity in the South American Platform, including the Goiás-Tocantins Seismic Zone, the Pantanal Basin and the Borborema Province, which suggests that lithospheric thinning plays a key role on intraplate seismicity.

Keywords: Rayleigh waves, inversion, Fast Marching Method, intraplate seismicity, São Francisco Paleocontinental Block, Paranapanema Block

Contents

List of Figures

List of Tables

Chapter 1

Introduction

Due to limitations in technology, it isn't possible to directly study the Earth's deep interior yet. Therefore, we have to rely on indirect methods to do so. Amongst the geophysical techniques that can provide subsurface information, seismology is one of the most powerful and has a wide range of applications, such as hydrocarbon detection (e.g., Khattri et al., 1979, Zouaghi et al., 2009); fault geometry (e.g., Braunmiller and Nábělek, 1996), crustal thickness and lithospheric discontinuities (e.g., Liu et al., 2003; França and Assumpção, 2004; Heit et al., 2007), and seismic imaging ranging from a scale of meters to thousands of kilometers (e.g., Aki et al., 1977; Rawlinson et al., 2011; Fang et al., 2015).

Since the late 1970s, the branch of seismology known as seismic tomography has been applied at several scales (local to global) to produce images of seismic velocities of the subsurface. Even though the foundation of geophysical data inversion was established by the beginning of the 1970s (e.g., Backus and Gilbert, 1967; Backus and Gilbert, 1970; Wiggins, 1972), early publications concerning inverting travel time data of earthquakes to obtain velocity structure were published only by 1977 (Aki et al., 1977). Since then, seismic tomography gained worldwide popularity and has been applied to map wavespeeds underneath North America (e.g., Van der Lee and Nolet, 1997; Yuan and Romanowicz, 2010; Sigloch, 2011), South America (e.g., VanDecar et al., 1995; Feng et al., 2007; Rocha et al., 2011), Europe (e.g., Goes et al., 2000; Zhu et al., 2012), Asia (e.g., Feng and An, 2010, Matsubara et al., 2008) and Australia (e.g., Saygin and Kennett, 2010; Rawlinson et al., 2011; Saygin and Kennett, 2012).

South America underwent a complex geological evolution, such that its present geological and geographical configuration is the result of a long series of Wilsonian orogenic cycles. To better understand the tectonic evolution of a continent, it is necessary to grasp its structure in the present, at both shallow and deep scales. In this context, seismological methods, and especially seismic tomography provide the best means for indirectly studying the Earth's deep interior.

When compared to other continents such as North America or Europe, seismic station coverage in South America is rather scarce, especially in regions with low population density or hard to access, such as the Amazon rainforest. This scarceness leads to limitations in seismological models representing the continent, where small scale structures may not be retrieved. However, previous surface wave tomography studies in South America (e.g., Silveira et al., 1998; Vdovin et al., 1999; Van der Lee et al., 2001; Feng et al., 2004; Heintz et al., 2005; Feng et al., 2007), relying on data from stations of the permanent global network and/or stations of temporary networks, have successfully mapped most regional large scale features and obtained the best possible models with the data available at the time. Those studies tend to agree on the large scale structures, such as high seismic velocities beneath cratons, but they differ in terms of resolution and consequently smaller scale features tend to disagree due to distinct datasets and inversion schemes.

New data can improve previous seismic tomography results, reveal smaller-scale features that haven't been imaged before, and increase model resolution. From 2011 to 2014 several new stations have been deployed in Brazil by the following institutions: University of São Paulo (USP), University of Brasília (UnB), University of Rio Grande do Norte (UFRN) and National Observatory (ON). Those stations constitute the Brazilian Seismographic Network (RSBR), which comprises four sub-networks: BL (USP), BR (UnB), NB (UFRN), ON (ON) (Bianchi et al., 2018). Besides earthquake location in Brazil, data from the RSBR can be used in studies concerning the Earth's subsurface beneath South America, providing models with better resolution than previous works, especially in regions with previous little monitoring, such as the Amazon rainforest. A new project named 3-Basin project, funded by São Paulo State Research Foundation, also allowed the deployment of several new temporary seismic stations in the region of the Paraná, Chaco-Paraná and Pantanal basins. Those stations comprise the XC network and significantly improve coverage in southwestern South American Platform.

Based on the new data and on an iterative inversion scheme of surface waves that allows the nonlinearity of the tomographic problem to be taken into account, our objective is to generate a better constrained model that represents the deep structure of the South American continent. More specifically, we use a denser path coverage (our maximum number of group velocity measurements is nearly three times larger than the one of the previous study by Feng et al. (2004, 2007)), allowed by the new data, to produce group velocity lateral variation maps of Rayleigh waves in the period range 10-150 s. Those maps are then interpreted in terms of the main aspects of the lithosphere of South America, such as its cratonic blocks and intraplate seismicity. Chapter 2 presents a literature review, which aims to provide the reader with the state of the art of the subject; it includes a review of the geological setting of South America - a continent that can be roughly divided into the South American Platform (a stable portion), the Andean orogeny and the Patagonian block -, basic concepts of the seismological theory and the main previous tomographic studies of the South American continent. Chapters 3 and 4 describe the methodology applied to achieve Rayleigh wave group velocity maps: the former chapter is focused on data processing while the latter chapter explains the inversion scheme adopted. Chapter 5 presents an article with our results and discussion.

Chapter 2

Literature review

2.1 Introduction

In this chapter, a brief review of the state of the art knowledge concerning the South American continent is provided. This continent has a complex structural framework and geological history, which is discussed in Section 2.2. Section 2.3 describes some of the foundations of seismological theory on which surface wave tomography is built upon, except for the inversion theory, for which an entire chapter is dedicated (Chapter 4). Finally, in Section 2.4, we summarize studies from several researchers about seismic tomography history and the main lithospheric structure results in South America derived from seismic tomography.

2.2 Regional geology

In tectonic terms, the lithosphere of South America can be roughly divided into a relatively stable portion — the South American Platform, which occupies most of the territory of the continent — that is not affected by the Andean and Caribbean orogeneses and is surrounded by them; the Andean Phanerozoic Fold Belt on the west and north; and the Patagonian block, a microcontinent with evolution independent from the rest of South America, located on its southern portion and bounded by the Andes on the west and by the Atlantic Ocean on the east.

2.2.1 South American Platform

Almeida et al. (2000) define the South American Platform as the stable portion of the homonym plate that is relatively not affected by the Andean and Caribbean orogeneses. Besides relative stability compared to the surrounding mobile belts, a Platform is usually characterized for antiquity - because its basement is mainly composed of Archean and Proterozoic rocks — and transitority — because of its long tectonic evolution (Almeida et al., 2000).

Throughout geological time the lithosphere of South America has been deformed and rearranged several times by Global Plate Tectonics processes, and the basement of the continent is the result of a long evolution. More specifically, the basement of the continent can be considered the product of three main orogenic events: (i) the Trans-Amazonian, during the Paleoproterozoic; (ii) the Late Mesoproterozoic and (iii) the Brasiliano/Pan African, mainly in Neoproterozoic times. The lack of data makes it difficult to determine cycles for the Archean yet (Almeida et al., 2000). Although of secondary importance to the Amazonian Craton and surroundings (Brito Neves and Fuck, 2013), the Brasiliano events resulted in the present configuration of the tectonic elements in the South America Platform, and the youngest fold belts of the basement were formed during the Neoproterozoic (Almeida et al., 2000). Those fold belts have stabilized during the Ordovician (440 Ma) and it can be said that the South American Platform is an entity of the Ordovician, but only got individualized as such during the Cretaceous, with separation between Africa and South America (Hasui, 2012). The basement of the South American Platform is exposed in three shields (Figure 2.1): Guyana and Central Brazil shields, located north and south to the Amazonian Basin, respectively, and the Atlantic shield, in central-eastern Brazil. Figure 2.1 also shows areas of Phanerozoic cover across the Platform.

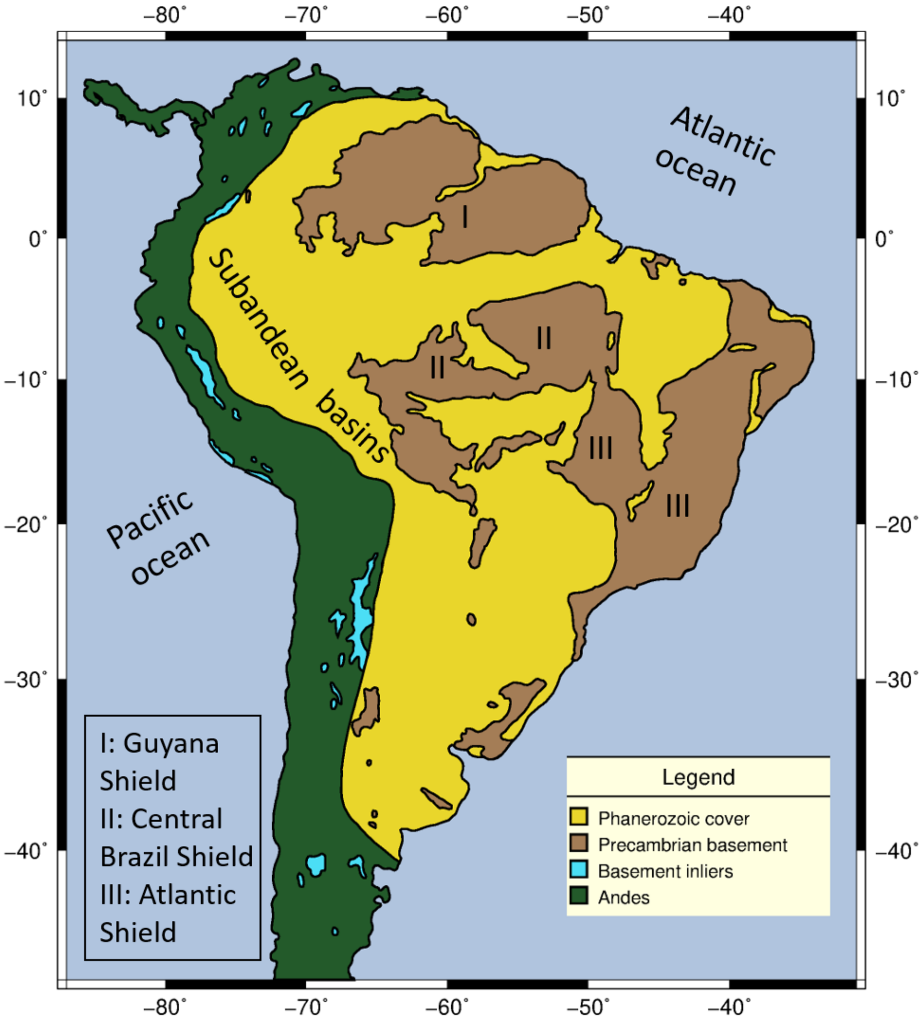

Figure 2.1: Map of exposed Precambrian basement regions and Phanerozoic sedimentary cover of the South American Platform. The basement is exposed along three shields: Guyana and Central Brazil shields, located north and south to the Amazonian Basin, respectively, and Atlantic shield, in central-eastern Brazil. Modified from Almeida et al. (1981).

Due to a distinct tectonic evolution, the basement of the South American Platform can be divided into two main domains: a pre-Brasiliano N-NW Amazonian Domain, where large Archean nuclei are circumscribed by younger Paleo- and Mesoproterozoic mobile belts; and a central-eastern "Brasiliano" Domain, whose structural framework was intensely shaped by Neoproterozoic orogenic cycles, namely the Brasiliano/Pan African events (Brito Neves and Fuck, 2014), that were diachronous and distributed over four pulses: i) ca. 800 - 740 Ma, ii) ca. 660 - 610 Ma, iii) ca. 590 - 560 Ma and iv) 520-500 Ma (Brito Neves et al., 2014). Another contribution by Brito Neves and Fuck (2014) is the recognition that the crustal evolution of the Amazonian Domain share many similarities with the ancient Laurentian continent, while the Brasiliano Domain presents affinities with western Gondwana. Those domains are separated by a megashear zone named Transbrasiliano Lineament (TBL), which extends even further to Africa (e.g, Santos et al., 2008), to the south and by the Araguaia Fold Belt to the north (Brito Neves and Fuck, 2014). Figure 2.2 is a map of the main geotectonic features of South America.

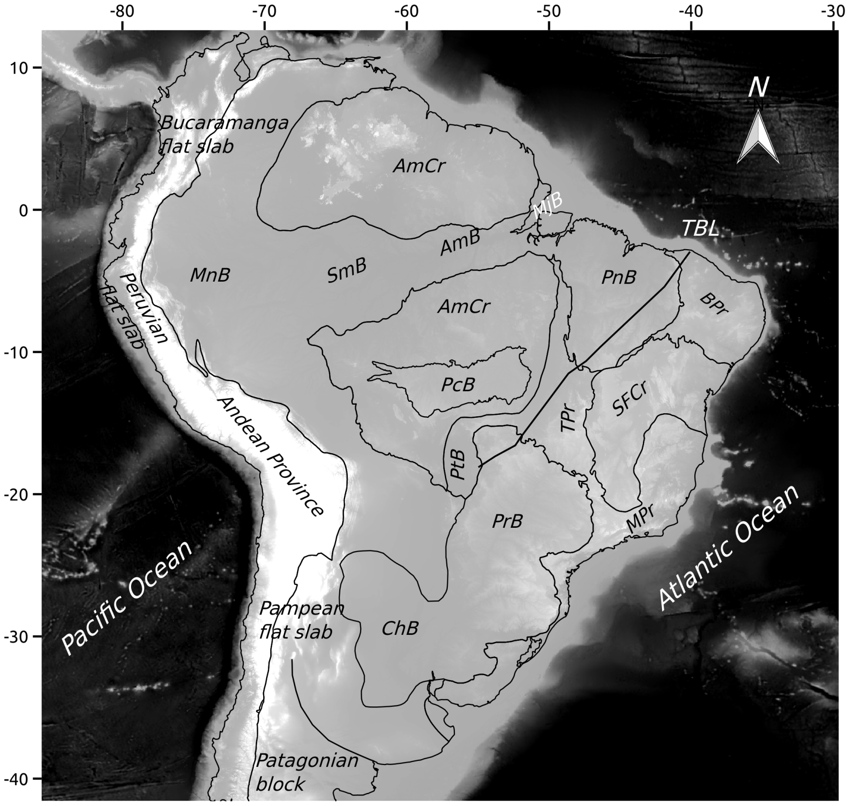

Figure 2.2: Main geotectonic provinces of South America. The solid black contours represent: AmCr - Amazonian Craton, SFCr - São Francisco Craton, BPr - Borborema Province, TPr - Tocantins Province, MPr - Mantiqueira Province, PnB - Parnaíba Basin, PrB - Paraná Basin, ChB - Chaco Basin, PtB - Pantanal Basin, PcB - Parecis Basin, MnB - Maranon Basin, SmB - Solimões Basin, AmB - Amazon Basin and MjB - Marajó Basin. TBL stands for the Transbrasiliano Lineament.

Almeida et al. (1977, 1981) made the first proposal of division of the Brazilian territory in structural provinces. Ten provinces were recognized (see Figure 2.2 for a spatial reference):

- Rio Branco (included in the Guyana Shield), Tapajós (part of the Central Brazilian Shield) and São Francisco provinces, corresponding to the cratonic areas;
- Borborema, Mantiqueira and Tocantins provinces, corresponding to Neoproterozoic orogens;
- Amazon, Paraná and Parnaíba provinces, corresponding to large Paleozoic sedimentary basins. The Amazon province includes both Amazon and Solimões Basins;
- A province corresponding to small coastal sedimentary basins.

With new geochronological and geological data available, finer subdivisions have been proposed. In particular, the Brazilian Geological Survey (CPRM) (Schobbenhaus and Brito Neves, 2003; Santos, 2003) added a Parecis province to the previously mentioned division, corresponding to the namesake basin, and divided the Amazonian Craton in seven provinces: Transamazonas (2.25 - 2.0 Ga), Carajás (3.1 - 2.53 Ga), Amazônia Central (2.6 - 1.7 Ga), Tapajós-Parima (2.1 - 1.87 Ga), Rondônia-Juruena (1.81 - 1.52 Ga), Rio Negro (1.86 - 1.52 Ga) and Sunsás (1.45 - 0.99 Ga). Because new data are always being produced, new interpretations are always being proposed and there is no absolute consensus about those subdivisions.

2.2.2 Andes

Developed along the western margin of South America, the Andes are the largest orogenic system resulting from a non-collisional environment in the world, extending more than 8000 km. The Andean mountain range is a consequence of several processes related to the subduction of Nazca plate beneath the South American plate. Gansser (1973) provided the first proposal of division for the Andes, under the plate tectonics concept, in northern, central and southern Andes (see Figure 2.3). Northern and Southern Andes are characterized by an expressive occurrence of ophiolitic rocks, together with metamorphic rocks of the Jurassic and Cretaceous (Ramos, 1999; Ramos, 2009). Central Andes, on the other hand, lack those rocks and represent the Andean-type orogen (Ramos, 1999) of the classification of Dewey and Bird (1970).

An astonishing feature is the varying geometry of the Nazca slab beneath the Andes, where there are segments with flat-slab subduction (subhorizontal Wadati-Benioff zone) and segments with "normal" subduction, dipping around 30°-40°. From north to south, these flat-slab segments are:

- *Bucaramanga segment*: located in northern Colombia, north of 5°N, first identified by Pennington (1981);
- *Peruvian segment*: located between 5°S and 14°S;
- *Pampean segment*: located between 27°S and 33°S. Barazangi and Isacks (1976, 1979) first identified the Peruvian and Pampean segments.

Figure 2.3: Schematic map of the Andes, showing the Bucaramanga, Peruvian and Pampean flat-slab segments. Figure extracted from Ramos (2009)

2.2.3 Patagonian block

Patagonia is a mass of land separated from the rest of the South American continent by a major fault and can be defined as the portion of the Terra Australis orogen (Cawood, 2005) in the continent that was not affected by Andean orogeny (Hasui, 2012). The basement of Patagonia can be divided into two massifs: Somún Cura and Deseado, with granitoids ranging from Neoproterozoic to early Paleozoic ages (e.g., Pankhurst et al., 2003). We won't discuss the Patagonian block any further due to its limited resolution in our model.

2.3 Seismological theory

2.3.1 Elastic wave equation and body waves

A major field in seismology deals with Earth's structure. The energy released by an earthquake in the form of elastic waves propagates throughout the Earth, and the ground motion caused by it can be recorded at seismic stations. Several quantities of this recording (e.g., travel time, amplitude, attenuation, full-waveform) are used to infer Earth's internal attributes such as velocity, dynamic processes, composition. Hence, the elastic waves generated by an earthquake provide powerful means of retrieving information of Earth structure, at depths that cannot be reached directly by man yet.

By combining the equation of motion and the expressions for stress and strain relationship in an isotropic elastic medium, one can derive the elastic wave equation, which can be written in terms of displacement ($\mathbf{u}$) as (Shearer, 2009):

$$\rho\ddot{\mathbf{u}} = (\lambda + 2\mu)\nabla(\nabla \cdot \mathbf{u}) - \mu\nabla \times \nabla \times \mathbf{u} \tag{2.1}$$

where ρ is the density, and μ and λ are the Lamé parameters, which describe the linear relationship between stress and strain within an isotropic solid. μ is known as the shear modulus: small values of μ indicate that applied shear stress is small compared to the shear strain caused by it, i.e. the object has low rigidity. Since fluids don't support shear stresses, $\mu = 0$ for them. The Lamé parameter λ does not have a physical meaning. Note that Equation 2.1 is a simplified version of the elastic wave equation in which the gradient terms of the Lamé parameters were ignored.

There are two main types of solutions to the wave equation: P (primary) and S (secondary) waves. They result from the stress imbalance occasioned by an earthquake and are known as body waves because they propagate through the volume (or body) of the medium. As a P wave travels through the medium, the particles are compressed and dilated in a direction parallel to the wave propagation direction, in longitudinal motion. The displacement caused by S waves is perpendicular to the propagation direction and is commonly divided into a vertical (SV) and a horizontal (SH) component. SV waves are contained in a plane through the propagation vector and SH waves are perpendicular to it. Figure 2.4 shows, in an illustrative and exaggerated way, the displacement caused by P and S waves.

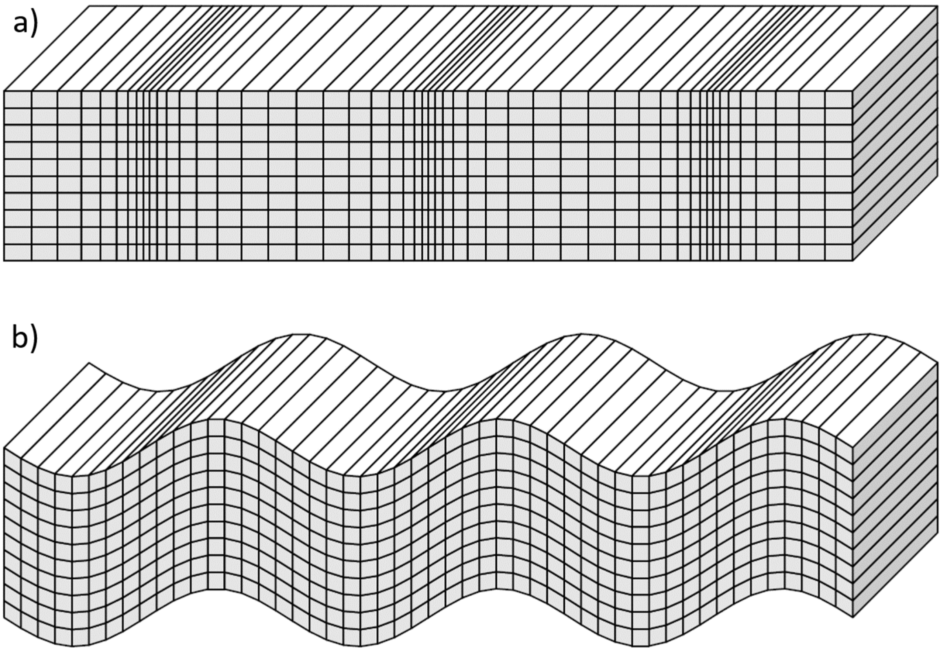

Figure 2.4: Displacement of the ground caused by a) P-waves; b) S-waves. Figure from Shearer (2009).

Equation 2.1 is a complicated partial differential equation for displacements in a media (Lay and Wallace, 1995). Instead of directly solving it, we can use Helmholtz's theorem to split the displacement into a scalar function $\phi(\mathbf{x}, t)$ and a vector function $\Psi(\mathbf{x}, t)$, in order to obtain solutions for P and S waves. This theorem is expressed as:

$$\mathbf{u} = \nabla\phi + \nabla \times \Psi \tag{2.2}$$

After some algebra (see Lay and Wallace, 1995; Stein and Wysession, 2003), substitution of Equation 2.2 into Equation 2.1 yields in one wave equation for each potential:

$$\nabla^2\phi = \frac{1}{\alpha^2}\frac{\partial^2\phi}{\partial t^2} \tag{2.3}$$

$$\nabla^2\Psi = \frac{1}{\beta^2}\frac{\partial^2\Psi}{\partial t^2} \tag{2.4}$$

where:

$$\alpha = \sqrt{\frac{\lambda + 2\mu}{\rho}} \tag{2.5}$$

and

$$\beta = \sqrt{\frac{\mu}{\rho}} \tag{2.6}$$

are P- and S-wave speeds, respectively. Although equations 2.5 and 2.6 are strictly valid for isotropic elastic media, observations show that P-waves are always faster than

S-waves. Also, from Equation 2.6, S-waves cannot propagate through liquids ($\mu = 0$), and this behavior is the primary evidence for a liquid outer core.

2.3.2 Surface waves

Besides body waves, other solutions to the seismic wave equation are surface waves, whose propagation is along the surface of the Earth and result from the interaction of seismic waves with a free surface. There are two types of surface waves, named after their discovers:

- **Rayleigh waves**: Formed through a combination of P and SV waves, with all their motion contained in a vertical plane parallel to the direction of propagation. They are recorded in the vertical and radial components of a seismogram, out of phase by $\pi/2$, which causes an elliptical movement from retrograde at the surface to prograde at depth.
- **Love waves**: They are formed by constructive interference of SH waves and its multiples. Unlike Rayleigh waves, Love waves cannot exist in a halfspace of constant velocity, because they require a velocity gradient. The simplest model in which Love waves can occur is a layer of thickness h and velocity β_1 over a halfspace of velocity β_2, where $\beta_1 < \beta_2$ (Stein and Wysession, 2003). Figure 2.5 is a representation of the motion of the ground particles caused by Love and Rayleigh waves.

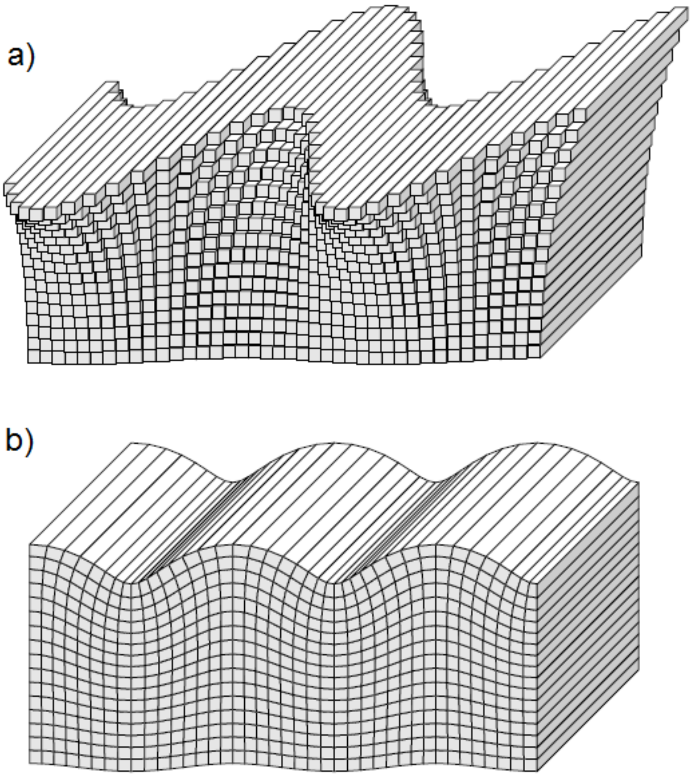

Figure 2.5: Displacement of the ground caused by a) Love waves; b) Rayleigh waves. Figure from Shearer (2009).

Because of the geometric spreading in two dimensions, surface wave energy decays with distance approximately as $1/r$, where r is the source-receiver distance, rather than as $1/r^2$

for body waves (Stein and Wysession, 2003), whose energy is spread in three dimensions. Hence, at large source-receiver distances, surface waves will be the prominent recording in broadband seismograms, as shown by Figure 2.6, where we can see that surface waves have greater amplitudes than P- and S-wave phases. Note that the Rayleigh waves are recorded in the vertical and radial components, and the Love waves are recorded in the transverse component. Due to this slower rate of decay, it is possible that surface waves generated by a large earthquake circle the Earth many times.

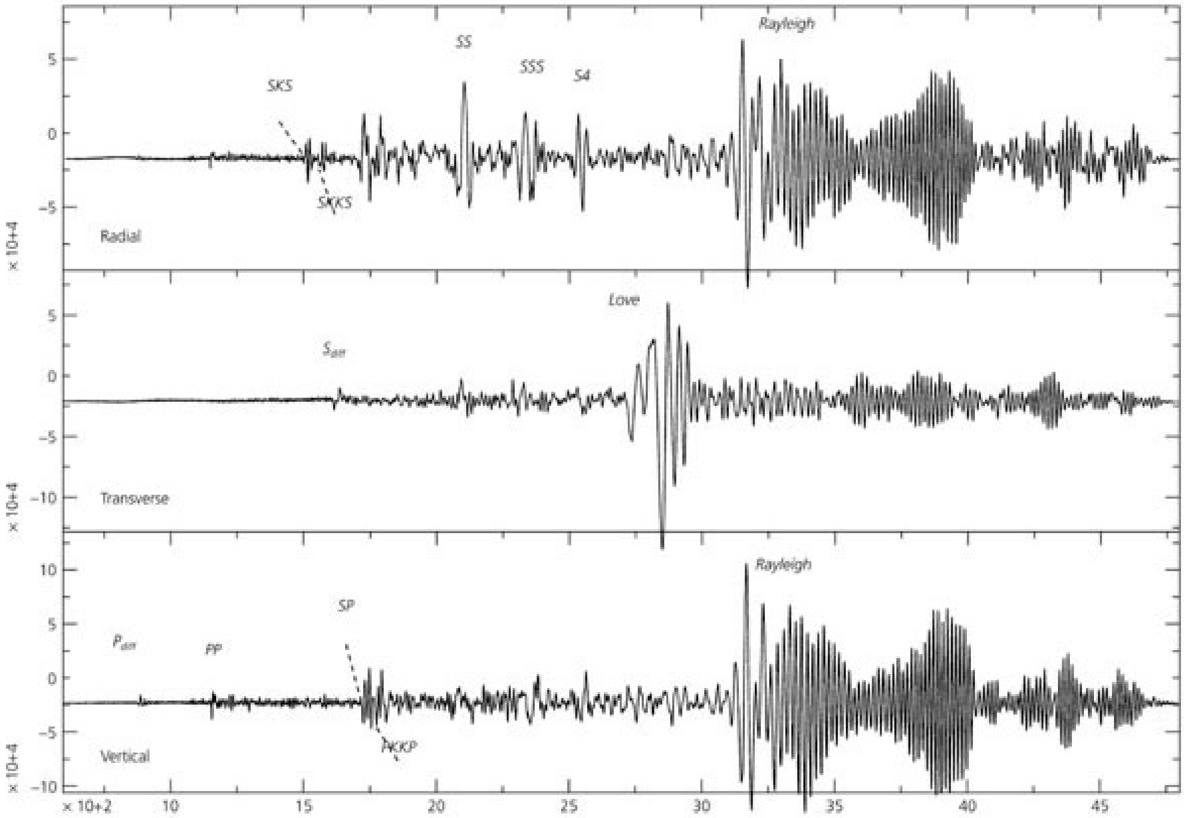

Figure 2.6: Record of an earthquake in the Vanuatu trench, with source-receiver distance of 110°. Note the high amplitude of surface waves compared to body waves. Figure from Stein and Wysession (2003).

Surface waves must satisfy a boundary condition of free surface and are characterized by slower speeds when compared to body waves, arriving after P- and S-waves and their latter arrivals such as reflections, refractions, and scattering. Among surface waves, Love waves are usually faster than Rayleigh waves. Another interesting feature of surface waves is that their velocity is frequency dependent, a property named dispersion, which is one the basis of surface wave tomography.

2.3.3 Dispersion, group and phase velocity

In Earth, there are velocity gradients with depth, because of changes in composition and variations of pressure and temperature states. The inner structure can be roughly divided into the following main layers: crust, mantle, outer core, and inner core. Each layer presents its subdivisions and velocity gradients, which vary spatially around the world. For example, the discontinuity between upper crust and lower crust, named Conrad discontinuity, is observed in some regions of continental crust but in others not. There is a variation in depth of the discontinuity between crust and upper mantle (Mohorovičić discontinuity) around the world, and knowledge about crust thickness can provide useful insights on geological history and processes.

Surface waves, especially Rayleigh, own their dispersive character to the velocity gradient in real Earth. Since surface wave frequencies travel with different velocities, they are sensitive to different ranges of depths, and a small change in S-wave velocity at depth can lead to a great change in surface wave velocity. Longer periods generally travel faster than shorter ones, because they are more sensitive to deeper materials with faster speeds (Figure 2.7).

There are two main well-established approaches of surface wave tomography: full-waveform inversion in the time Domain and travel time inversion in the frequency Domain (Romanowicz, 2002). In the first approach, first-order perturbation theory (e.g., Woodhouse and Dahlen, 1978) is applied to compute and perturb synthetic seismograms. In this work we apply the second approach, inversion of travel times of dispersion curves in the frequency Domain to generate seismic wave velocity maps for several periods, which can later be jointly inverted for 3D S-wave velocity. Developed by Nakanishi and Anderson (1983), Nakanishi and Anderson (1984) and Nataf et al. (1986) to study global mantle velocities, this technique gained worldwide popularity, with several researchers refining and applying it at local, regional and global scales.

Surface wave tomography using dispersion measurements can be performed either with phase or group velocities. Phase velocity (c) is the velocity at which peaks and troughs travel, and is by definition given by:

$$c = \frac{\omega}{k} \tag{2.7}$$

where ω is the angular frequency and k is the wavenumber. To work with single station phase velocity measurements, focal mechanism data are required, because we need to know the source phase in the moment of the rupture. This limits the dataset to relatively high magnitude events, with well defined focal mechanisms. A workaround to eliminate the source phase is to use the two-station method for measuring phase velocities (e.g., Snoke and James, 1997), but in this case, the source and the two receivers must lie approximately within the same great circle. Since earthquakes tend to concentrate on plate boundaries, this also limits the dataset.

On the other hand, single station group velocity calculations only require information on the source and the receiver coordinates and event origin time. This allows measurements of dispersion curves of earthquakes with smaller magnitudes and there is no need for epicenters aligned with pairs of stations. In this work, we only measure Rayleigh wave group velocity curves. Group velocity (U) is the velocity of a longer period envelope of waves and is related to phase velocity by:

$$U = \frac{d\omega}{dk} = \frac{d(kc)}{dk} = c + k\frac{dc}{dk} \tag{2.8}$$

For Earth, the phase velocity of surface waves generally decreases with frequency ($dc/dk < 0$), and hence group velocity is less than or equal to phase velocity (Shearer, 2009). Sensitivity (S) is defined as the derivative of group velocity with respect to S velocity:

$$S = \frac{\partial U}{\partial \beta} \tag{2.9}$$

Variation of Rayleigh wave sensitivity according to depth and period is provided in Figure 2.7, relative to the AK135 velocity model (Kennett et al., 1995). A general pattern of longer period waves being sensitive to deeper S velocity variations can be grasped: 10 s period waves are sensitive to shallow upper crust structure while 150 s period waves are sensitive to lithospheric structure.

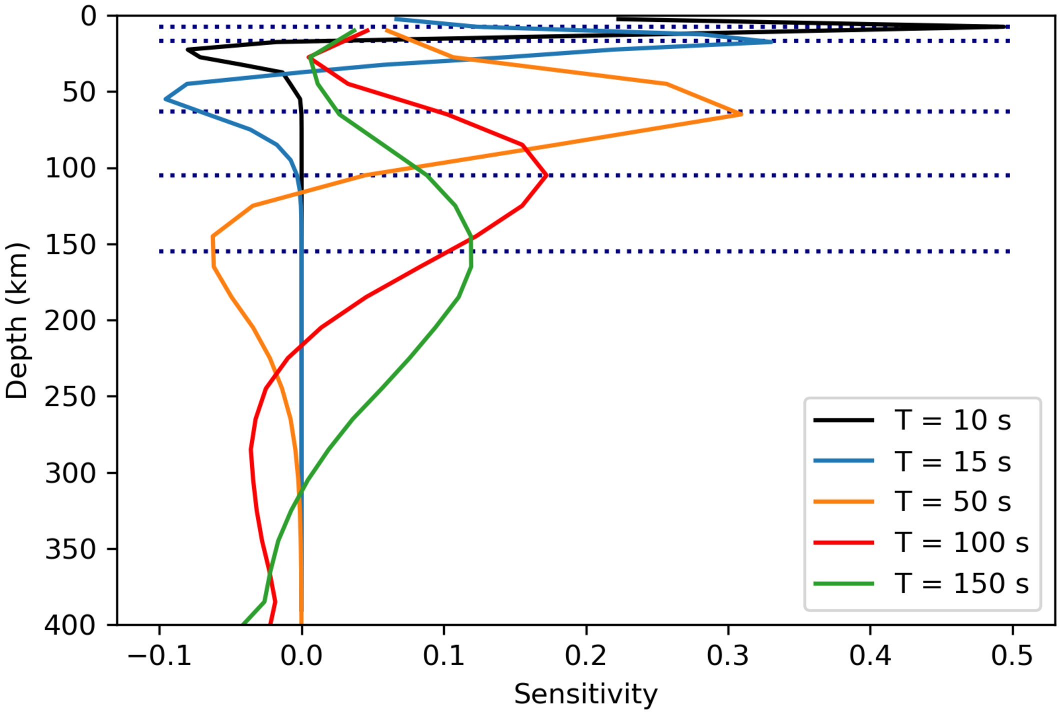

Figure 2.7: Sensitivity kernels of Rayleigh waves relative to the AK135 velocity model. Sensitivity kernels for periods of 10, 15, 50, 100 and 150 s are shown. Dotted dark blue lines are representing sensitivity peaks, that is, depths that influence the respective wave period the most.

2.4 Previous geophysical studies

The lithospheric structure beneath South America has been imaged by some tomographic studies, with different datasets, inversion approaches, parameterizations, and resolutions. In this section results from studies of several researchers are briefly summarized. Since our work is concerned with surface wave tomography, special attention will be given to tomographic results, ranging from global to local scale.

Prior to the advent of tomographic techniques in seismology, early works (e.g., Toksöz et al., 1967; Anderson, 1967) provided evidence for the existence of lateral inhomogeneities in the Earth's mantle. Even though the first well-accepted one dimensional model of the

Earth, *Preliminary Reference Model - PREM* (Dziewonski and Anderson, 1981), was published in 1981, the radial velocity and density structure of the Earth was relatively well known by 1970 (Shearer, 2009). Therefore, the focus was shifted to resolve lateral differences in velocity from inversion of seismic data to obtain three-dimensional structure. Pioneering works in seismic tomography include Aki and Lee (1976), which inverted P-wave travel time data for both velocity structure and hypocenter parameters (i.e. local earthquake tomography), Aki et al. (1977), which produced the first example of what is now known as teleseismic tomography, and Dziewonski et al. (1977), which inverted over 700000 travel time residuals of P-wave for velocity structure. Since then, seismic tomography has become a popular method within seismology, now performed with increasingly larger datasets.

Early results of the velocity structure beneath the South American continent were within the scope of global tomography. In this context, seismic tomography using surface waves is particularly useful, because they allow the sampling of regions devoid of dense seismic station coverage, such as South America, Africa, and oceans (Romanowicz, 2002). Examples of global tomography studies include Trampert and Woodhouse (1995), Laske and Masters (1996), Ekström et al. (1997), Ritzwoller et al. (2002), Zhou et al. (2006), Haned et al. (2015). Although global tomography is a robust method for studying large scale structures, it is not suitable for regional interpretation due to poor resolution ($>10°$). In South America, this kind of model is generally not capable of distinguishing the main geological provinces.

Paraná Basin, in Brazil, has been an object of study of several tomographic works. The study of VanDecar et al. (1995) presented the first local tomographic model in Brazil, using P- and S-waves, and imaged parts of the São Francisco Craton and the Paraná Basin. The most astonishing feature in their model is a low-velocity anomaly in a cylinder-like shape, which was interpreted as a thermal conduit of the plume that supplied the Paraná plume head, responsible for the Paraná flood basalts. The dimensions of this low-velocity anomaly were estimated as about 300 km across, between depths of 200 to 500-600 km. Schimmel et al. (2003) inverted a larger dataset, confirmed the presence of the low-velocity anomaly beneath the Paraná Basin, and suggested that it may be confined to the upper mantle. Liu et al. (2003), however, based on results of common conversion point receiver functions (used to study deep discontinuities of the mantle, mainly the 410 and 660-km second-order discontinuities), showed that there is no perturbation in the transition zone thickness, indicating that either the low-velocity anomaly does not extend to the mantle transition zone or it is rather compositional than thermal.

Still in the Paraná Basin, Snoke and James (1997), using group and phase interstation velocities of Rayleigh and Love waves, obtained an average Moho depth of about 42 km for the eastern part of the basin and a maximum S-velocity of the upper mantle lid equal to 4.7 km/s, a quite high value. They also found a shallow Moho depth of 32 km for the Chaco Basin, with upper mantle S-wave velocities of 4.2-4.3 km/s. By joint inversion of receiver function and surface waves, An and Assumpção (2004) found low velocities (less than 3.8 km/s) in the lower crust beneath Paraná Basin and their results also pointed that possible underplating processes in the basin, accompanying basalt extrusion, might not be widespread.

Rocha et al. (2011) presented a model for central and SE Brazil from travel time tomography of P- and S-waves. They included more stations and paths to their data set compared to previous studies, which allowed to image several new features of the São Francisco Craton and the Paraná Basin. Due to the increased resolution, the 150-km depth velocity map of the basin can be roughly correlated with a suture zone model for its basement, proposed by Milani and Ramos (1998). In the São Francisco Craton, a high-velocity anomaly extends westward beyond the geological surface limit, supporting a hypothesis that the craton was part of a larger plate from the Neoproterozoic (e.g., Alkmim et al., 1993). Some of the tomographic models beneath South America obtained by a number of authors are presented in Figure 2.8.

In the regional surface wave tomography context, we can cite the studies of Silveira et al. (1998) and Silveira and Stutzmann (2002) that produced phase velocity maps for the Atlantic ocean using stations from the global permanent network. Vdovin et al. (1999), also using global stations, obtained about 7000 Rayleigh wave and 4800 Love wave dispersion curves from 765 events recorded at 48 stations. However, only 15 stations and 213 events of their dataset were located on or near South America. The dispersion curves were inverted to produce group velocity maps of the South American continent and neighboring oceans. They claim that their model can resolve structures with scale length of 6-8° across South America for periods below 100 s, but has a decreasing resolution for longer periods and at the edges. Some of their results include:

- The low velocity signature of some sedimentary basins could be identified in the 20s Rayleigh map (Figure 2.8c), but the sediments of the Amazonian Basin could not be distinguished;
- Crustal thickness variations could be qualitatively interpreted across the South American continent;
- The Amazonian and São Francisco Cratons could not be distinguished in the high velocity anomaly. This often occurs in global tomography models as well, due to low resolution;
- Low velocity anomaly corresponding to the Galapagos Ridge.

Deployment of portable temporary networks (e.g., BLSP experiment (James et al., 1993; Assumpção et al., 2002), BANJO experiment (Beck et al., 1996), VEN92 experiment (Russo and Silver, 1996)) in the South American continent enabled deep structure to be represented by better resolution models. Van der Lee et al. (2001, 2002) performed a waveform inversion with aid of the partitioned waveform inversion (PWI) method described by Van der Lee and Nolet (1997), to generate a model for central and western South America upper mantle S velocity structure, named SA99. However, their data set was restricted to about 500 waveforms, yielding in a heterogeneous coverage that was reflected in good resolution only beneath certain parts of South America.

Feng et al. (2004) inverted approximately 6000 Rayleigh wave group velocity dispersion curves to provide the first S-wave velocity model with a reasonable resolution for the whole South American continent. They measured Rayleigh and Love wave velocities of stations from both the permanent network and the BLSP experiment and they claim that their model has the best possible resolution of 300 km at crustal depths and 600 km at lithospheric depths. However, that resolution seems to be achieved only beneath SE Brazil, where most of the stations are concentrated, and is degraded toward northern and northeast Brazil. Feng et al. (2007) complemented their previous study by adding about 1500 waveforms and jointly inverting them with the group velocity measurements. The use of higher mode waveform data improves the maximum depth reached to about 300 km. Some of the results and implications of both studies are as follow:

- Low velocities in the 20 s period Rayleigh wave map associated with the major sedimentary basins in South America;
- At 30 km depth, the lowest velocities are found beneath the highest topography of the Andes; high velocities in the Guyana shield compatible with high Bouguer anomalies; low velocity in the Paraná Basin and relatively higher velocities in the Pantanal Basin;
- At 100 km depth, high velocities are found in the Amazonian and São Francisco Cratons; flat slab segments of the Andean cordillera present moderate to high velocities;
- The Amazonian Basin is underlain by high velocities like the Central Brazil and Guyana shields;
- The lithosphere of the Amazonian Craton is interpreted to be thicker (approximately 200 km) and faster in the eastern Archean part than in the western part;
- From a low velocity trend at 100 km, the Transbrasiliano Lineament is suggested to be a zone of thinner lithosphere rather than just a surface feature.

Heintz et al. (2005) built an SV-wave model for South America and the neighboring oceans from inversion of 5850 Rayleigh waveforms (Figures 2.8a, 2.8b). Unlike Feng et al. (2007), they found the upper mantle velocity of the Amazonian Basin to be slower than that of its surrounding Central Brazil and Guyana shields. Their model shows low-velocity anomalies related to the Carnegie and Chile ridges and they propose that slab windows channels the sublithospheric mantle flow from the Pacific to the Atlantic. An important observation is that their model is unable to separate the São Francisco from the Amazonian Craton.

In the Borborema Province, NE Brazil, Dias et al. (2015) cross-correlated ambient seismic noise in order to obtain Rayleigh wave dispersion curves between pairs of stations, which were inverted to generate group velocity maps from 5 to 20 s, therefore modeling shallow structure. Short period maps (5 and 10 s) correlate well with surface geology and in the longer period maps (15 to 20 s) some structures, such as the Rio Grande do Norte Domain, fades away, suggesting that they are rather supracrustal than lithospheric. Goutorbe et al. (2015) also applied ambient noise tomography to the eastern part of Brazil to produce Rayleigh wave maps in the period range 6-23 s. Their model is in general agreement with the one of Feng et al. (2004), but there are some significant differences between the two 20 s maps, especially within the Tocantins province.

Russo et al. (2010) deployed 39 stations in southern Chile to study the region of the Chile triple junction. P-wave tomography seems to show a slab window, that is, a gap between the subducted Antartic and Nazca plates that appears to be filled with warm asthenospheric material, which is slower than the surrounding asthenosphere. This is the first direct evidence of a forming slab window. Analysis of shear wave splitting also indicates perturbations of upper mantle flow due to the slab window.

Azevedo et al. (2015), based on P-wave tomography results in central Brazil, found low-velocity anomalies, in general agreement with the Transbrasiliano Lineament, interpreted as a zone separating the São Francisco and Amazonian paleoplates. This study also confirmed a correlation between low-velocity anomalies in the Tocantins Province and a high seismicity zone (Goias-Tocantins seismic zone), as pointed out by a previous study by Assumpção et al. (2004). The latter study suggests that high seismicity is caused by lithospheric thinning. Rocha et al. (2016) also provided more evidence that thinner lithosphere between the São Francisco and Amazonian paleocontinents is related to this high seismicity zone.

More recently, Rosa et al. (2016) added group velocity measurements from both earthquakes and interstation ambient noise cross-correlation to the database of Feng et al. (2004) in order to improve path coverage in the Paraná and Chaco Basins. Even though they did not perform a second inversion step for S-wave velocity structure, they constructed group velocity period maps based on two different regularization approaches: one minimizing the first derivative (e.g., Feng et al., 2004) and other minimizing the second derivative (e.g., Pasyanos et al., 2001).

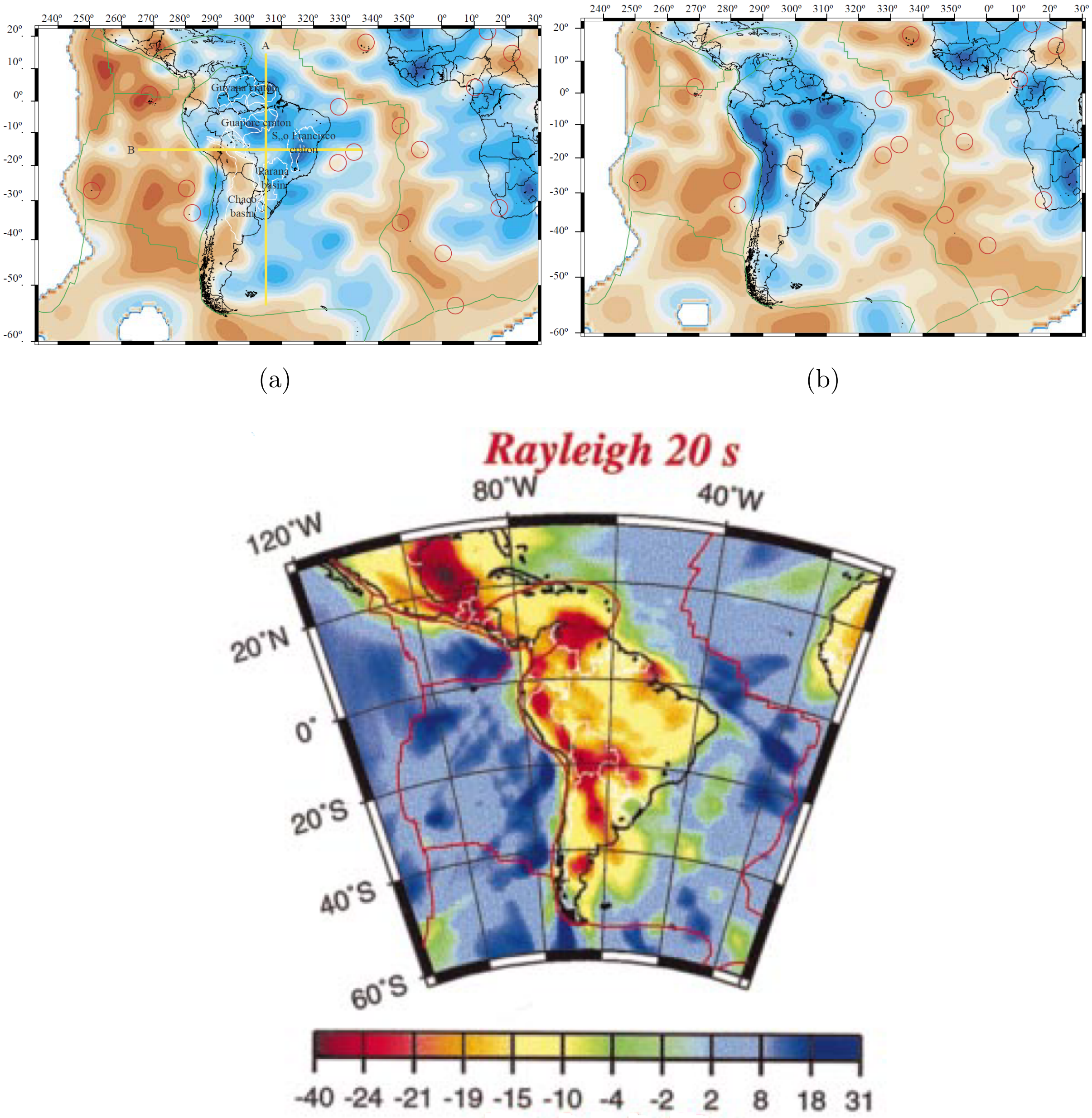
240° 250° 260° 270° 280° 290° 300° 310° 320° 330° 340° 350° 0° 10° 20° 30°
20° 10° 0° -10° -20° -30° -40° -50° -60°
A
B
Guyana craton
Guapore craton
S.o Francisco craton
Parana basin
Chaco basin
Rayleigh 20 s
120°W
80°W
40°W
20°N
0°
20°S
40°S
60°S
-40 -24 -21 -19 -15 -10 -4 -2 2 8 18 31

(a)

(b)

(c)

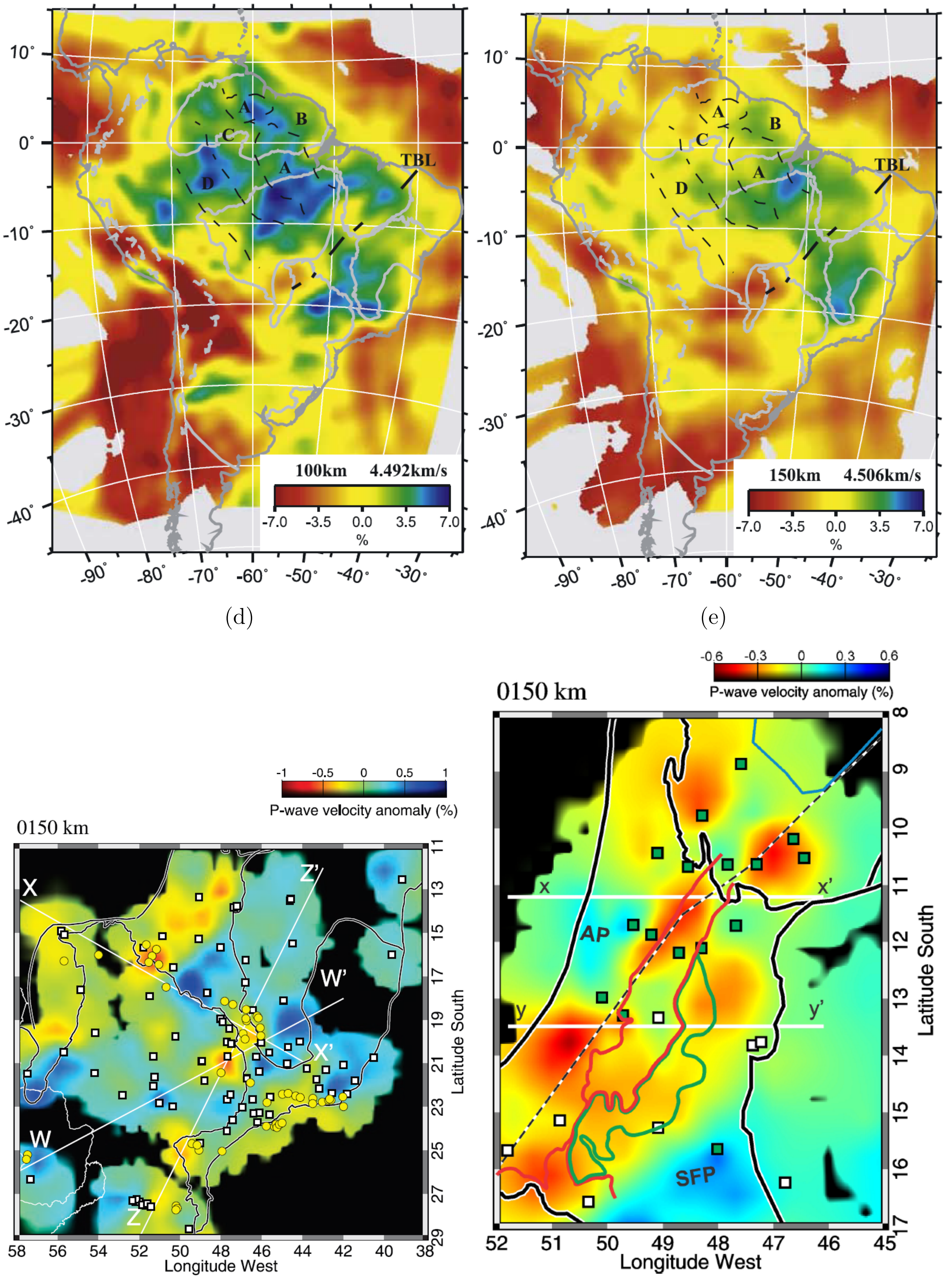

(d)

(e)

(f)

(g)

Figure 2.8: a) S velocity slice at depth of 100 km (Heintz et al., 2005); b) S velocity slice at depth of 150 km (Heintz et al., 2005); c) 20 s map of Vdovin et al., 1999; d) S velocity slice at depth of 100 km (Feng et al., 2007); e) S velocity slice at depth of 150 km (Feng et al., 2007); f) P velocity slice at depth of 150 km (Rocha et al., 2011; g) P velocity slice at depth of 150 km (Azevedo et al., 2015).

Chapter 3

Data processing

3.1 Introduction

The problem of modeling group velocity lateral variation maps from Rayleigh wave dispersion measurements can be divided into several steps. In this chapter and in Chapter 4 the methodology applied to achieve such maps (Figure 3.1) is described in some detail.

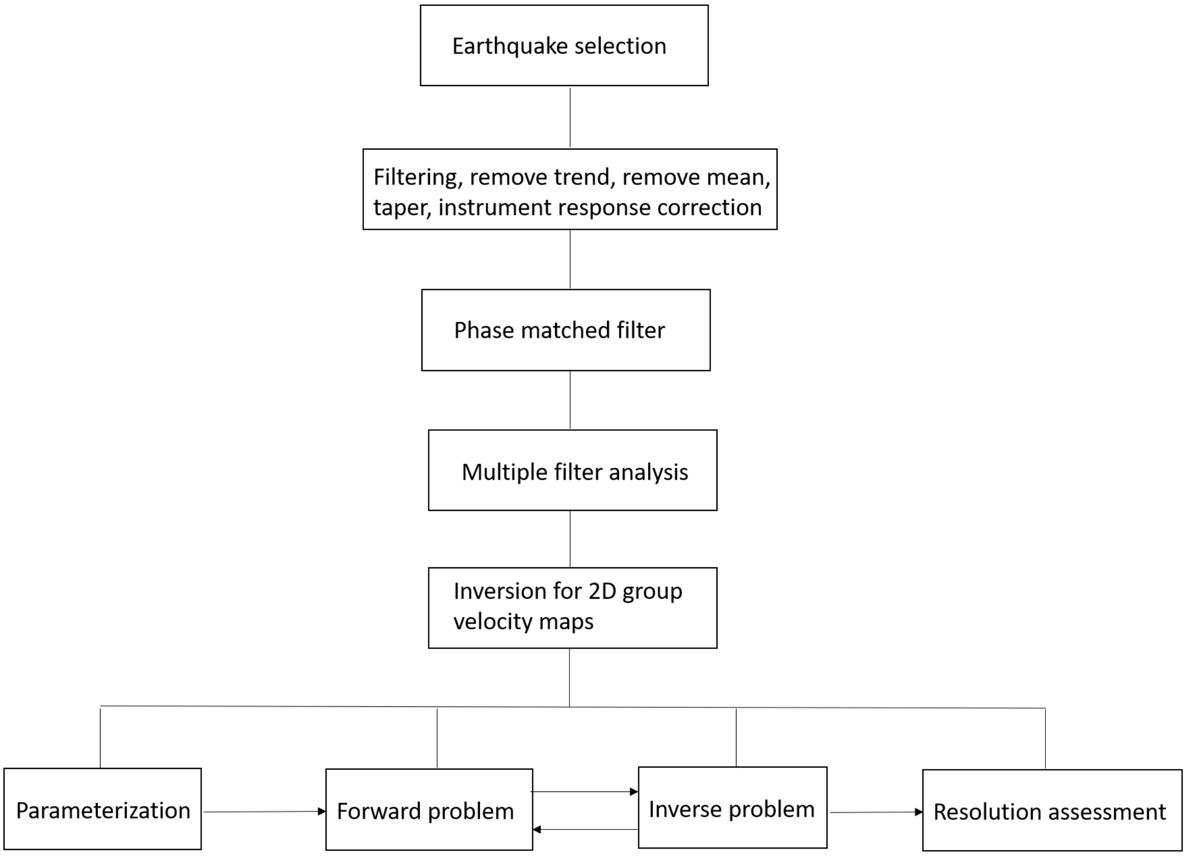

Figure 3.1: Flow chart summarizing the methodology applied in this work.

First, we establish some criteria whether the seismogram will be downloaded or not. Then, we apply pre-processing techniques to the seismograms, aiming to enhance the quality of the dispersion curves and improve signal to noise ratio. Those techniques include filtering, trend and mean removal, taper filtering, and instrument response correction. Except for the latter, those signal enhancing techniques were performed with aid of the ObsPy Python library (Krischer et al., 2015; Beyreuther et al., 2010). The files were instrument corrected using the EVALRESP module of the Seismic Analysis Code (SAC), where the required instrument poles and zeros information is extracted from a dataless file of the respective station. After pre-processing every seismogram, we proceed to the processing stage, which includes phase-matched filtering and multiple filter analysis. In this stage, we measure dispersion curves relative to each path (a path can be defined as the travel time for a given source-receiver pair) and estimate Rayleigh wave group velocities of several periods. Those observations constitute the **data**: average velocities of the whole path. In the inversion step, we wish to relate the **data** to the **model parameters**, which are in this case SV velocities at several points of the medium. The tomographic problem of estimating group velocity maps from dispersion curves is divided into four steps: (i) parameterization of the study area; (ii) given the model parameters, calculation of theoretical travel times through the array of sources and receivers - the forward step; (iii) adjustment of model parameters to better satisfy the observed data - the inverse step; (iv) assessment of model resolution (Chapter 4).

3.2 Data

To measure fundamental mode group velocity dispersion curves, we only process the vertical component of broadband station seismograms, because Rayleigh waves (P-SV motion) are better recorded in this component. The recordings are stored in files in the SAC format, and it is required for the group velocity calculation that the source and receiver coordinates (latitude, longitude, depth) to be filled in the file header. Moreover, the origin time of the earthquake must be present in the header as well. The station coordinates were retrieved from their respective dataless file. For each event, the source parameters required were obtained from the United States Geological Survey (USGS) catalog, available at `https://earthquake.usgs.gov/earthquakes/search/`. Only events with epicenter in South America were included in our database, focusing on pure continental paths. Also, we only processed paths with source-receiver distances greater than 15°, magnitudes larger than 5.0 and depths down to 100 km. We selected 1043 earthquakes occurring from 2002 to 2019, registered by a total of 282 stations - keep in mind that events are not generally recorded by every station. Figure 3.2 shows the distribution of receivers across South America; the reader is referred to Table 3.1 for a more detailed description of the network codes in Figure 3.2.

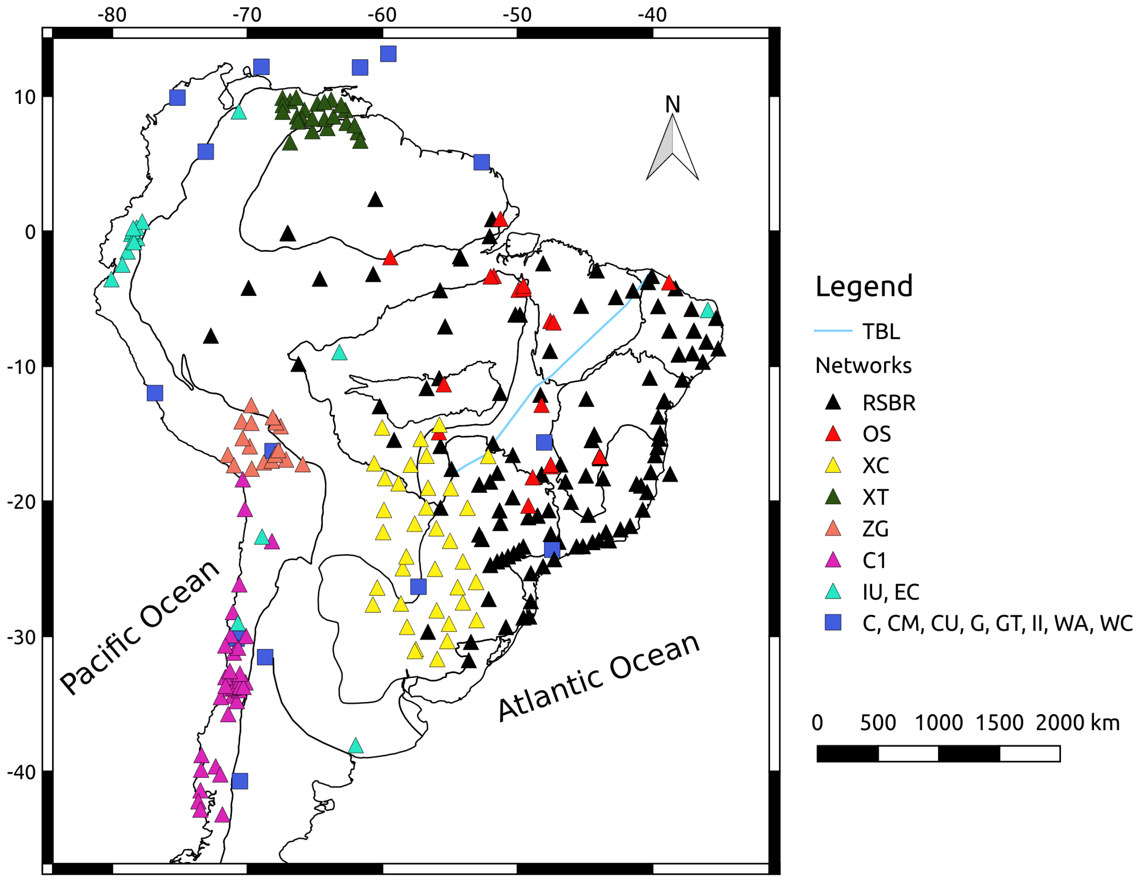

Figure 3.2: Distribution of receivers across South America. Black contours are the main geotectonic provinces of South America presented in Figure 2.2.

To grasp an insight into the statistical distribution of some source parameters, Figure 3.3 shows boxplots of the distances, magnitudes, and depths of the events in our dataset. A boxplot is formed by a box, two straight vertical lines - called whiskers - and some points - called outliers. The length of each box is defined by the first quartile (Q1, 25% of the distribution) and by the third quartile (Q3, 75% of the distribution). Also, the lines inside each box represent the median (second quartile, Q2) of distance, magnitude, and depth of the events in our dataset, respectively. The whiskers represent the variability of the data outside the (Q1, Q3) interval, and is formed by points that fall within:

$$(\mathrm{Q1} - 1.5 \cdot \mathrm{IQR}, \mathrm{Q3} + 1.5 \cdot \mathrm{IQR}) \tag{3.1}$$

where IQR is the interquartile range (Q3-Q1). The outliers are the points that fall outside the whiskers. Some of the immediate conclusions of Figure 3.3 include:

- The majority of our data has path lengths between 25° and 35°, and actually paths longer than 50° are quite rare;
- Most events have intermediate magnitudes between 5.0 and 6.0, with median equal to 5.5;

- Most events are rather shallow (depth <30 km) than deep, and depths below 60 km are outliers.

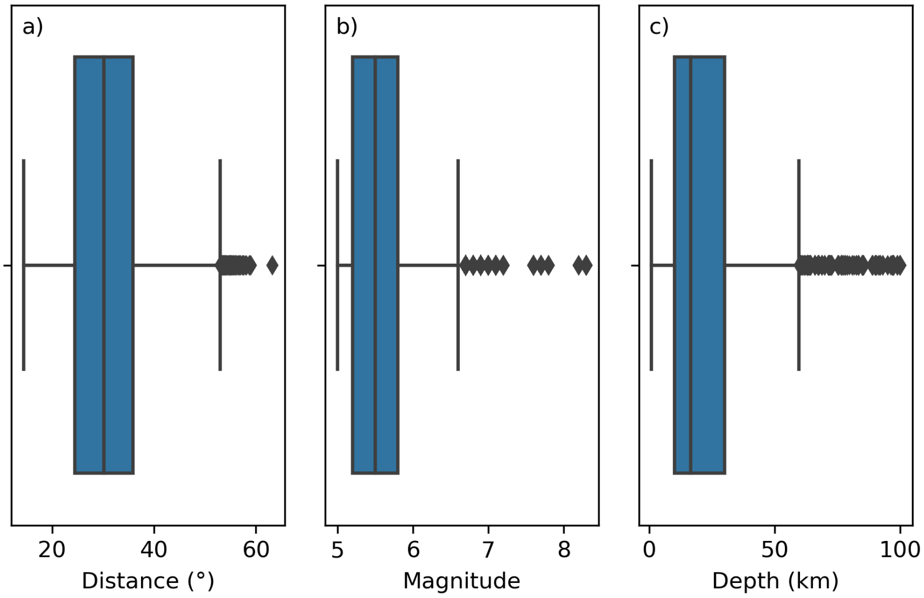

Figure 3.3: Boxplots of a) distance, b) magnitude and c) depth of the events in the dataset.

Since we did not use data from stations outside the continent and earthquakes from distant sources such as the Atlantic Ridge, our paths tend to have a relatively small length, and most of our source-receiver distances are less than 35°, as shown by the boxplot. This is good to minimize diffraction effects, which are stronger on longer paths and periods (Feng et al., 2004). Usually, earthquakes with greater magnitudes have a better signal to noise ratio, and for this reason, we choose 5.0 as our minimum magnitude, instead of the cut-off value of 4.5 used by Feng et al. (2004, 2007). Even though most of the events in our dataset have magnitudes between 5.0 and 6.0, some of them have magnitudes larger than 8.0. We noticed that deeper earthquakes tended to have a poorer signal to noise ratio and dispersion curves less defined, and this is why the maximum depth in our database is 100 km.

Compared to previous regional studies using surface wave tomography (e.g., Vdovin et al., 1999; Feng et al., 2004; Heintz et al., 2005; Feng et al., 2007), the recently installed RSBR stations provide a better coverage, especially in northern and northeast Brazil, and can hopefully yield in a more well constrained Rayleigh wave group velocity maps. Besides data from the RSBR stations, we also used data from several other networks, including both temporary and permanent networks. Table 3.1 sums up the networks used in this work and their respective number of stations.

Code	**Network name**	**Number of stations**
BL	Brazilian Lithospheric Seismic Project (BLSP)	55
BR	University of Brasilia Seismic Network	28
ON	Rede Sismográfica do Sul e do Sudeste (RSIS)	18
NB	Northeastern Brazil (UFRN)	19
XC	Pantanal, Chaco and Paraná (PCPB) structural studies network	36
C1	Red Sismologica Nacional (RSN)	36
XT	Caribbean Passive Experiment	24
OS	Seismological Observatory, Brasilia, Brazil	18
ZG	Central Andean Uplift and the Geodynamics of the High Topography	17
EC	Ecuador Seismic Network	10
IU	Global Seismograph Network (GSN - IRIS/USGS) (GSN)	7
GT	Global Telemetered Seismograph Network (USAF/USGS) (GTSN)	4
CU	Caribbean USGS Network	2
G	GEOSCOPE	2
CM	Red Sismologica Nacional de Colombia	2
II	IRIS/IDA Seismic Network	1
C	Chilean National Seismic Network	1
WC	Curacao Seismic Network	1
WA	West Central Argentina Network	1

Table 3.1: Networks used in this work, with the respective number of stations.

3.3 Multiple filter analysis

For each year, a csv file with epicenter coordinates and origin time of the earthquakes that follow the criteria established in Section 3.2 was obtained. Then, the respective seismogram for each available path was downloaded. The seismic data were obtained from either the International Federation of Digital Seismograph Networks (FDSN, `http://www.fdsn.org/`) or the internal server of the Seismological Observatory of University of Brasília. To each vertical component seismogram in SAC format, several pre-processing techniques (Figure 3.1) were applied, aiming to improve the quality of the dispersion curves, followed by a processing step to measure group velocity.

The former approach to obtain group velocities from a seismic recording was the peak and trough method, in which one must manually or automatically read the arrivals from a well-dispersed surface wave train. However, a more accurate method to determine group velocities is a frequency-time analysis, through the Multiple Filter Technique (MFT), developed by Dziewonski et al. (1969). Designated to study instantaneous amplitudes and phases of multi-mode dispersed signals (which are dependent upon period and velocity), MFT can be used to estimate group velocity of Rayleigh waves. It applies a system of narrow bandpass Gaussian filters to the seismogram, each filter defined as:

$$H(\omega) = e^{\frac{-\alpha(\omega-\omega_0)^2}{\omega_0^2}} \tag{3.2}$$

where ω_0 is the central frequency of the symmetric filter and alpha is a parameter that controls the resolution: improved resolution in the time (velocity) domain implies a worse resolution in frequency (period) domain. We employ a version of MFT called multiple filter analysis, which considers instantaneous frequency instead of filter frequency to determine group velocities; this approach minimizes a systematic error in group velocity measurement of individual recordings (Shapiro and Singh, 1999). To apply the multiple filter analysis to each seismogram, we use a software from the Computer Programs in Seismology (CPS) package, available from `http://www.eas.slu.edu/eqc/eqccps.html` (Herrmann, 2013). This program is implemented according to the theoretical background proposed by Bhattacharya (1983), but it assumes a Gaussian signal amplitude spectrum instead of a linear shape (Herrmann and Ammon, 2002). According to Herrmann and Ammon (2002) one must increase the alpha parameter as source-receiver distance increases, in order to obtain a reasonable spectral amplitude estimate. Table 3.2 shows their recommendations of values of alpha as a function of distance.

Alpha	**Distance (km)**
25	1000
50	2000
100	4000
200	8000

Table 3.2: Recommendations for the alpha value according to the epicentral distance.

For more information on multiple filter analysis mathematical background, please refer to Dziewonski et al. (1969), Herrmann (1973), Bhattacharya (1983), Herrmann and Ammon (2002).

Higher modes of the surface waves may contaminate their spectra, so before the multiple filter analysis, we use the CPS program to apply a phase-matched filter (Herrin and Goforth, 1977) to isolate the fundamental mode from higher modes and to improve signal to noise ratio. A new fundamental mode seismogram is generated (the program creates a new file with the same name as the original, but with an 's' appended to the end), on which we perform the multiple filter analysis to extract group velocities relative to each path. Figure 3.4 shows an example of a seismogram before and after phase-matched filtering, where a significant improvement in signal to noise ratio can be seen. This is the record of an earthquake with epicenter at 0.2849°S, 80.492699°W and origin time on June 30, 2017 (22:29:45.14 UTC).

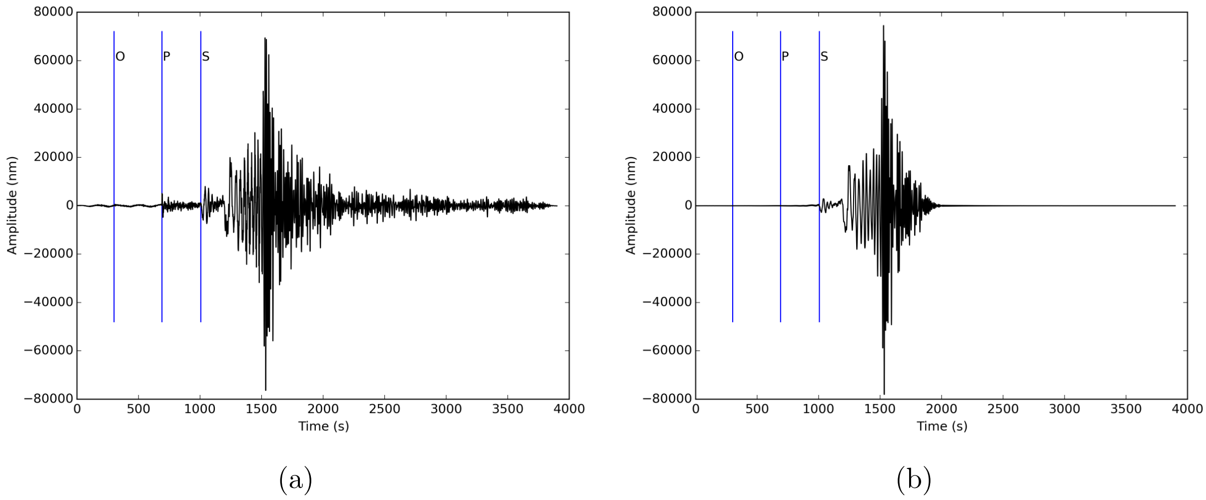

(a) (b)

Figure 3.4: Record of an earthquake a) before and; b) after phase matched filtering. The three vertical blue lines represent, from left to right, the origin time and P- and S-wave theoretical arrivals.

After creating a new presumably fundamental mode isolated trace, the next step is to analyze its Rayleigh wave dispersion curve. This procedure is repeated for each path in the dataset. Figure 3.5 is the dispersion curve of the earthquake shown in Figure 3.4. The period range of the curve in this example is 8-220s, but it varies for each seismogram, according to magnitude and distance: events with larger magnitudes at greater distances generally present longer periods better recorded (Feng et al., 2004; Feng and An, 2010). Therefore, the periods are unevenly sampled and periods in the range 15-100 s have more measurements than shorter and longer ones, as it can be inferred from Figure 3.6; path coverage is also different for each period.

In this work, we adopt a period range of 10-150 s and obtained up to 17000 group velocity measurements at 30 s, with the number of measurements decreasing for both shorter and longer periods (Figure 3.6). This uneven sampling implies different resolutions for each group velocity map, where the better-constrained ones should be expected to be the ones more densely sampled by rays, that is, the ones in the period range 15-100 s.

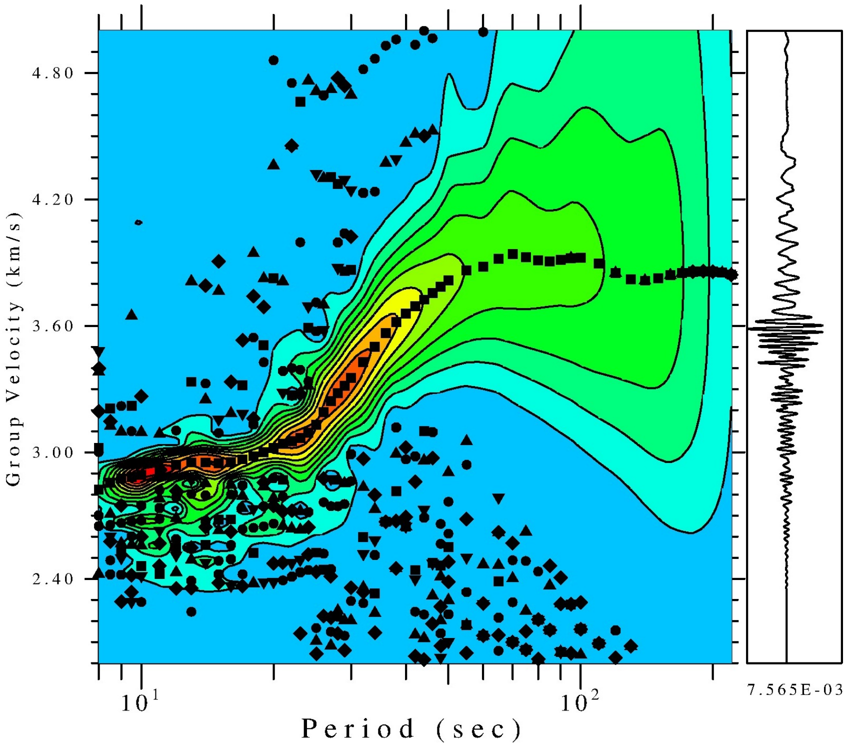

Figure 3.5: Example of Rayleigh wave dispersion curve, obtained from multiple filter analysis of the earthquake represented in Figure 3.4. The period range is 8-220 and the group velocity estimates for each period are represented by the black squares inside the energy contour.

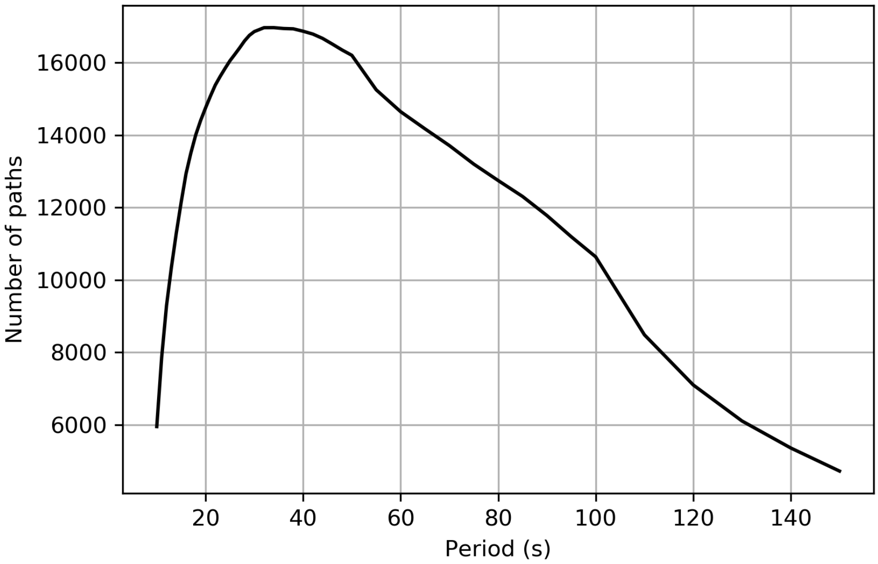

Figure 3.6: Number of path as a function of period. The number of rays is maximum at 30 s and decreases for both shorter and longer periods.

Chapter 4

Tomographic inversion

4.1 Introduction

After processing every seismogram using the multiple filter analysis, we have thousands of travel time observations (Figure 3.6), for each period. Each observation can be thought of as the time required by the respective wave frequency to travel from the source to the receiver, with a mean group velocity of the entire path. The problem is that from only an observation, we cannot distinguish the time took by the wave to travel across each different geological unit crossed by the wavefront, that is, it is not possible to know the seismic velocity within each of these units. Therefore, an inversion step (Figure 3.1) is required to estimate group velocity lateral variation maps, using information from all available paths to produce such maps for each period.

Often scientists wish to relate some set of observational data ($\mathbf{d}$) of a system to model parameters ($\mathbf{m}$) characterizing physical properties of the same system, through a known relationship $\mathbf{g}$:

$$\mathbf{d} = \mathbf{g}(\mathbf{m}) \tag{4.1}$$

where $\mathbf{d}$ and $\mathbf{m}$ may be continuous functions of time and/or space or discrete observations, and $\mathbf{g}$ is a function that relates model and data, and whose form depends upon the nature of the problem (Aster et al., 2019). The forward problem is to find $\mathbf{d}$ given $\mathbf{m}$, while the inverse problem is to find $\mathbf{m}$ given $\mathbf{d}$. According to Aster et al. (2019), there are three main issues concerning methods of inversion:

- *Existence*: because of noise in data and/or approximations made in $\mathbf{g}$, there may be no model solution that fits the data;
- *Uniqueness*: instead of a unique solution, several solution models may fit the data with a reasonable misfit;
- *Instability*: a small noise amount may have a great influence on the solution: this causes the inverse problem to be ill-posed. Regularization terms are frequently included in the inversion to stabilize it.

If the data are travel times beneath an array of earthquakes and stations, and the model is the structure of seismic velocity of the Earth, then we have a seismic tomography problem. The travel time of a given ray in a continuous velocity field is given by:

$$t = \int_S^R \frac{1}{v(\mathbf{x})} dl \tag{4.2}$$

where $\mathbf{x}$ is the position vector, S and R are the source and receiver coordinates, respectively, v is the velocity and dl is a differential path length. Equation 4.2 is non-linear because the path depends on the velocity structure and this may cause a difficulty to solve the inverse problem. It can be either: (i) linearized; (ii) solved by iteratively solving the forward and inverse steps, in order to account for non-linearity; (iii) solved by fully non-linear inversion (rarely done) (Rawlinson and Sambridge, 2003).

As stated in the previous chapter, seismic tomography can be divided into parameterization, forward step, inverse step and assessment of model resolution. All of those steps are performed using a Fast Marching Surface Tomography (FMST) package of Rawlinson (2005).

4.2 Model parameterization

Model parameterization concerns representation of a continuous velocity field in a discrete way. The most used parameterizations in seismic tomography are probably constant-velocity blocks (or cells in two dimensions) (e.g., Aki et al., 1977; Humphreys and Clayton, 1990; Feng et al., 2004) and velocity grid nodes (2D or 3D) with some sort of interpolation function associated (e.g., Thurber, 1983; Zhao and Kanamori, 1992; Saygin and Kennett, 2010). Illustrations representing both types of parameterizations are shown in Figure 4.1.

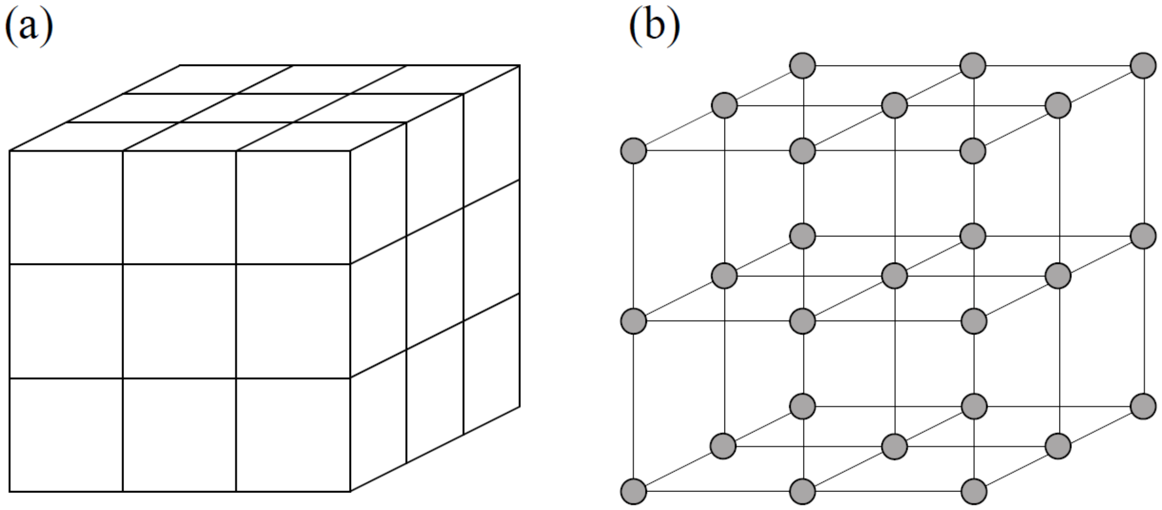

Figure 4.1: Examples of velocity parameterization: a) constant-velocity blocks, b) velocity grid nodes with an interpolation function associated. Modified from Rawlinson and Sambridge (2003).

constant-velocity blocks are widely used because they are simple to implement, but they may not be adequate to represent a smooth velocity field because they may cause artificial velocity gradients from a block to adjacent ones, possibly resulting in ray shadow zones and triplications (Rawlinson and Sambridge, 2003). Velocity nodes together with an interpolation function, on the other hand, can result in a velocity field with continuous first and second derivatives, depending on the order of the interpolation function used (Rawlinson and Sambridge, 2003).

To represent the velocity structure of the South American continent we define a grid of velocity nodes, with a bi-cubic B-spline interpolation function associated. A great advantage of cubic B-splines is that they are locally supported and therefore less constrained parts of the model don't have a global influence on the result. An optimum balance between recovery, resolution and computational processing time was found for a grid spacing of 1° by 1°.

4.3 Forward problem

In seismic tomography, the forward problem concerns calculating theoretical travel times for every available source-receiver path. In an elastic medium, seismic wave propagation is described by the Eikonal equation:

$$|\nabla_{\mathbf{x}} T| = s(\mathbf{x}) \tag{4.3}$$

where $\nabla_{\mathbf{x}}$ is the gradient operator, T is travel time field, s is slowness and $\mathbf{x}$ is a position vector. It is important to note that the Eikonal equation is restricted to the high frequency approximation: over one wavelength, the change in velocity gradient must be sufficiently small when compared to the velocity itself (Lay and Wallace, 1995), or, in another words, the wavelength of the seismic waves must be much less than the wavelength of the velocity structure being mapped. This causes resolving power to decrease with increasing period, and consequently larger periods can only map large velocity structures.

Because simple equations can be derived for rays (rays are the normal vectors to wavefronts) from the Eikonal equation, it is theoretically easier to track ray rather than entire wavefront propagation, and hence traditional travel time prediction is based on ray tracing. The equation governing ray propagation is given by (see Lay and Wallace, 1995):

$$\frac{d}{dl}\left(\frac{1}{v(\mathbf{x})}\frac{d(\mathbf{x})}{dl}\right) = \nabla\left(\frac{1}{v(\mathbf{x})}\right) \tag{4.4}$$

where $v(\mathbf{x})$ is the velocity field and dl is a differential path length. There are two ray-tracing methods to solve the forward problem: shooting and bending. Shooting methods (e.g., Julian and Gubbins, 1977, VanDecar et al., 1995) formulate Equation 4.4 as an initial value problem and calculate, iteratively, ray trajectory based on source position and initial ray direction. It is more used in 2D than 3D problems. Bending methods (e.g., Julian and Gubbins, 1977) establishes an arbitrary path joining source and receiver and iteratively adjusts it until it satisfies Fermat's principle. According to Rawlinson and Sambridge (2005), there are some issues with ray tracing, concerning robustness, speed and ray selection; even small velocity variations may cause shooting and bending not to converge.

An alternative to traditional ray tracing methods is to directly solve the Eikonal equation through a grid-based finite differences scheme (e.g., Vidale, 1988; Qin et al., 1992;

Buske and Kästner, 2004), therefore tracking the entire wavefront instead of a ray. In this context, we calculate theoretical travel times using the so-called Fast Marching Method or FMM (e.g., Sethian, 1996; Sethian and Popovici, 1999; Rawlinson and Sambridge, 2004b).

An issue that grid-based Eikonal solving numerical schemes must face is the arise of gradient discontinuities as the wavefront evolves, a problem that usually occurs when there is multipathing (Rawlinson and Sambridge, 2005). To address this difficulty, the implementation of FMM in FMST introduces a weak solution enforced by an entropy-satisfying upwind differences scheme (e.g., Sethian and Popovici, 1999):

$$\begin{bmatrix} max(D_a^{-x}T, -D_b^{+x}T, 0)^2 \\ +max(D_c^{-y}T, -D_d^{+y}T, 0)^2 \\ +max(D_e^{-z}T, -D_f^{+z}T, 0)^2 \end{bmatrix}^{1/2} = s_{i,j,k} \tag{4.5}$$

where (i, j, k) are grid increments in (x, y, z) directions and a, b, c, d, e, f are integers that define the order of the scheme, and, in the finite differences notation, for example, considering first order and x direction:

$$D_i^{-x} = \frac{T_i - T_{i-1}}{\delta x} \tag{4.6}$$

$$D_i^{+x} = \frac{T_{i+1} - T_i}{\delta x} \tag{4.7}$$

In other words, the entropy condition ensures that the wavefront only passes through a point once, and this causes FMM to be unconditionally stable; actually, FMM represents the first unconditionally stable grid-based Eikonal solver (Rawlinson and Sambridge, 2003). In our case, we employ a mixed order scheme, in which second-order operators are used whenever possible, but it switches to first order if D_2 is unavailable.

The order of points of the grid in which travel times are calculated is of major importance for FMM and must follow the direction from smaller to larger values of the travel time field. This is done by FMM by classifying points relative to a narrow band (Figure 4.2) concept: points in a narrow band are classified as close and have trial travel time values, points outside the narrow band in the direction opposite to the expanding wavefront (upwind) are classified as alive and have correct values and points that are outside the narrow band in the direction of the expanding wavefront (downwind) are classified as far and have no predicted travel times associated (Rawlinson and Sambridge, 2005).

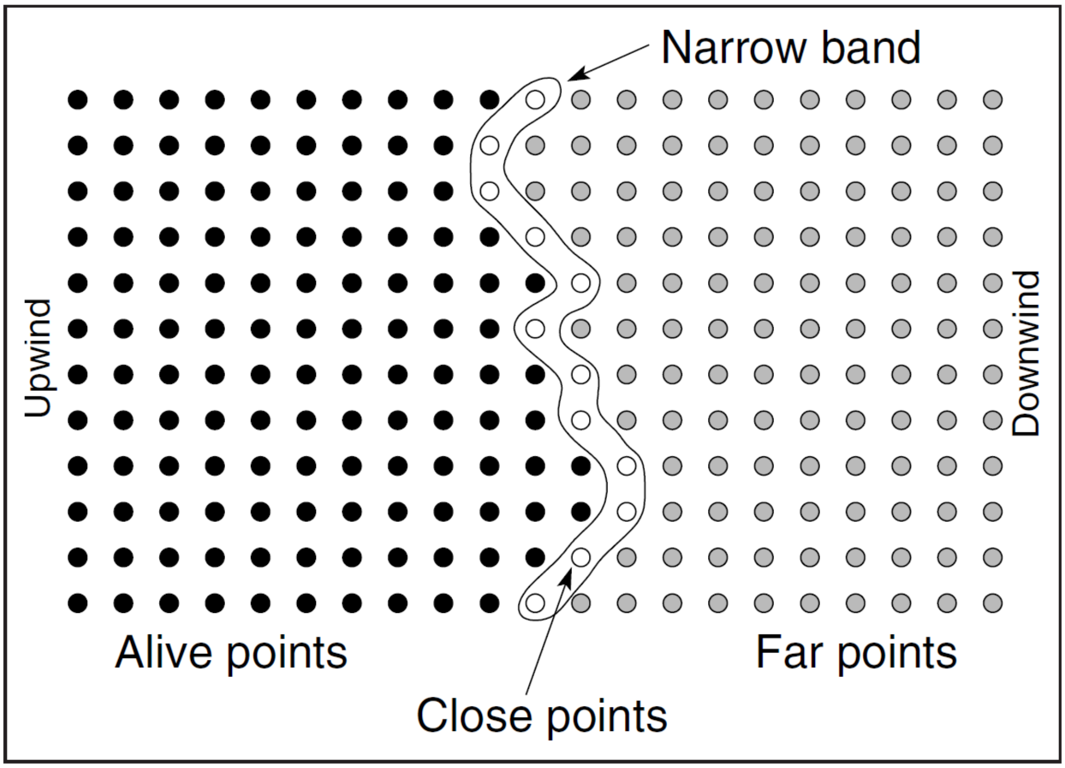

Figure 4.2: How the narrow band concept works. Extracted from Rawlinson and Sambridge (2005).

4.4 Inverse problem

For each period, we wish to determine its velocity field beneath South America, based on a set of observations of travel times, that is, we wish to invert travel time observations for velocity structure. There are several ways in which this could be achieved. Among the most popular inversion schemes in seismic tomography gradient methods (i.e., Gauss-Newton, damped-least squares, conjugate gradients, steepest descent, subspace methods) can be cited. Most gradient methods cast the inversion problem as an optimization problem, where an objective function consisting of a misfit and some regularization terms must be minimized. Considering an L_2 norm, this objective function can be written as (Rawlinson et al., 2014):

$$S(\mathbf{m}) = (\mathbf{g}(\mathbf{m}) - \mathbf{d}_{obs})^T \mathbf{C}_d^{-1} (\mathbf{g}(\mathbf{m}) - \mathbf{d}_{obs}) + \epsilon (\mathbf{m} - \mathbf{m}_0)^T \mathbf{C}_m^{-1} (\mathbf{m} - \mathbf{m}_0) + \eta \mathbf{m}^T \mathbf{D}^T \mathbf{D} \mathbf{m} \quad (4.8)$$

Equation 4.8 is divided into three main parts. The first term on the RHS of Equation 4.8 is the misfit, which measures the disagreement between observed data $\mathbf{d}_{obs}$ and predicted data $\mathbf{g}(\mathbf{m})$; $\mathbf{C}_d^{-1}$ is a data covariance matrix, in which generally picking errors are included to give different weights to the data during the inversion. Since the data alone is generally not capable to constrain all of the model parameters in teleseismic tomography, two regularization terms are included in Equation 4.8. The second term on the RHS, $\Phi(\mathbf{m}) = (\mathbf{m} - \mathbf{m}_0)^T \mathbf{C}_m^{-1} (\mathbf{m} - \mathbf{m}_0)$, is a regularization term used in a Bayesian framework and its effect is to constrain the solution to models that are close to the reference model;

$\mathbf{C}_m^{-1}$ is a model covariance matrix, defined *a priori*, $\mathbf{m}$ and $\mathbf{m}_0$ are the current and reference model, respectively. Note that $\phi(\mathbf{m})$ is multiplied by a factor ϵ, known as damping. The third term on the RHS, $\Omega(\mathbf{m}) = \mathbf{m}^T\mathbf{D}^T\mathbf{D}\mathbf{m}$, is a regularization term adopted in a Occam's framework (Constable et al., 1987) that favors parsimony over complexity: it seeks for a model that is sufficiently smoothed but still adjusts the data. $\mathbf{D}$ is a second derivative operator and η is the smoothing factor. Because we use both Bayesian and Occam's frameworks, it is not simple to choose values for damping and smoothing factors in a quantitative way, resulting therefore in a semi-quantitative approach. We analyze the trade-off between satisfying the data and the regularization terms by inversion with differents sets of damping and smoothing, ranging from 0 to 1000. To choose the appropriate value for ϵ, we set η to zero and vary ϵ within this interval, generating an L-curve (Figure 4.3a). A similar procedure is performed to pick the optimal value of η, by setting ϵ to zero and varying η within the same interval (Figure 4.3b). Then each curve is analyzed to select the optimal value for each parameter: we find that $\eta = 10$ and $\epsilon = 10$ are optimal parameters, and use these values as damping and smoothing parameters for every period, in order to ensure consistency. Figure 4.3 presents L-curves for 15 s period Rayleigh waves.

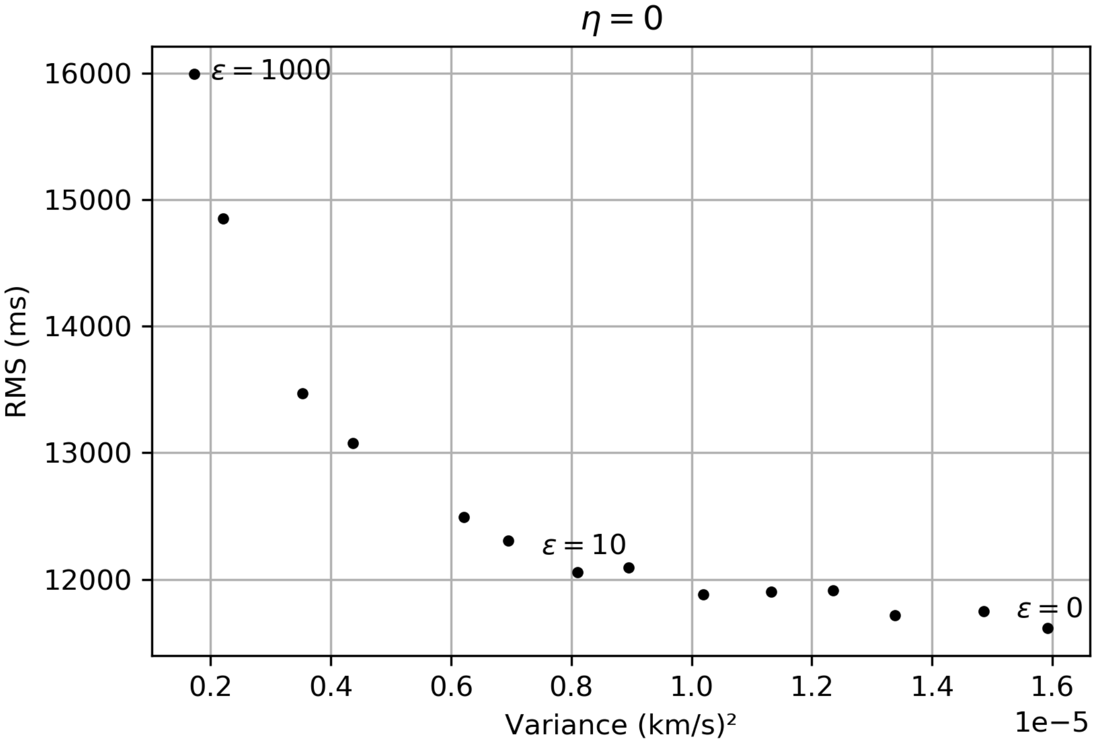

(a) Each dot on the curve is constructed by setting η to zero and varying ϵ from 0 to 1000. $\epsilon = 0$ is too small, $\epsilon = 10$ is optimal, and $\epsilon = 1000$ is too large.

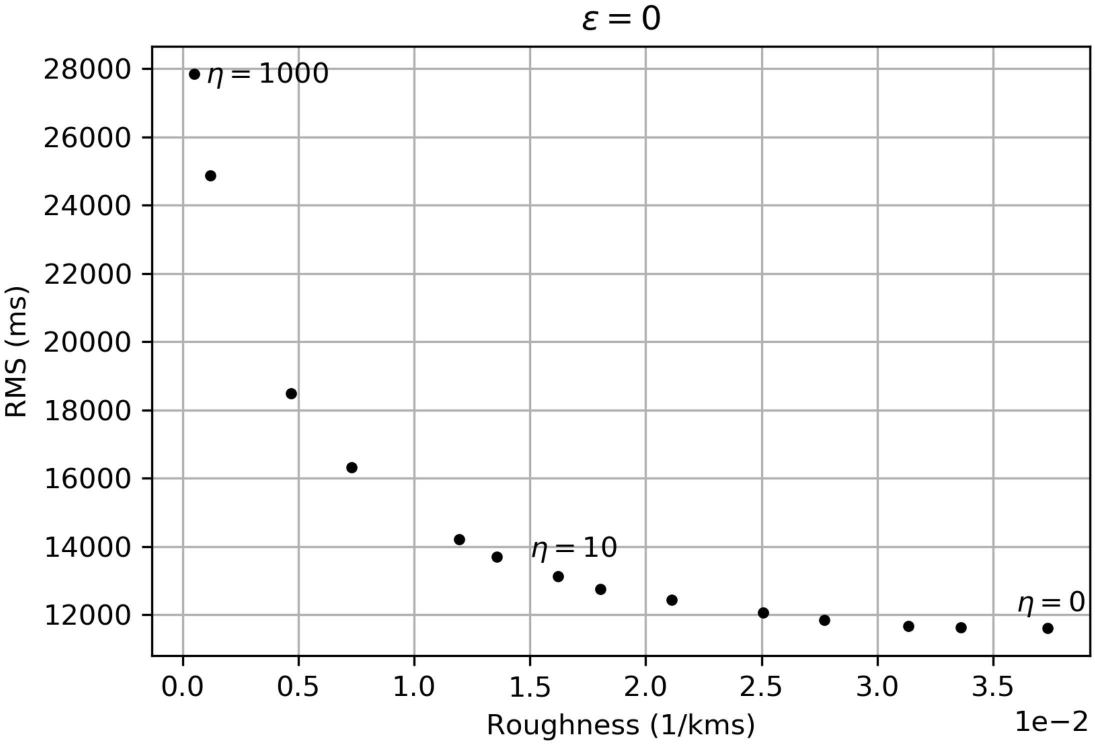

(b) Each dot on the curve is constructed by setting ϵ to zero and varying η from 0 to 1000. $\eta = 0$ is too small, $\eta = 10$ is optimal, and $\eta = 1000$ is too large.

Figure 4.3: L-curves for 15 s period Rayleigh waves.

Following Rawlinson and Sambridge (2003), if we assume that $S(\mathbf{m})$ is sufficiently smooth, we can use a truncated Taylor series to make a local quadratic approximation about some current model:

$$S(\mathbf{m} + \delta\mathbf{m}) = S(\mathbf{m}) + \hat{\boldsymbol{\gamma}}\delta\mathbf{m} + \frac{1}{2}\delta\mathbf{m}^T\hat{\boldsymbol{H}}\delta\mathbf{m} \tag{4.9}$$

where $\delta\mathbf{m}$ is the perturbation, $\hat{\boldsymbol{\gamma}}$ is the gradient vector and $\hat{\boldsymbol{H}}$ is the Hessian matrix, given respectively by:

$$\hat{\boldsymbol{\gamma}} = \frac{\partial S}{\partial \mathbf{m}} = \mathbf{G}^T\mathbf{C}_d^{-1}(\mathbf{g}(\mathbf{m}) - \mathbf{d}_{obs}) + \epsilon\mathbf{C}_m^{-1}(\mathbf{m} - \mathbf{m}_0) + \eta\mathbf{D}^T\mathbf{D}\mathbf{m} \tag{4.10}$$

$$\hat{\boldsymbol{H}} = \frac{\partial^2 S}{\partial \mathbf{m}^2} = \mathbf{G}^T\mathbf{C}_d^{-1}\mathbf{G} + \nabla_{\mathbf{m}}\mathbf{G}^T\mathbf{C}_d^{-1}(\mathbf{g}(\mathbf{m}) - \mathbf{d}_{obs}) + \epsilon\mathbf{C}_m^{-1} + \eta\mathbf{D}^T\mathbf{D} \tag{4.11}$$

where $\mathbf{G} = \frac{\partial \mathbf{g}}{\partial \mathbf{m}}$ is the Fréchet matrix of partial derivatives, in our case calculated by the FMM. To minimize Equation 4.8, an iterative approach is required until $S(\mathbf{m})$ is stabilized:

$$\mathbf{m}_{n+1} = \mathbf{m}_n + \delta\mathbf{m}_n \tag{4.12}$$

To calculate the perturbation about the current model, $\delta\mathbf{m}$, we apply a subspace scheme, briefly described below. For more information on subspace method, please refer to Kennett et al. (1988), Sambridge (1990) and Rawlinson and Sambridge (2003).

4.4.1 Subspace method

Subspace methods rely on minimization of S by projecting Equation 4.9 onto a subspace defined by a projection matrix $\mathbf{A}$ composed by n M-dimensional basis vectors $\mathbf{a}^j$, and the perturbation about the current model may be written as:

$$\delta\mathbf{m} = \sum_{j=1}^{n} \mu_j \mathbf{a}^j = \boldsymbol{A}\boldsymbol{\mu} \tag{4.13}$$

where every μ_j is the length of the respective $\mathbf{a}_j$ vector. Substituting Equation 4.13 into Equation 4.9:

$$S(\mathbf{m}+\delta\mathbf{m}) = S(\mathbf{m}) + \sum_{j=1}^{n} \mu_j \hat{\boldsymbol{\gamma}}\mathbf{a}^j + \frac{1}{2}\sum_{j=1}^{n}\sum_{k=1}^{n} \mu_j\mu_k(\mathbf{a}^k)^T \hat{\boldsymbol{H}}(\mathbf{a}^j) \tag{4.14}$$

Derivating and equaling to zero to find the minimum of Equation 4.14:

$$\frac{\partial S(\mathbf{m})}{\partial \mu_j} = \hat{\boldsymbol{\gamma}}\mathbf{a}^j + \sum_{k=1}^{n} \mu_k(\mathbf{a}^k)^T \hat{\boldsymbol{H}}(\mathbf{a}^j) = 0 \tag{4.15}$$

In terms of the perturbation coefficients $\boldsymbol{\mu}$:

$$\boldsymbol{\mu} = -(\mathbf{A}^T\hat{\boldsymbol{H}}\mathbf{A})^{-1}\mathbf{A}^T\hat{\boldsymbol{\gamma}} \tag{4.16}$$

Substituting Equations 4.16 and 4.11 into Equation 4.13:

$$\delta\mathbf{m} = -\mathbf{A}(\mathbf{A}^T(\mathbf{G}^T\mathbf{C}_d^{-1}\mathbf{G} + \epsilon\mathbf{C}_m^{-1} + \eta\mathbf{D}^T\mathbf{D})\mathbf{A})^{-1}\mathbf{A}^T\hat{\boldsymbol{\gamma}} \tag{4.17}$$

The combination of FMM to solve the forward step with a subspace method to solve the inverse step provides a stable and robust means for obtaining group velocity lateral variation maps.

4.5 Resolution assessment

To qualitatively assess the lateral resolution of our tomographic maps, we have performed a number of a variant of the checkerboard test in which there is some spacing between the alternating high and low-velocity anomalies - it can be regarded as a combination of checkerboard and spike tests. In this type of test, we generate a synthetic dataset through an alternating pattern of high and low-velocity anomalies, using the same source-receiver distribution as in our observed dataset. A maximum perturbation of 0.8 km/s is chosen. To simulate sources of error (e.g., mislocation of events, noise, etc) present in the data, a Gaussian noise component is added to each path, with a large standard deviation of 6 s. An inversion of this synthetic dataset with the subspace method is then carried out using the same parameters (e.g., grid spacing, damping, smoothing) as the actual inversion. Synthetic test results are presented in Fig. 4.4 for periods of 15, 50 and 100 s, with alternating anomalies of 2° x 2°, 3° x 3° and 4° x 4°, respectively.

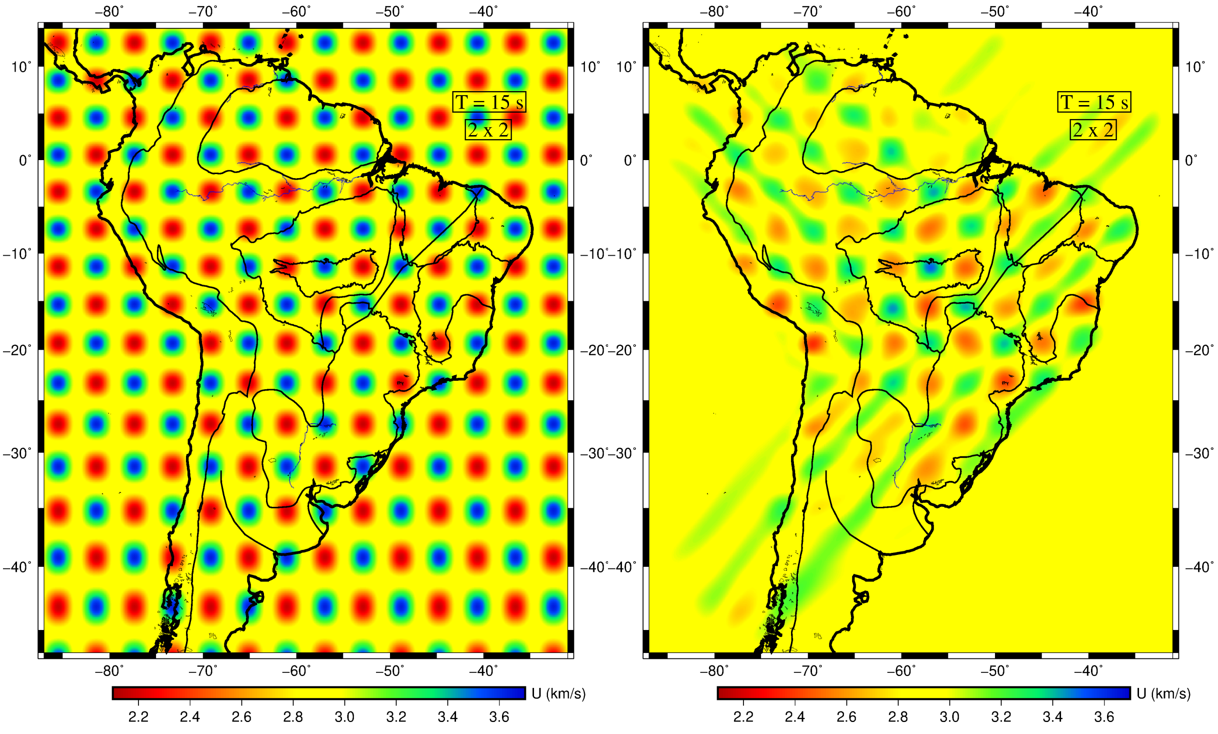

(a)

(b)

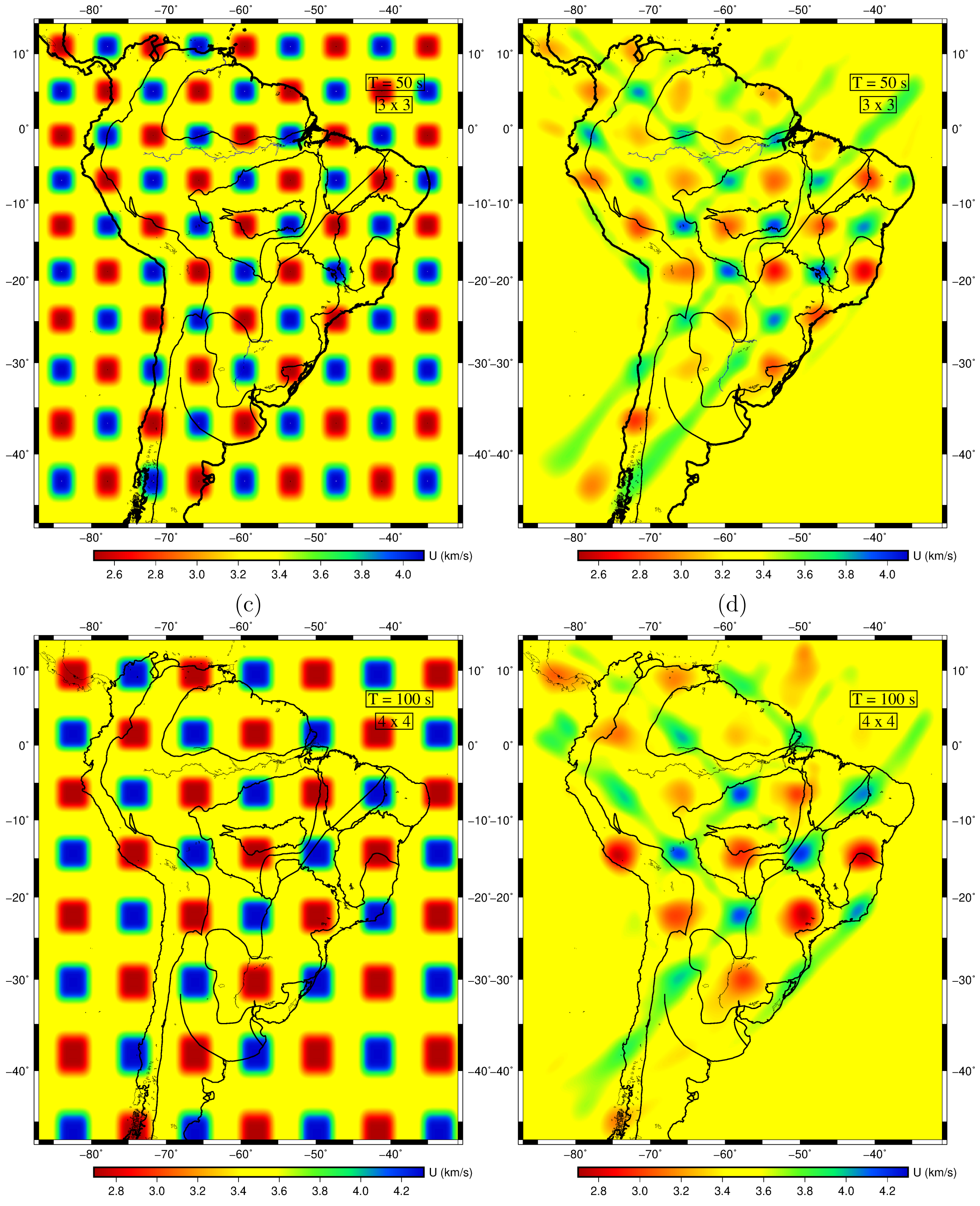

(c)

(d)

(e)

(f)

Figure 4.4: Results of the checkerboard tests. Left column panels (a, c, e) are the input models and right column panels (b, d, f) are the output models obtained from inversion with the same parameters as the inversion of the observed dataset. Each figure shows the respective period and anomaly size.

As pointed out by Lévěque et al. (1993), checkerboard test results can be misleading and should be interpreted with caution, because small scale structure may be well retrieved by the test while longer scale structure is poorly resolved. We address this problem by varying the size of the anomalies from 2° x 2° to 4° x 4°. In fact, checkerboard tests are still widely used (e.g., Rawlinson et al., 2011; Fang et al., 2016) and can provide useful insights on model resolution.

In general, the velocity anomalies were well recovered by the tests, but amplitude loss to some extent can be seen in all retrieved models, probably caused by the smoothing and damping regularization terms included in the inversion. Some smearing effects are also present, especially in areas devoid of receivers and/or sources (see Figure 3.2) such as southern Argentina (especially the Patagonian block) and parts of the oceans that are sampled by a small number of rays.

Chapter 5

Surface wave group velocity tomography of the South American continent

This chapter presents an article with results and discussion of our surface wave tomographic model of the South American continent.

5.1 Abstract

Based on new data from permanent and temporary networks, we present new tomographic images of the South American continent, constructed from inversion of fundamental mode group velocities of Rayleigh waves. An iterative combination of the Fast Marching Method to solve the direct step with a subspace method to solve the inverse step takes into account the nonlinearity of the tomographic problem and is used to obtain group velocity maps in the period range 10-150 s. A maximum of $\sim$ 17000 measurements was achieved at 30 s period and data from 282 stations were employed. The lateral resolution of our model is assessed by synthetic checkerboard tests, where the size of the anomalies is varied from 2° x 2° to 4° x 4° in each test. Those tests showed that the synthetic velocity anomalies were generally well recovered, despite the presence of some amplitude loss and smearing effects in some portions of the model, probably caused by the inclusion of regularization terms and areas devoid of stations, respectively. In our results, there is a great correlation between short period maps and surface geology, where regions of exposed basement are related to high velocities, while sedimentary basins present low velocities. Long period maps sample lithospheric depths, revealing that old and stable cratonic areas of South America, such as the Amazonian and São Francisco Cratons, correlate well with high velocities. Limits for the São Francisco Paleocontinental Block and for the Paranapanema Block are also proposed based on our 100 and 150 s period maps and are consistent with gravity anomalies and with the limits recently proposed by Rocha et al., derived from body wave tomography. Several low-velocity anomalies are consistent with regions of concentration of intraplate seismicity in the South American Platform, including the Goiás-Tocantins Seismic Zone, the Pantanal Basin and the Borborema Province, which suggests that lithospheric thinning plays a key role on intraplate seismicity.

5.2 Introduction

The lithosphere of South America can be roughly divided into a relatively stable portion — the South American Platform, which occupies most of the territory of the continent — that is not affected by the Andean and Caribbean orogeneses and is surrounded by them; the Andean Phanerozoic Fold Belt on the west and north; and the Patagonian Block, a microcontinent with evolution independent from the rest of South America, located on its southern portion and bounded by the Andes on the west and by the Atlantic Ocean on the east (Almeida et al., 2000). Figure 5.1 shows the main geotectonic provinces of South America.

South America underwent a complex geological evolution, such that its present geological and geographical configuration is the result of a long series of Wilsonian orogenic cycles. In order to better understand the tectonic evolution of a continent, it is necessary to grasp how it is structured today, at both shallow and deep scales. In this context, seismological methods, and especially seismic tomography provide the best means for indirectly studying the Earth's deep interior.

The lithospheric structure of South America has been imaged by many tomographic studies, using body and surface waves, at local and regional scales. For example, the Paraná Basin, in southern Brazil, has been an object of study of several tomographic works. The study of VanDecar et al. (1995) presented the first local tomographic model in Brazil, using P- and S-waves, and imaged parts of the São Francisco Craton and the Paraná Basin. The most astonishing feature in their model is a low-velocity anomaly in a cylinder-like shape, which was interpreted as a thermal conduit of the plume that supplied the Paraná plume head, responsible for the Paraná flood basalts. The dimensions of this low-velocity anomaly were estimated as about 300 km across, between depths of 200 to 500-600 km. Schimmel et al. (2003) inverted a larger dataset, confirmed the presence of the low-velocity anomaly beneath the Paraná Basin, and suggested that it may be confined to the upper mantle. Liu et al. (2003), however, based on results of common conversion point receiver functions (used to study deep discontinuities of the mantle, mainly the 410 and 660-km second-order discontinuities), showed that there is no perturbation in the transition zone thickness, indicating that either the low-velocity anomaly does not extend to the mantle transition zone or it is rather compositional than thermal.

Rocha et al. (2011) presented a model for central and SE Brazil from travel time tomography of P- and S-waves. They included more stations and paths to their data set compared to previous studies, which allowed to image several new features of the São Francisco Craton and the Paraná Basin. Due to the increased resolution, the 150-km depth velocity map of the basin can be roughly correlated with a suture zone model for its basement, proposed by Milani and Ramos (1998). In the São Francisco Craton, a high-velocity anomaly extends westward beyond the geological surface limit, supporting a hypothesis that the craton was part of a larger plate from the Neoproterozoic (e.g., Alkmim et al., 1993).

Body wave seismic tomography was also employed to infer the relationship between low velocity anomalies, spots of thin lithosphere and intraplate seismicity in central Brazil by Assumpção et al. (2004), Azevedo et al. (2015) and Rocha et al. (2016). All of those results were restricted to relatively small portions of Brazil and neighboring countries. The first body wave tomography study comprising the entire Brazilian territory was made by Azevedo (2017).

Although seismic tomography using surface waves has poorer resolution when compared to body waves, due to their inherent longer wavelengths, they are strongly dispersive in inhomogeneous media and travel along the surface of the Earth, thus allowing a good sampling (path coverage), especially in areas that are otherwise devoid of seismic stations and/or large earthquakes (Romanowicz, 2002).

When compared to other continents such as North America or Europe, seismic station coverage in South America is rather scarce, especially in regions with low population density or hard to access, such as the Amazon rainforest. This scarceness leads to limitations in seismological models representing the continent, where small scale structures may not be retrieved. However, previous surface wave tomography studies in South America (e.g., Silveira et al., 1998; Vdovin et al., 1999; Van der Lee et al., 2001; Feng et al., 2004; Heintz et al., 2005; Feng et al., 2007), relying on data from stations of the permanent global network and/or stations of temporary networks, have successfully mapped most regional large scale features. Those studies tend to agree on the large scale structures, such as high seismic velocities beneath cratons, but they differ in terms of resolution and consequently smaller scale features tend to disagree due to distinct datasets and inversion schemes.

New data can improve previous seismic tomography results, reveal smaller-scale features that haven't been imaged before, and increase model resolution. From 2011 to 2014 several new stations have been deployed in Brazil by the following institutions: University of São Paulo (USP), University of Brasília (UnB), University of Rio Grande do Norte (UFRN) and National Observatory (ON). Those stations constitute the Brazilian Seismographic Network (RSBR), which comprises four sub-networks: BL (USP), BR (UnB), NB (UFRN), ON (ON) (Bianchi et al., 2018). Besides earthquake location in Brazil, data from the RSBR can be used in studies concerning the Earth's subsurface beneath South America, providing models with better resolution than previous works, especially in regions with previous little monitoring, such as the Amazon rainforest. A new project named 3-Basin project, funded by São Paulo State Research Foundation, also allowed the deployment of several new temporary seismic stations in the region of the Paraná, Chaco-Paraná and Pantanal Basins. Those stations comprise the XC network and significantly improve coverage in southwestern South American Platform.

Based on the new data and on an iterative inversion scheme of surface waves that allows the nonlinearity of the tomographic problem to be taken into account, our objective is to generate a better constrained model that represents the deep structure of the South American continent. More specifically, we use a denser path coverage (our maximum number of group velocity measurements is nearly three times larger than the one of the previous study by Feng et al. (2004, 2007)), allowed by the new data, to produce group velocity lateral variation maps of Rayleigh waves in the period range 10-150 s. Those maps are then interpreted in terms of the main aspects of the lithosphere of South America, such as its cratonic blocks and intraplate seismicity.

5.3 Geological setting

Almeida et al. (2000) define the South American Platform as the stable portion of the homonym plate that is relatively not affected by the Andean and Caribbean orogeneses.

Besides relative stability compared to the surrounding mobile belts, a platform is usually characterized for antiquity - because its basement is mainly composed of Archean and Proterozoic rocks — and transitority — because of its long tectonic evolution (Almeida et al., 2000).

Throughout geological time the lithosphere of South America has been deformed and rearranged several times by Global Plate Tectonics processes, and the basement of the continent is the result of a long evolution. More specifically, the basement of the continent can be considered the product of three main orogenic events: (i) the Trans-Amazonian, during the Paleoproterozoic; (ii) the Late Mesoproterozoic and (iii) the Brasiliano/Pan African, mainly in Neoproterozoic times. The lack of data makes it difficult to determine cycles for the Archean yet (Almeida et al., 2000). Although of secondary importance to the Amazonian Craton and surroundings (Brito Neves and Fuck, 2013), the Brasiliano events resulted in the present configuration of the tectonic elements in the South America Platform, and the youngest fold belts of the basement were formed during the Neoproterozoic (Almeida et al., 2000). Those fold belts have stabilized during the Ordovician (440 Ma) and it can be said that the South American Platform is an entity of the Ordovician, but only got individualized as such during the Cretaceous, with separation between Africa and South America (Hasui, 2012).

Due to a distinct tectonic evolution, the basement of the South American Platform can be divided into two main domains: a pre-Brasiliano N-NW Amazonian Domain, where large Archean nuclei are circumscribed by younger Paleo- and Mesoproterozoic mobile belts; and a central-eastern "Brasiliano" Domain, whose structural framework was intensely shaped by Neoproterozoic orogenic cycles, namely the Brasiliano/Pan African events (Brito Neves and Fuck, 2014), that were diachronous and distributed over four pulses: i) ca. 800 - 740 Ma, ii) ca. 660 - 610 Ma, iii) ca. 590 - 560 Ma and iv) 520-500 Ma (Brito Neves et al., 2014). Brito Neves and Fuck (2014) also recognized that the crustal evolution of the Amazonian Domain shares many similarities with the ancient Laurentian continent, while the Brasiliano Domain presents affinities with Western Gondwana. Those domains are separated by a megashear zone named Transbrasiliano Lineament (TBL), which extends even further to Africa (e.g, Santos et al., 2008), to the south and by the Araguaia Fold Belt to the north (Brito Neves and Fuck, 2014).

Almeida et al. (1977, 1981) made the first proposal of division of the Brazilian territory in structural provinces. Ten provinces were recognized (see Figure 5.1 for a spatial reference): Rio Branco (part of the Amazonian Craton to the north of the Amazon Basin), Tapajós (part of the Amazonian Craton to the south of the Amazon Basin) and São Francisco Provinces, corresponding to the cratonic areas; Borborema, Mantiqueira and Tocantins Provinces, corresponding to Neoproterozoic orogens; Amazon, Paraná and Parnaíba Provinces, corresponding to large Paleozoic sedimentary basins (the Amazon Province includes both Amazon and Solimões Basins); a province corresponding to small coastal sedimentary basins. With new geochronological and geological data available, finer subdivisions have been proposed. In particular, the Brazilian Geological Survey (CPRM) (Schobbenhaus and Brito Neves, 2003; Santos, 2003) added a Parecis Province to the previously mentioned division, corresponding to the namesake basin, and divided the Amazonian Craton in seven provinces: Transamazonas (2.25 - 2.0 Ga), Carajás (3.1 - 2.53 Ga), Amazônia Central (2.6 - 1.7 Ga), Tapajós-Parima (2.1 - 1.87 Ga), Rondônia-Juruena (1.81 - 1.52 Ga), Rio Negro (1.86 - 1.52 Ga) and Sunsás (1.45 - 0.99 Ga). Because new data are always being produced, new interpretations are always being proposed and there is no absolute consensus about those subdivisions.

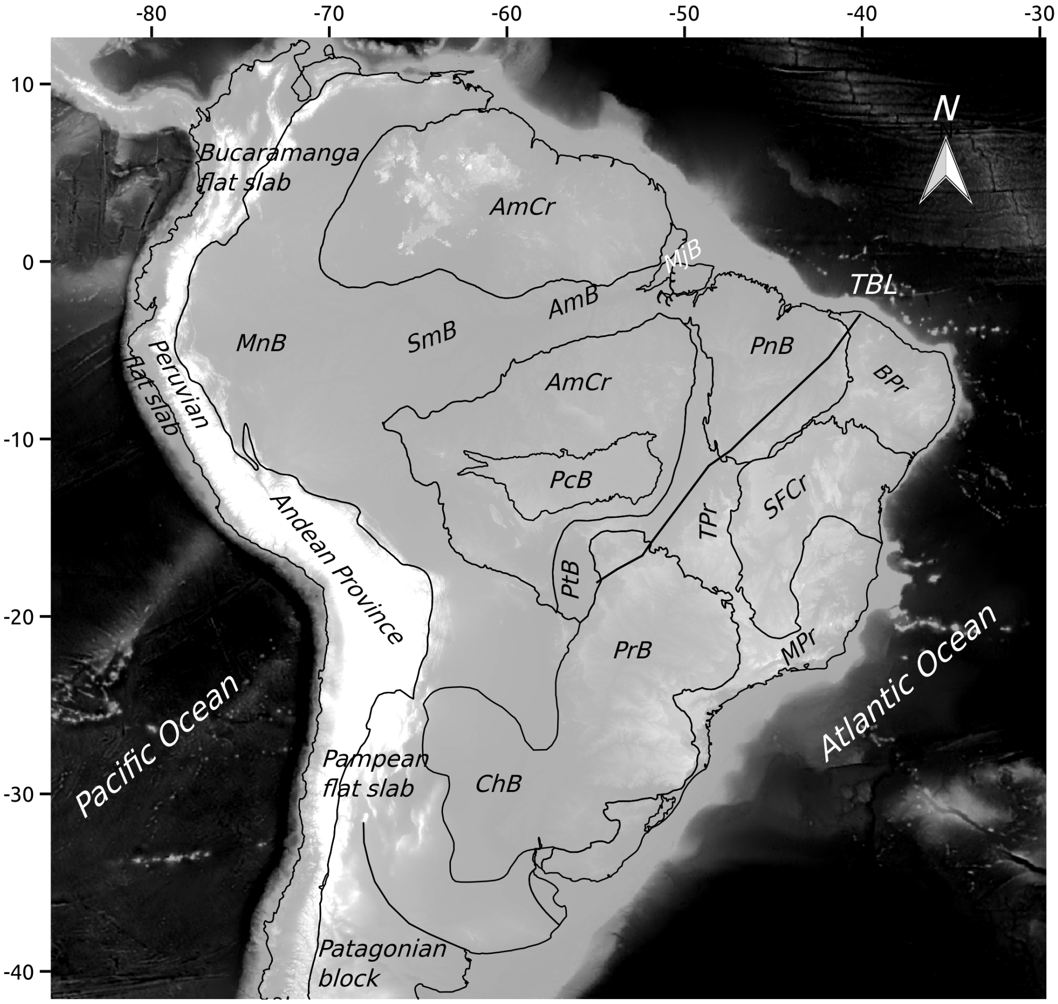

Figure 5.1: Main geotectonic provinces of South America. The solid black contours represent: AmCr - Amazonian Craton, SFCr - São Francisco Craton, BPr - Borborema Province, TPr - Tocantins Province, MPr - Mantiqueira Province, PnB - Parnaíba Basin, PrB - Paraná Basin, ChB - Chaco Basin, PtB - Pantanal Basin, PcB - Parecis Basin, MnB - Maranon Basin, SmB - Solimões Basin, AmB - Amazon Basin and MjB - Marajó Basin. TBL stands for the Transbrasiliano Lineament.

Developed along the western margin of South America, the Andes are the largest orogenic system resulting from a non-collisional environment in the world, extending more than 8000 km. The Andean mountain range is a consequence of several processes related to the subduction of Nazca plate beneath the South American plate. Gansser (1973) provided the first proposal of division for the Andes, under the plate tectonics concept, in northern, central and southern Andes. Northern and Southern Andes are characterized by an expressive occurrence of ophiolitic rocks, together with metamorphic rocks of the Jurassic and Cretaceous (Ramos, 1999; Ramos, 2009). Central Andes, on the other hand, lack those rocks and represent the Andean-type orogen (Ramos, 1999) of the classification of Dewey and Bird (1970).

Patagonia is a mass of land separated from the rest of the South American continent by a major fault and can be defined as the portion of the Terra Australis orogen (Cawood, 2005) in the continent that was not affected by Andean orogeny (Hasui, 2012). The basement of Patagonia can be divided into two massifs: Somún Cura and Deseado, with granitoids ranging from Neoproterozoic to early Paleozoic ages (e.g., Pankhurst et al., 2003). We won't discuss the Patagonian Block any further due to its limited resolution in our model.

5.4 Data and method

Our tomographic model is based on inversion of fundamental mode Rayleigh wave group velocity measurements, from vertical component seismograms of broadband seismic stations. The group velocity calculations require the coordinates and the origin time of the earthquakes to be known; this information was taken from the United States Geological Survey (USGS) bulletin, available at `https://earthquake.usgs.gov/earthquakes/search/`. We selected 1043 earthquakes from 2002 to 2019, with magnitudes larger than 5.0, source-receiver distances greater than 15° and depths down to 100 km. Those parameters were chosen empirically by testing. Boxplots of the source parameters distance, magnitude, and depth of the paths in our dataset are shown in Figure 5.2. Because we only use data from stations in South America and did not analyze paths of earthquakes from distant sources such as the Atlantic Ridge, our paths tend to have a relatively small length, and the majority of our data has source-receiver distances between 25° and 35°; path lengths longer than 50° are outliers. Usually, earthquakes with greater magnitudes have a better signal to noise ratio, and for this reason, we choose 5.0 as our minimum magnitude, instead of the cut-off value of 4.5 used by Feng et al. (2004, 2007). The median of the magnitudes in our dataset is 5.5, and most earthquakes have magnitudes between 5.0 and 6.0. In terms of depth, most events are rather shallow (depth < 30 km).

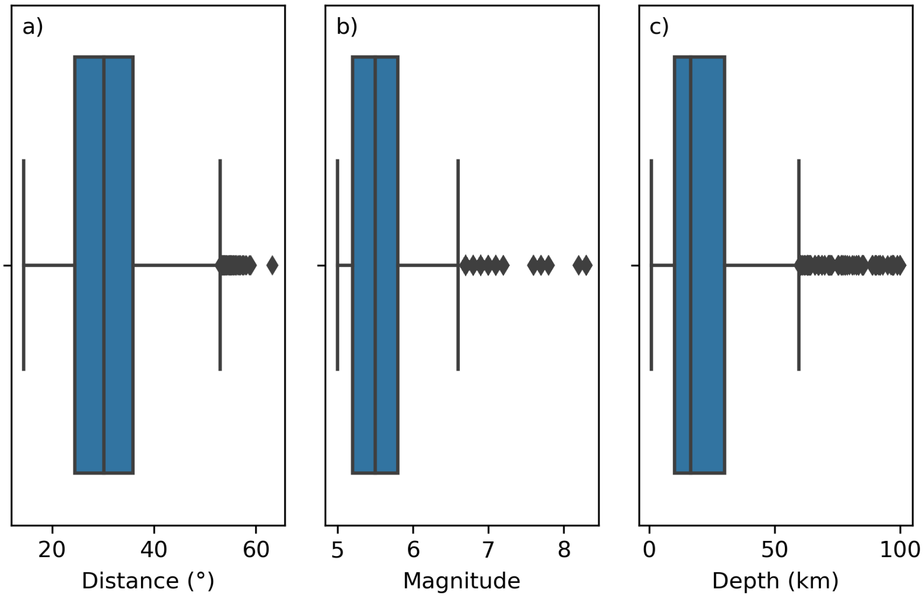

Figure 5.2: Boxplots of a) distance, b) magnitude and c) depth of the events in the dataset.

Due to its large territory, with vast forest cover in the Amazonian region, much of Brazil is not adequately seismically monitored, and most of the existing stations are concentrated in central and SE Brazil. Fortunately, this scenario is been changing since 2011 with the deployment of the Brazilian Seismographic Network (RSBR) - a network started by Universities of Brasília, São Paulo, Rio Grande do Norte, and by the National Observatory, and now funded by the Brazilian Geological Survey (Bianchi et al., 2018). Compared to previous regional studies in South America using surface wave tomography (e.g., Vdovin et al., 1999; Feng et al., 2004; Heintz et al., 2005; Feng et al., 2007; Rosa et al., 2016), the recently installed RSBR stations improve coverage, especially in northern (i.e., the Amazon) and NE Brazil, thus providing a more homogeneous station distribution and increasing resolution of future tomographic models.

Besides data from RSBR stations, we processed seismograms from stations of several other projects, both permanent (Seismological Observatory of University of Brasília network - OS, Red Sismologica Nacional - C1, Ecuador Seismic Network - EC, Global Seismograph Network - IU, Global Telemetered Seismograph Network - GT, Caribbean USGS Network - CU, GEOSCOPE - G, Red Sismologica Nacional de Colombia - CM, IRIS/IDA Seismic Network - II, Curacao Seismic Network - WC, West Central Argentina Network - WA) and temporary (Pantanal, Chaco and Paraná structural studies network - XC, 2016-; Caribbean Passive Experiment - XT, 2003-2005; Central Andean Uplift and the Geodynamics of the High Topography - ZG, 2010-2012) networks, with a total of 282 seismic stations (Figure 5.3).

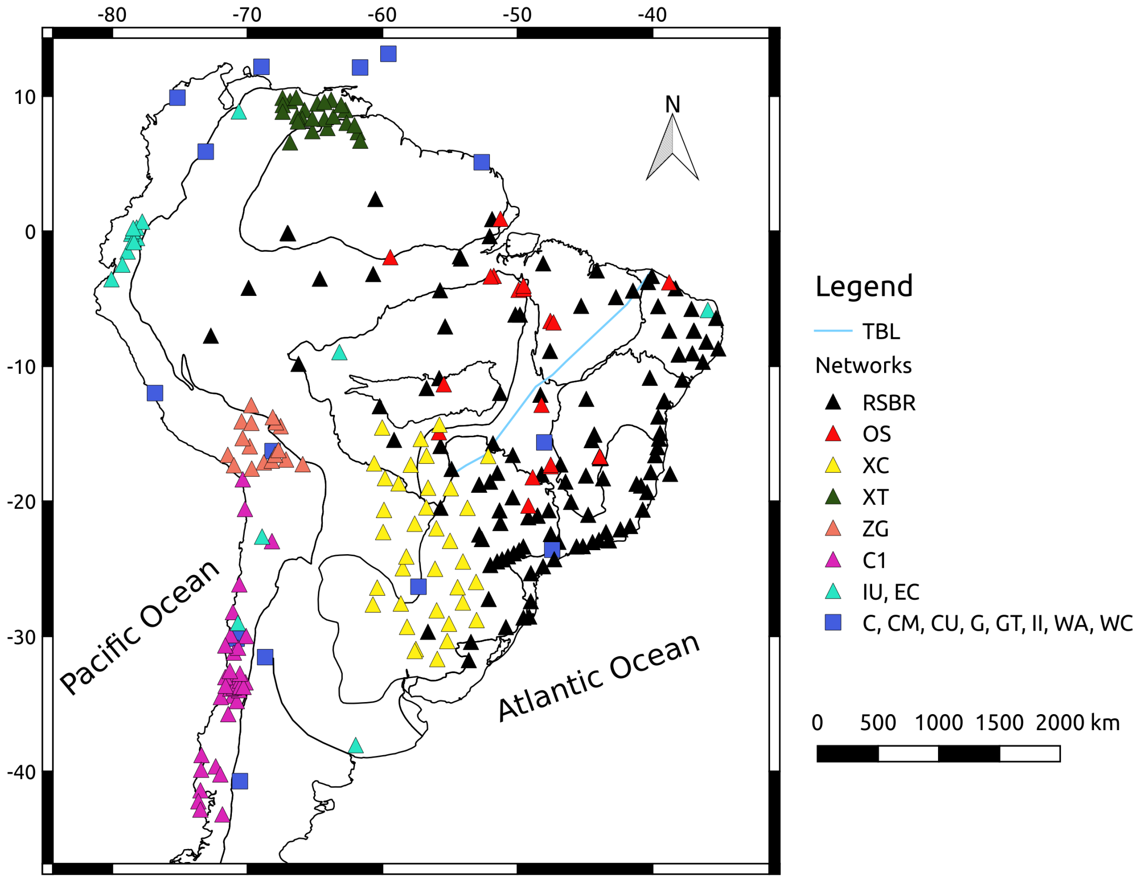

Figure 5.3: Distribution of receivers across South America. Black contours are the main geotectonic provinces of South America presented in Figure 5.1.

To measure group velocity, we employ a version of the multiple filter technique (Dziewonski et al., 1969) called multiple filter analysis, which considers instantaneous frequency instead of filter frequency to estimate group velocities; this approach minimizes a systematic error in group velocity measurement of individual recordings (Shapiro and Singh, 1999). To apply the multiple filter analysis to each seismogram, we use a software from the Computer Programs in Seismology (CPS) package, available from `http://www.eas.slu.edu/eqc/eqccps.html` (Herrmann, 2013). This program is implemented according to the theoretical background proposed by Bhattacharya (1983), but it assumes a Gaussian signal amplitude spectrum instead of a linear shape (Herrmann and Ammon, 2002). Prior to group velocity measurement, we apply pre-processing steps to each seismogram, such as band-pass filtering, trend and mean removal, taper, and instrument response correction, in order to improve its quality. Also, a phase-matched filter (Herrin and Goforth, 1977) is employed to remove higher modes.

The period range of each dispersion curve varies according to the path, depending on earthquake magnitude and source-receiver distance. This causes each period to be unevenly sampled, and the intermediate ones are better sampled by a larger number of rays. The number of measurements obtained is maximum - $\sim$ 17000 paths - for a period of 30 s, and decreases for both shorter and longer periods (Figure 5.4). Only measurements in the period range 10-150 s were inverted.

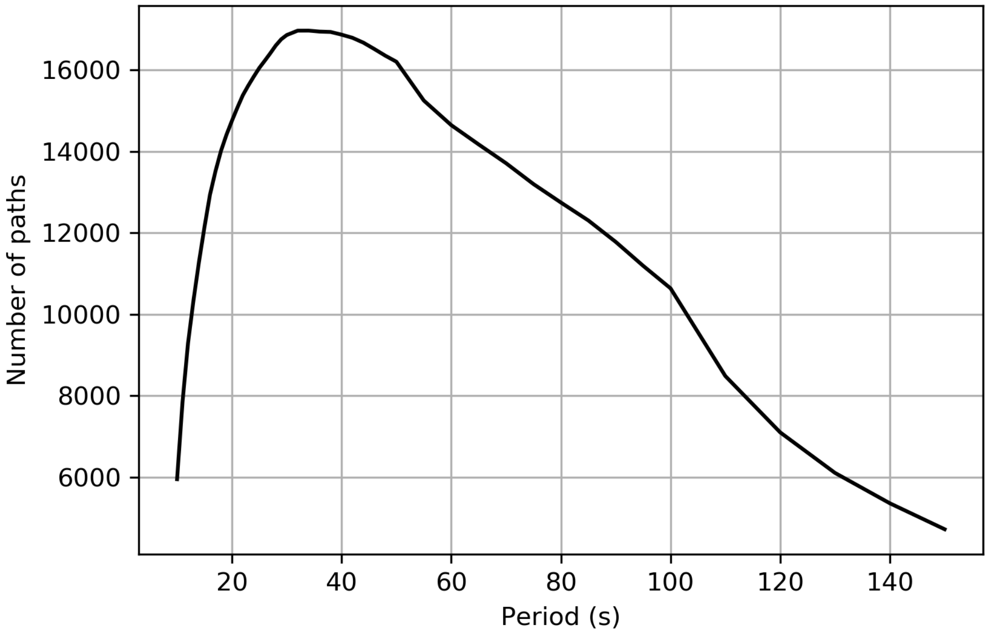

Figure 5.4: Number of path as a function of period. The number of rays is maximum at 30 s and decreases for both shorter and longer periods.

5.5 Tomographic inversion

The tomographic problem of estimating group velocity maps from dispersion curves is divided into four steps: (i) parameterization of the study area; (ii) given the model parameters, calculation of theoretical travel times through the array of sources and receivers - the forward step; (iii) adjustment of model parameters to better satisfy the observed data - the inverse step; (iv) assessment of model resolution.

We use the Fast Marching Surface Tomography (FMST) package of Rawlinson (2005) to solve the tomographic problem. In the first step, the velocity structure of the South American continent is represented by a grid of velocity nodes, with a bi-cubic B-spline interpolation function associated. An optimum balance between recovery, resolution and computational processing time was found for a grid spacing of 1° by 1°.

FMST iteratively solves the forward and the inverse steps in order to account for the non-linearity between travel time and velocity (Rawlinson, 2005). Rather than using a conventional ray tracing method, the forward problem is solved by tracking the entire wavefront through the Fast Marching Method (FMM) (e.g., Sethian, 1996; Sethian and Popovici, 1999; Rawlinson and Sambridge, 2004b; Rawlinson and Sambridge, 2005). FMM is a grid based numerical method that solves the eikonal equation via finite differences (Rawlinson and Sambridge, 2005). It was shown to be a robust method for computing travel times by several studies in seismic tomography (e.g., Rawlinson and Sambridge, 2004a, Saygin and Kennett, 2010, Dias et al., 2015) and other fields such as robotics (e.g., Liu et al., 2017). The main advantages of FMM over traditional ray tracing methods include avoiding great circle assumption, finding diffractions in shadow zones and solving wave propagation even in highly heterogeneous media (e.g., Sethian and Popovici, 1999;

Rawlinson and Sambridge, 2003). FMM is unconditionally stable due to the reinforcement of the following entropy-satisfying condition (e.g., Rawlinson and Sambridge, 2005):

$$\begin{bmatrix} max(D_a^{-x}T, -D_b^{+x}T, 0)^2 \\ +max(D_c^{-y}T, -D_d^{+y}T, 0)^2 \\ +max(D_e^{-z}T, -D_f^{+z}T, 0)^2 \end{bmatrix}^{1/2} = s_{i,j,k} \tag{5.1}$$

where (i, j, k) are grid increments in (x, y, z) directions and a, b, c, d, e, f are integers that define the order of the scheme, T is traveltime and D is the finite differences notation.

The inverse step is cast as an optimization problem, where the following objective function S($\mathbf{m}$) is to be minimized:

$$S(\mathbf{m}) = (\mathbf{g}(\mathbf{m}) - \mathbf{d}_{obs})^T \mathbf{C}_d^{-1} (\mathbf{g}(\mathbf{m}) - \mathbf{d}_{obs}) + \epsilon (\mathbf{m} - \mathbf{m}_0)^T \mathbf{C}_m^{-1} (\mathbf{m} - \mathbf{m}_0) + \eta \mathbf{m}^T \mathbf{D}^T \mathbf{D} \mathbf{m} \tag{5.2}$$

where $\mathbf{m}$ are the model parameters, $\mathbf{d}_{obs}$ are the observed travel time data, $\mathbf{g}(\mathbf{m})$ are the data predicted by the forward step, $\mathbf{C}_d^{-1}$ is a data covariance matrix, $\mathbf{m}_0$ is the reference model, $\mathbf{C}_m^{-1}$ is the covariance matrix of model parameters, $\mathbf{D}$ is a smoothing operator, ϵ and η are the damping and smoothing coefficients, respectively (Rawlinson et al., 2014). The first term on the right hand side of Equation 5.2 measures the misfit between observed and theoretical travel times. Since the solution may not be well constrained by the data alone, regularization terms are added to the objective function: the second term on the RHS favors solution models $\mathbf{m}$ that are close to the reference model $\mathbf{m}_0$ (Bayesian framework) and the third term favors smooth models over models with abrupt velocity variations (Occam's framework) (Rawlinson and Sambridge, 2003). We analyze the trade-off between satisfying the data and model complexity by inverting with differents sets of damping and smoothing coefficients (ϵ and η, respectively), ranging from 0 to 1000. To choose an appropriate value for ϵ, we set η to zero and vary ϵ within this interval, generating an L-curve (Figure 5.5a). A similar procedure is performed to pick an optimal value of η, by setting ϵ to zero and varying η within the same interval (Figure 5.5b). Then each curve is analyzed to select an optimal value for each parameter: we find that $\eta = 10$ and $\epsilon = 10$ are optimal parameters, and those values are used for all periods, in order to ensure consistency. Figure 5.5 presents L-curves for 15 s period Rayleigh waves.

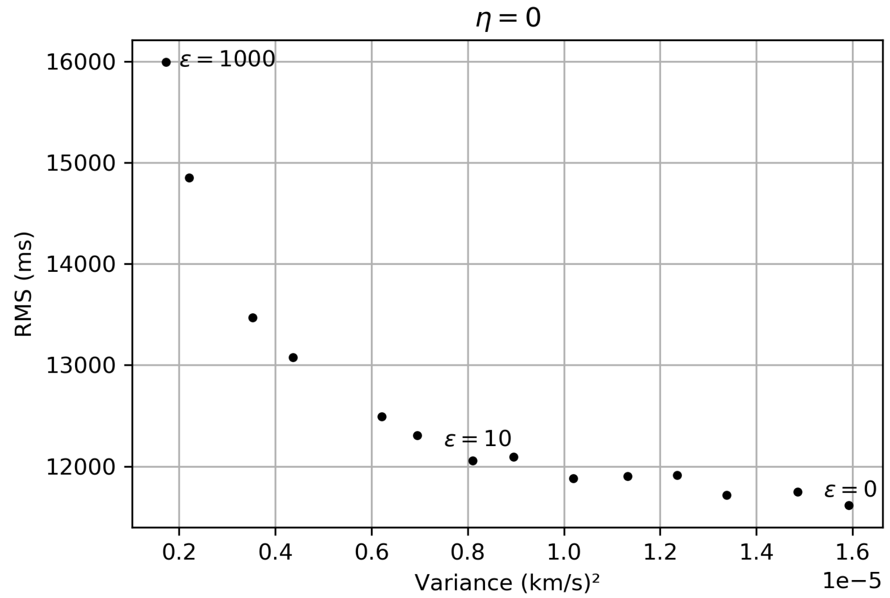

(a) Each dot on the curve is constructed by setting η to zero and varying ϵ from 0 to 1000. $\epsilon = 0$ is too small, $\epsilon = 10$ is optimal, and $\epsilon = 1000$ is too large.

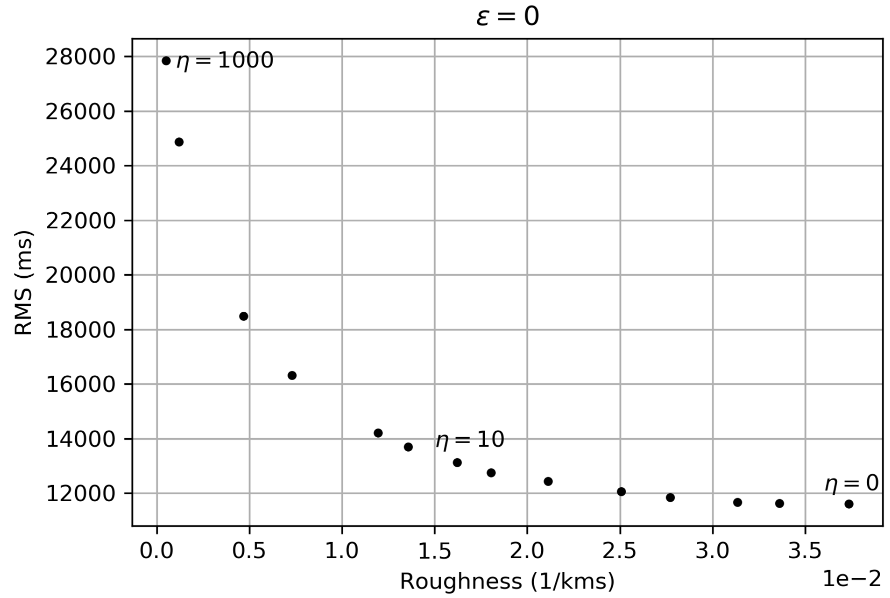

(b) Each dot on the curve is constructed by setting ϵ to zero and varying η from 0 to 1000. $\eta = 0$ is too small, $\eta = 10$ is optimal, and $\eta = 1000$ is too large.

Figure 5.5: L-curves for 15 s period Rayleigh waves.

To find the minimum of the objective function we apply a subspace scheme (e.g., Kennett et al., 1988; Sambridge, 1990), which is a gradient-based inversion method that assumes a local quadratic approximation about the current model. To reduce the computational expense of the inversion, the subspace method projects and minimizes, at each iteration, the quadratic approximation in an n-dimensional subspace of model space, and the model perturbation is given by (Rawlinson and Sambridge, 2003):

$$\delta\mathbf{m} = -\mathbf{A}(\mathbf{A}^T(\mathbf{G}^T\mathbf{C}_d^{-1}\mathbf{G} + \epsilon\mathbf{C}_m^{-1} + \eta\mathbf{D}^T\mathbf{D})\mathbf{A})^{-1}\mathbf{A}^T\hat{\boldsymbol{\gamma}} \tag{5.3}$$

where **A** is a projection matrix, **G** is the Frèchet derivatives matrix and $\hat{\boldsymbol{\gamma}}$ is the gradient vector. To illustrate how FMST accounts for wavefront distortion, Figure 5.6a shows the wavefront evolution of 15 s period waves, from an earthquake with epicenter in the Andes (represented by the red star). Triplication effects are stronger around low-velocity anomalies. Figures 5.6b and 5.6c also show histograms of traveltime residuals before (for a constant velocity model with v = 2.9 km/s) and after inversion. Before the inversion, great circle paths are assumed and are then corrected at each iteration.

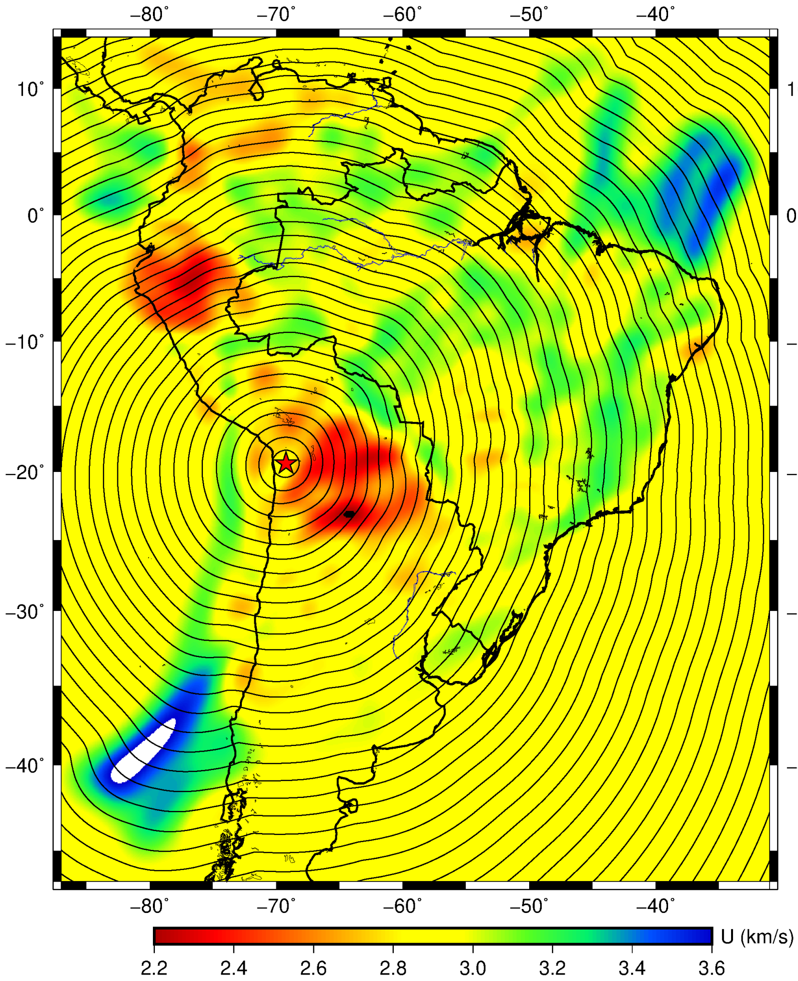

(a)

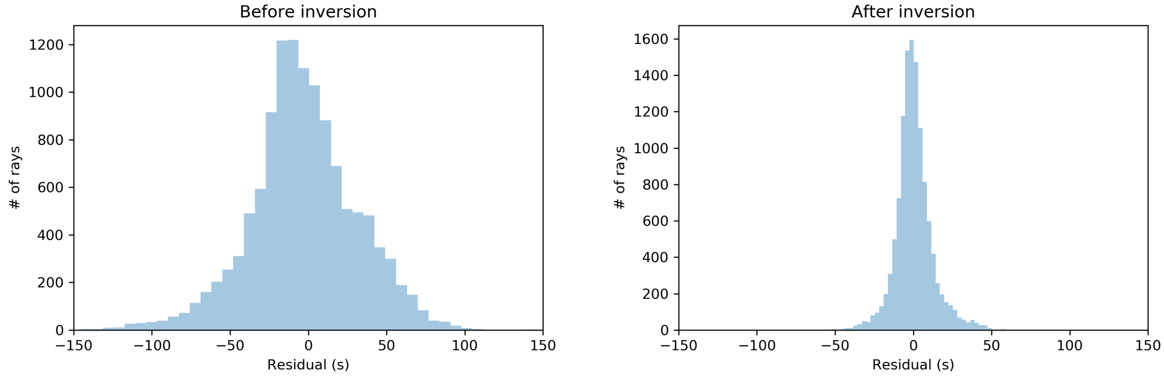

(b) (c)

Figure 5.6: a) Example of wavefront distortion for 15 s period Rayleigh waves; the epicenter of the earthquake is represented by the red star. Traveltime residuals histograms b) before and c) after inversion with the FMST package.

5.6 Synthetic tests

To qualitatively assess the lateral resolution of our tomographic maps, we have performed a number of a variant of the checkerboard test in which there is some spacing between the alternating high and low-velocity anomalies - it can be regarded as a combination of checkerboard and spike tests. In this type of test, we generate a synthetic dataset through an alternating pattern of high and low-velocity anomalies, using the same source-receiver distribution as in our observed dataset. A maximum perturbation of 0.8 km/s is chosen. To simulate sources of error (e.g., mislocation of events, noise, etc) present in the data, a Gaussian noise component is added to each path, with a large standard deviation of 6 s. An inversion of this synthetic dataset with the subspace method is then carried out using the same parameters (e.g., grid spacing, damping, smoothing) as the actual inversion. Synthetic test results are presented in Fig. 5.7 for periods of 15, 50 and 100 s, with alternating anomalies of 2° x 2°, 3° x 3° and 4° x 4°, respectively.

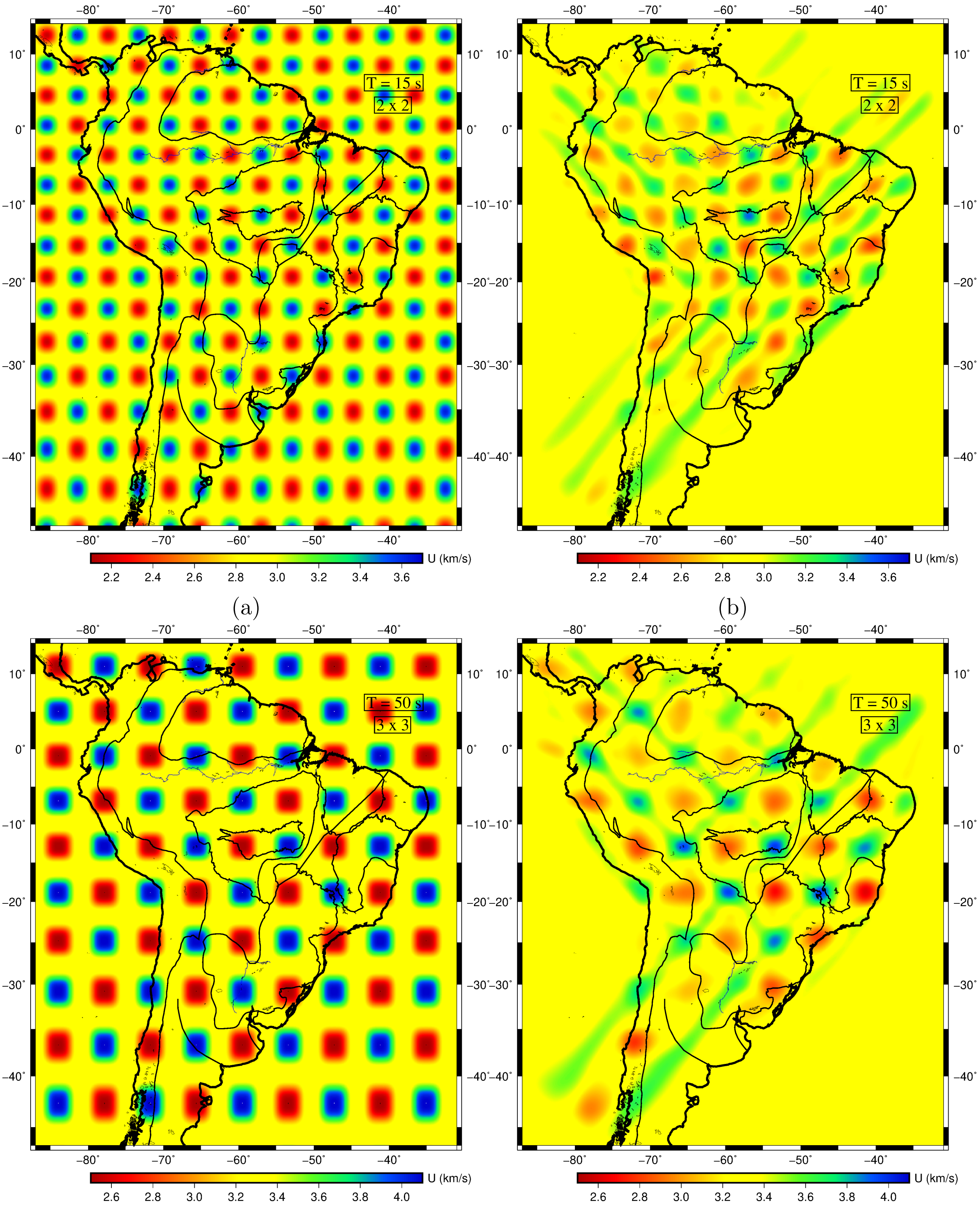
−80˚
−70˚
−60˚
−50˚
−40˚
10˚
0˚
−10˚
−20˚
−30˚
−40˚
T = 15 s
2 x 2
U (km/s)
2.2
2.4
2.6
2.8
3.0
3.2
3.4
3.6
T = 50 s
3 x 3
2.6
2.8
3.0
3.2
3.4
3.6
3.8
4.0

(a)

(b)

(c)

(d)

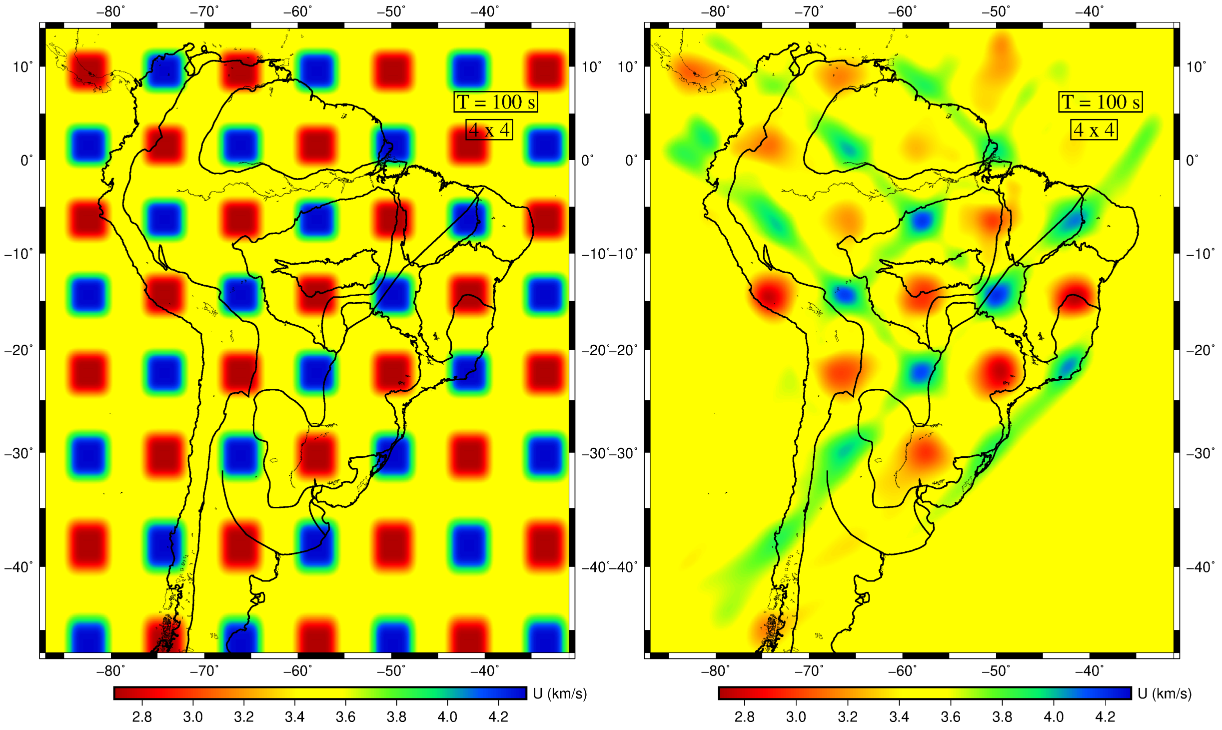

(e) (f)

Figure 5.7: Results of the checkerboard tests. Left column panels (a, c, e) are the input models and right column panels (b, d, f) are the output models obtained from inversion with the same parameters as the inversion of the observed dataset. Each figure shows the respective period and anomaly size.

As pointed out by Lévêque et al. (1993), checkerboard test results can be misleading and should be interpreted with caution, because small scale structure may be well retrieved by the test while longer scale structure is poorly resolved. We address this problem by varying the size of the anomalies from 2° x 2° to 4° x 4°. In fact, checkerboard tests are still widely used (e.g., Rawlinson et al., 2011; Fang et al., 2016) and can provide useful insights on model resolution.

In general, the velocity anomalies were well recovered by the tests, but amplitude loss to some extent can be seen in all retrieved models, probably caused by the smoothing and damping regularization terms included in the inversion. Some smearing effects are also present, especially in areas devoid of receivers and/or sources (see Figure 5.3) such as southern Argentina (especially the Patagonian block) and parts of the oceans that are sampled by a small number of rays.

5.7 Results and discussion

In this section we present 2D Rayleigh wave group velocity variation maps for periods of 10, 15, 50, 100 and 150 s (Figure 5.9); high-velocity anomalies are represented by cold colors and low-velocity anomalies are represented by hot colors. Although feasible with our path coverage, a second inversion for S-wave velocity structure is beyond the scope of this work and we use the sensitivity kernels shown in Figure 5.8 to interpret our tomographic images for different depths. This figure represents Rayleigh wave sensitivity to S-wave velocity variation with depth, and is constructed based on the AK135 (Kennett et al., 1995) velocity model. As period increases, surface waves are more affected by S-velocity variations at greater depths. For example, the sensitivity peak of 10 s period Rayleigh waves is around 10 km of depth, while the sensitivity peak of 150 s period waves is around 160 km of depth.

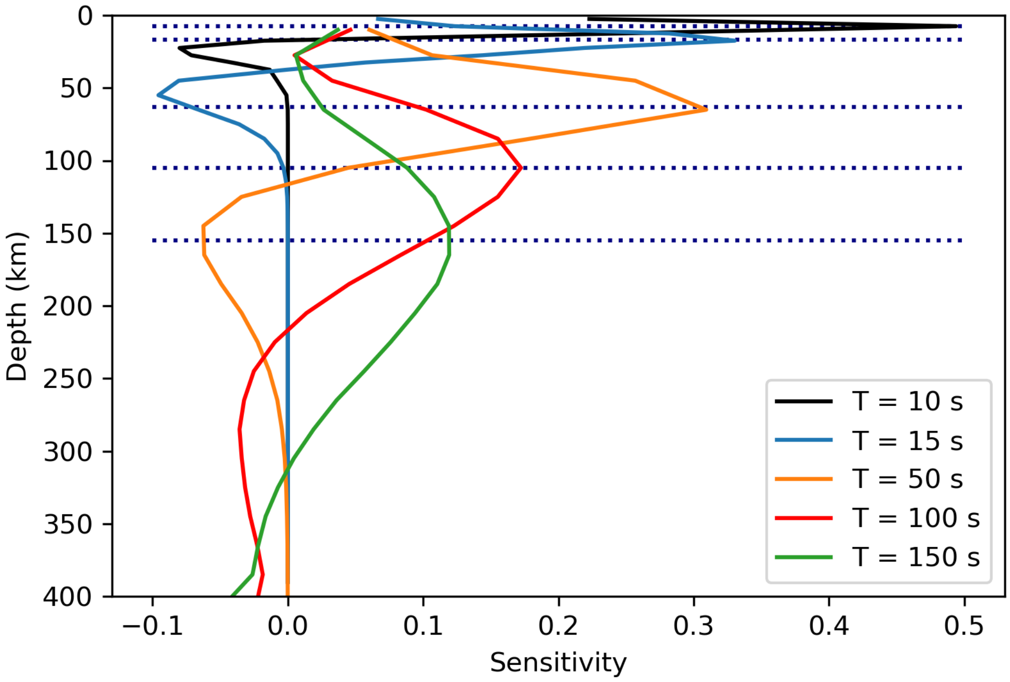

Figure 5.8: Sensitivity kernels of Rayleigh waves relative to the AK135 velocity model. Sensitivity kernels for periods of 10, 15, 50, 100 and 150 s are shown. Dotted dark blue lines are representing sensitivity peaks, that is, depths that influence the respective wave period the most.

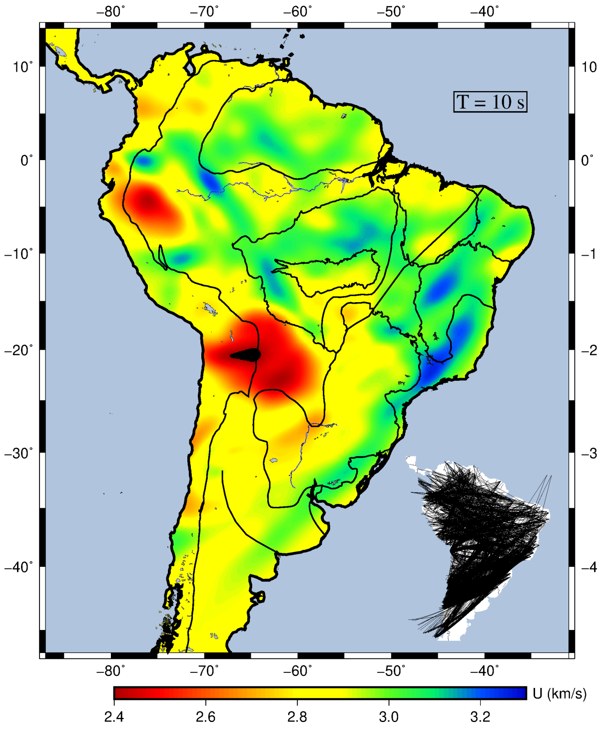
−80˚
−70˚
−60˚
−50˚
−40˚
10˚
0˚
−10˚
−20˚
−30˚
−40˚
T = 10 s
U (km/s)
2.4
2.6
2.8
3.0
3.2

(a)

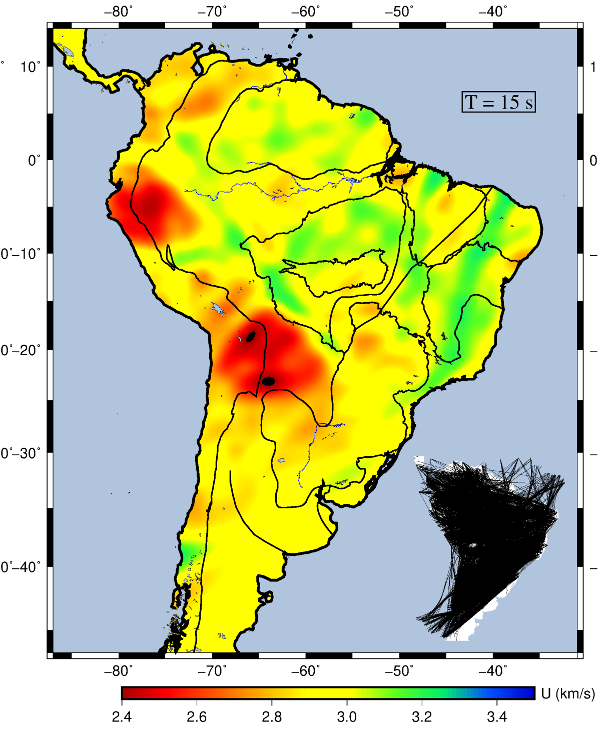
−80˚
−70˚
−60˚
−50˚
−40˚
10˚
0˚
−10˚
−20˚
−30˚
−40˚
T = 15 s
U (km/s)
2.4
2.6
2.8
3.0
3.2
3.4

(b)

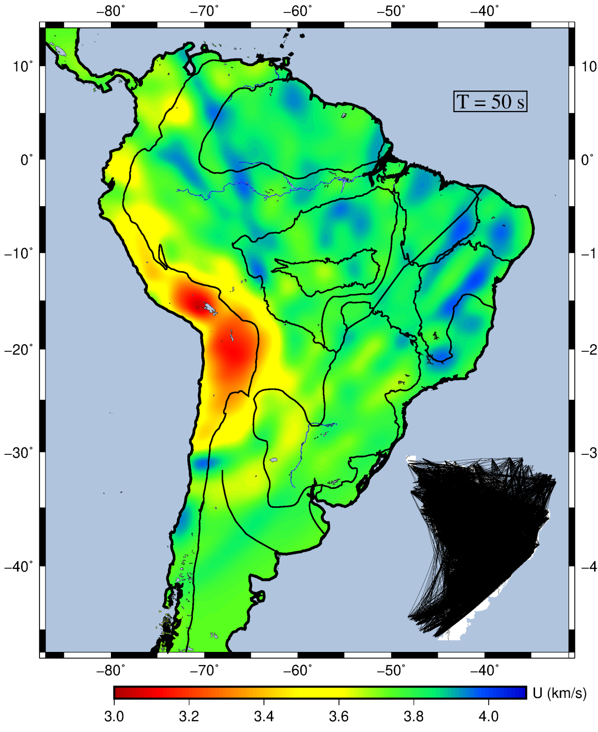
−80˚
−70˚
−60˚
−50˚
−40˚
10˚
0˚
−10˚
−20˚
−30˚
−40˚
T = 50 s
U (km/s)
3.0
3.2
3.4
3.6
3.8
4.0

(c)

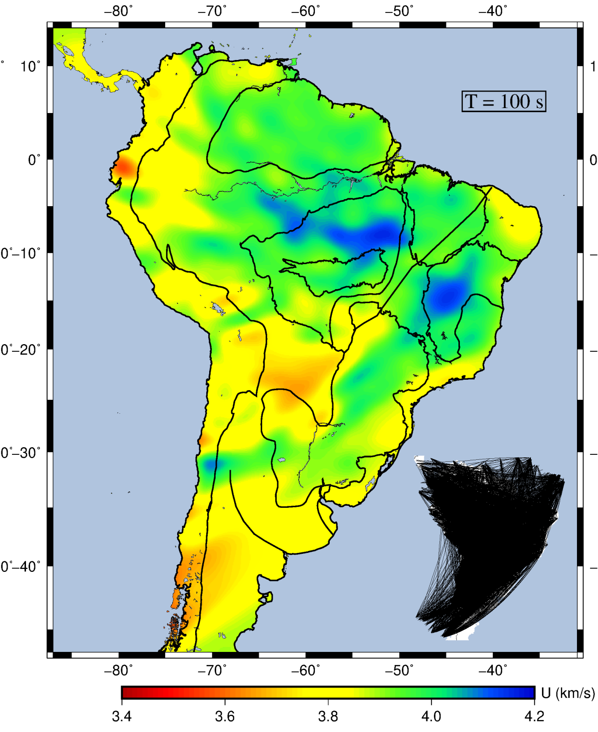
−80˚
−70˚
−60˚
−50˚
−40˚
10˚
0˚
−10˚
−20˚
−30˚
−40˚
T = 100 s
U (km/s)
3.4
3.6
3.8
4.0
4.2

(d)

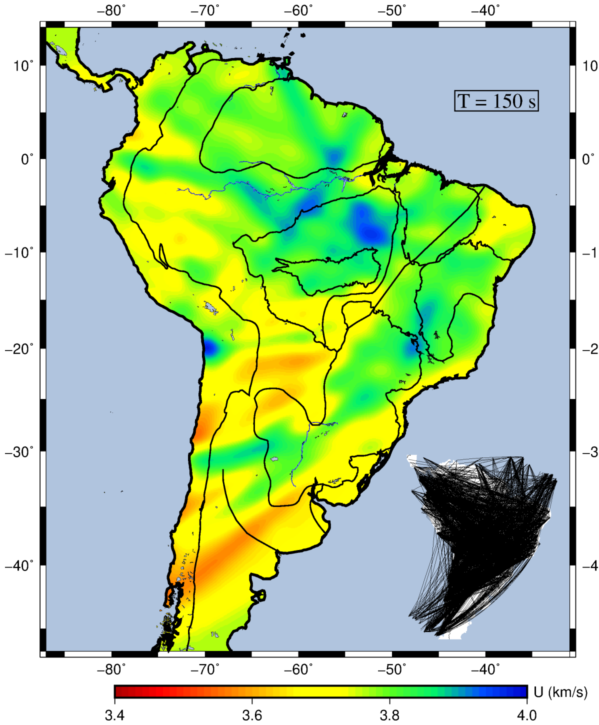

(e)

Figure 5.9: Rayleigh wave group velocity maps of South America for periods of a) 10 s, b) 15 s, c) 50 s, d) 100 s, e) 150 s. Path coverage of the respective period is represented in the right bottom corner of each panel. Cold colors represent high-velocity anomalies and hot colors represent low-velocity anomalies. Black contours are the geotectonic features of Figure 5.1.

From the sensitivity kernel, we can infer that 10 and 15 s period Rayleigh waves are mostly sensitive to shallow structure, such as basins and upper crust. Our 2D maps were constructed without any *a priori* geological information constraints, but Figures 5.9a and 5.9b present a very good correlation with surface geology, where regions of exposed basement - some portions of the cratons and Neoproterozoic fold belts - are related to high velocity anomalies. This is probably caused by a more stable and consolidated character of the basement rocks when compared to more young and loose sediments and rocks. Also, sedimentary basins - e.g., Paraná, Parnaíba, Amazonian, Solimões, Parecis, Pantanal - present a low-velocity signature. Maximum reported depth to basement across those basins is highly variable, ranging from 0.5 km at Pantanal Basin to 16 km at Marajó Basin (see Table 5.1). Therefore, regardless of sediment thickness, the mere presence of unconsolidated younger sediments seems to have a great influence on our short period maps.

Basin	**Max. thickness (km)**	**Reference**
Paraná	7	Milani and Zalan (1999), Milani and De Wit (2008)
Chaco-Paraná	5	Milani and Zalan (1999)
Parnaíba	3.5	Milani and Zalan (1999)
Amazon	5	Milani and Zalan (1999)
Solimões	5	Milani and Zalan (1999)
Parecis	1.5	Barros et al. (2011)
Pantanal	0.5	Dias et al. (2016)
Marajó	16	Zalán and Matsuda (2007)

Table 5.1: Sediment thickness of the major basins of South America.

The lowest velocities at 10 and 15 s are found beneath the Andes, especially beneath the highest topography of the South American continent (-20°, -68°). Since 15 s period waves are also sensitive to the upper crust, we believe that this may be caused by the thick crust beneath the Andes.

A local study by Dias et al. (2015) using ambient noise tomography in the Borborema Province, NE Brazil, found a great correlation between group velocity variation maps ranging from 5 to 20 s and surface geology, namely a small velocity anomaly at short periods corresponding to the Tucano-Jatobá rift basin (southern Borborema Province, ∼ -10°, -37°) and higher velocity anomalies elsewhere. Even though derived from teleseismic earthquake data with larger errors associated, our 10 and 15 s maps present a correlation with their model, and the Tucano-Jatobá basin is represented, at 10 s, by a low-velocity anomaly with some extent of smearing effects, due to a lower resolution.

At 50 s, Rayleigh waves are sensitive to crustal velocity and thickness (Figure 5.8) and the seismic anomalies are inversely correlated to Moho depth: low-velocity anomalies correspond to great Moho depth while high velocities correspond to a thinner crust. The most astonishing feature of Figure 5.9c is a low-velocity anomaly beneath the Andes Cordillera, in a region where Moho depth reaches 70 km (around -20°, -70°) (Rivadeneyra-Vera et al., 2019).

At 100 and 150 s mainly lithospheric depths are sampled. In Brazil, most of the Neoproterozoic orogens are underlain by low velocities, while high velocities are found beneath the Amazon and São Francisco Cratons and portions of the Paraná and Parnaíba Basins. A low-velocity trend parallel to the Transbrasiliano Lineament was imaged, extending to the border of the Parnaíba Basin.

An extra component of non-uniqueness is added to the inversion procedure when it comes to interpreting the result of a tomographic inversion. Velocity perturbations can be attributed either to temperature, composition or pressure variations. As shown by Trampert et al. (2001) for lower mantle depths, a quantitative approach to determine the sensitivity of P- and S-wave anomalies relative to each parameter requires a realistic determination of the respective error bars, which are usually unknown. Therefore, more qualitative approaches are used to interpret seismic tomography results. Typically, at mantle depths, velocity perturbations are assumed to be caused by temperature variations (e.g., VanDecar et al., 1995; Goes et al., 2000; Cammarano et al., 2003). Even for cratonic roots, Kaban et al. (2003) have shown that temperature is predominant over composition. Short period surface waves are strongly sensitive to shallow structure such as sediments and exposed basement (see Figures 5.1, 5.9a and 5.9b), and therefore the composition factor is more important. As period increases and mid-crustal depths are sampled, temperature influence increases (Saygin and Kennett, 2010). Therefore, we assume that composition is more important for short and intermediate periods (10, 15 and 50 s) while temperature has a greater influence on longer periods (100 and 150 s).

5.7.1 Intraplate seismicity

A remarkable evolution of knowledge concerning intraplate seismicity has been achieved during recent years. However, the causes of intraplate seismicity are still not fully understood, as epicenters are not necessarily related to known surface geological features such as faults, and although there are clear concentrations of earthquakes in some areas, the reason for such behavior is not obvious at first glance. To explain the observed seismicity in stable continental areas two main types of models have been proposed: (i) models involving weak zones such as extended crust in continental margins or aborted rifts (e.g., Johnston, 1989), (ii) models related to stress concentration in the crust (e.g., Talwani and Rajendran, 1991; Assumpção and Araujo, 1993); this stress concentration is often caused by lateral density variations.

Schulte and Mooney (2005) have demonstrated that if interior rifts/taphrogens and rifted continental margins are taken into consideration, then more than half of intraplate seismicity tend to occur in areas of extended crust. However, if continental margins are not considered, then the number of earthquakes associated with non-rifted crust exceeds the ones associated with interior rifts and taphrogens. Therefore, reasons other than extended crust must have a great influence on mid-plate seismicity. On the other hand, intraplate earthquakes are unevenly distributed and tend to be concentrated in some areas.

In Central Brazil, along the Tocantins Province, a NE-SW trend of earthquakes is observed, roughly parallel to the Transbrasiliano Lineament, forming the Goiás-Tocantins Seismic Zone (GTSZ). Assumpção and Sacek (2013) argued that GTSZ may not be related to the TBL, because they are not exactly coincident and, although TBL extends beneath the Parnaíba Basin, there is no significant seismic activity in this basin accompanying the lineament. However, they noted a strong correlation between earthquake distribution and isostatic gravity anomaly and proposed that flexural deformation plays an important role in stress concentration in the upper crust beneath Central Brazil.

Figure 5.10 shows epicenter distribution of intraplate earthquakes in Brazil from 1922 to 2013 (available at `http://rsbr.gov.br/catalogo_sb.html`). In order to decrease bias caused by different population density and number of stations through time and space, we uniformize the epicenter catalog according to the criteria defined by Assumpção et al. (2004). This catalog is composed of both historical and instrumentally detected events, and it should be emphasized that it is somewhat biased in northern Brazil due to scarce receiver distribution and low population density.

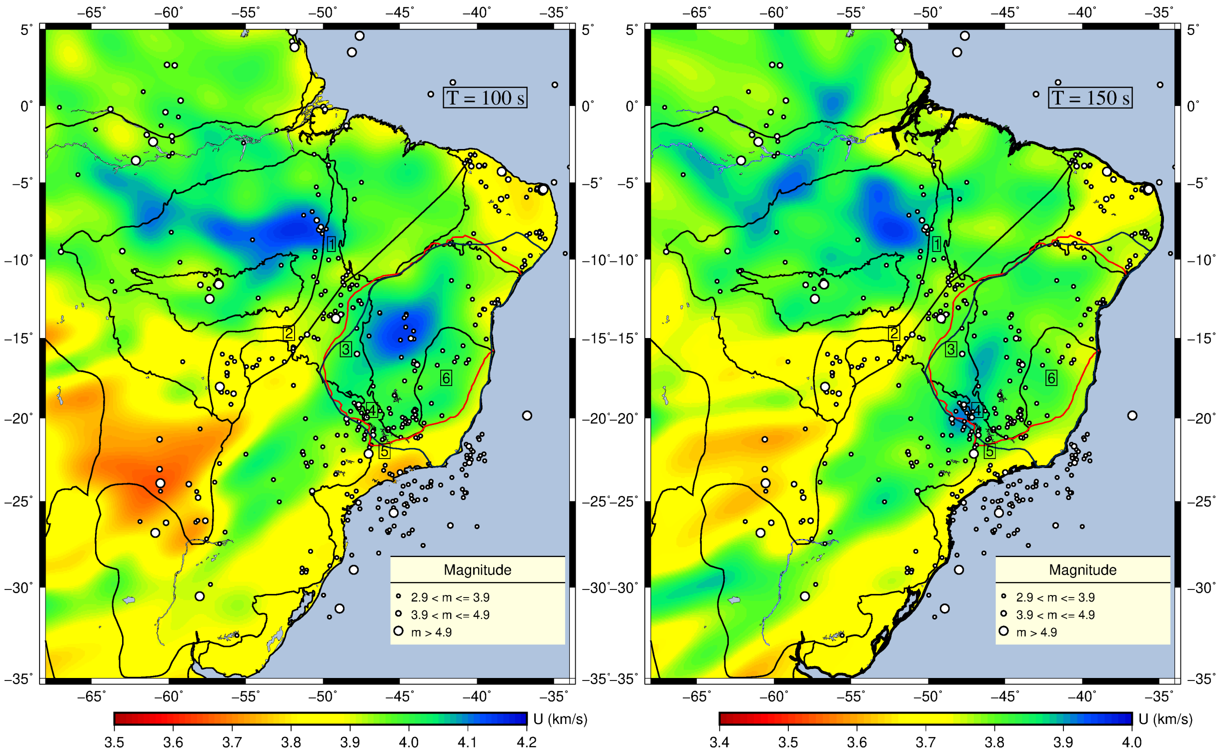

(a) (b)

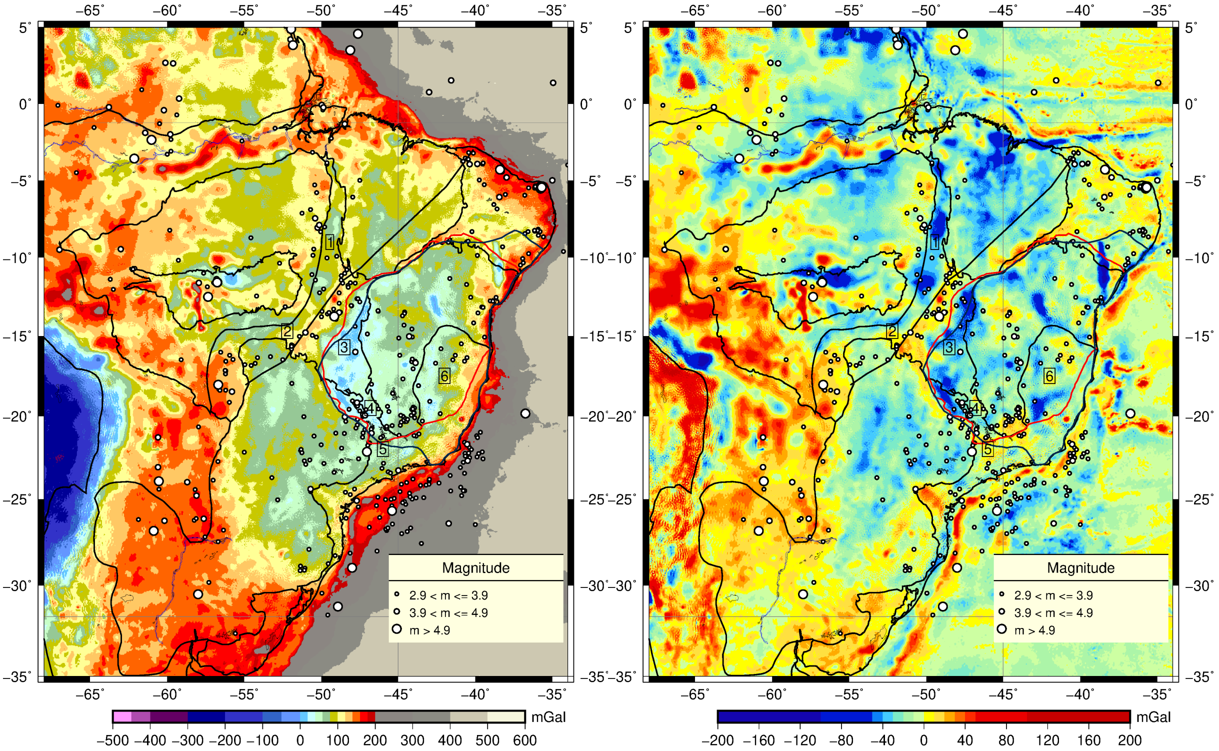

(c) (d)

Figure 5.10: a) 100 s period map; b) 150 s map; c) Gravity Bouguer anomaly map; d) Gravity isostatic anomaly map. All plots are overlaid by white circles representing the uniformized intraplate seismicity of Brazil, from 1922 to 2013. References: 1 - Araguaia Fold Belt, 2 - Paraguay Fold Belt, 3 - Northern Brasília Fold Belt, 4 - Southern Brasília Fold Belt, 5 - Ribeira Fold Belt, 6 - Araçuaí Fold Belt. Red and blue contours are limits for the São Francisco Paleocontinental Block, proposed by this work and by Rocha et al. (2019b), respectively. Black contours are the geotectonic features of Figure 5.1.

By comparing intraplate seismicity distribution in central Brazil with P-wave tomography results, Assumpção et al. (2004) noted a correlation between epicenter concentrations and low P-wave velocity anomalies. They suggested that those low-velocity anomalies are related to regions of thin lithosphere, where a hotter geotherm causes stress concentrations in the upper crust, which partially explains high seismicity in mid-plate areas. Azevedo et al. (2015) used data from more stations within the Tocantins Province to achieve a higher resolution model and confirmed the low-velocity pattern around the GTSZ. Assumpção and Sacek (2013) have shown that flexure effects could cause stresses of the order of 100 MPa, which is enough to lead to earthquakes. However, as pointed out by Rocha et al. (2016), the regional stress field over regions of thin lithosphere can also be an important component to generate the seismicity in central Brazil.

Our 100 s period image derived from surface wave dispersion measurements (Figure 5.10a) shows a low velocity trend in the Tocantins Province, roughly parallel to the TBL, consistent with the results obtained from P-wave tomography of Assumpção et al. (2004), Azevedo et al. (2015) and Rocha et al. (2016), interpreted as lithospheric thinning. Except for diffuse seismicity, especially within the São Francisco Craton, our results reveal that most of the intraplate seismicity of the South American Platform is associated with low-velocity anomalies, expanding thus the previous results in central Brazil to new areas.

We observe that Pantanal Basin and Borborema Province, two of the most seismically active areas in Brazil (e.g., Assumpção and Suárez, 1988; Takeya et al., 1989; Bezerra et al., 2011; Dias et al., 2016), are dominated by low velocity anomalies, which could also indicate zones of crustal weakness due to ascension of the asthenosphere, and consequently lithospheric thinning. The low-velocity in the Pantanal Basin extends southward, to parts of the Paraná and Chaco-Paraná Basins, where some earthquakes are also observed. Note that the number of earthquakes is drastically reduced in the region of the Paraná Basin where a high-velocity anomaly is observed, possibly associated with the Paranapanema Block, an old and more rigid lithospheric block beneath the sediment cover of the basin.

In the Mantiqueira Province, several earthquakes occur within the Ribeira Fold Belt region, associated with a low-velocity anomaly, while the Araçuaí Fold Belt presents a high-velocity anomaly and is practically aseismic. We interpret that the lithosphere beneath the Araçuaí Belt is more rigid, part of an older São Francisco Paleocontinental Block (SFPB, see next section) (Rocha et al., 2019b).

The region of the Parnaíba Basin is almost aseismic. Our results show moderate to high velocity anomalies in this basin, which seems to be consistent with a stable cratonic nucleus proposal (e.g., Cordani et al., 1984; Castro et al., 2014). Also, the high-velocity anomaly in the NE portion of the Parnaíba Basin appears to be related to the São Luís Craton, whose area in South America is relatively small.

Another important mid-plate seismic zone in South America is located in central-northern Parecis Basin, in the Porto dos Gaúchos Seismic Zone (PGSZ, see Barros et al. (2009)) and a small-sized low-velocity anomaly is also observed in this region. Besides low-velocity anomalies, the regions of high intraplate seismicity are also generally accompanied by high Bouguer and isostatic anomalies (Figures 5.10c and 5.10d) indicating that excess masses may be an important factor to explain intraplate seismicity as well.

5.7.2 São Francisco Paleocontinental Block

Located in eastern Brazil, the São Francisco Craton is an important component of the extra-Amazonian Domain of the South American Platform. This domain consists of several Archean and Paleoproterozoic cratonic nuclei generally smaller than the ones found in the Amazonian Domain, and amalgamated by fold belts (Brito Neves and Fuck, 2014). There is an understanding that the São Francisco Craton was part of a stable syn-Brasiliano paleocontinental plate, the São Francisco-Congo-Kasai-Angola (e.g., Brito Neves and Fuck, 2013). According to Brito Neves and Fuck (2013), the borders of the extra-Amazonian syn-Brasiliano cratons underwent reworking tectonic-thermal processes that resulted in descratonization, and therefore the limits of the cratons, as observed today, are probably only a portion of their original extent.

Analyses of geophysical data led to a hypothesis that at lithospheric depths the boundary of the São Francisco Craton is extended westward of its surface limits, beneath the northern Brasília Fold Belt (see Assumpção et al. (2017) for a review of the lithospheric studies concerning the São Francisco Craton). This is consistent with both previous body (e.g., Rocha et al., 2011; Azevedo et al., 2015; Azevedo, 2017, Rocha et al., 2019b) and surface (e.g., Feng et al., 2004; Feng et al., 2007) wave tomography results and with a deep refraction line (Soares et al., 2006). This suggests that the São Francisco Craton is included in a larger block named São Francisco Paleocontinental Block (SFPB), which is a part of the São Francisco-Congo-Kasai-Angola Plate.

The basement of the São Francisco Craton is exposed across the Atlantic Shield, whose signature is fast velocities in the 10 and 15 s period images. Those high velocities are also present across the neighboring Mantiqueira, Tocantins and Borborema Neoproterozoic Provinces, in which the basement is exposed as well. High velocities are observed as period increases, in 50, 100 and 150 s maps, consistent with a lithosphere relatively stable and cold. Due to the qualitative nature of our interpretation, we are not able to quantitatively estimate the depth of the cratonic root of the São Francisco Craton.

In the 100 and 150 s maps, high velocities of the São Francisco Craton are extended westward toward the Tocantins Province and eastward toward the Mantiqueira Province, consistent with the P-wave tomographic model of Rocha et al. (2019b), except that in their model low velocities are found beneath southern Brasília Fold Belt, southwestern to the São Francisco Craton (see number 4 on Figure 5.10). Based on our 100 and 150 s period maps and gravity anomalies (Bouguer and isostatic) from the Earth global gravity model WGM2012 (Bonvalot et al., 2012), we propose limits for the SFPB, represented by the red contours in Figure 5.10. The geometry of the SFPB proposed here and the one proposed by Rocha et al. (2019b) based on body wave tomography (blue contour in Figure 5.10) are very similar, except for a small area in the Mantiqueira and Borborema Provinces. Therefore, our study indicates further evidence for the existence of this paleocontinental block.

When compared to the São Francisco Craton, the limits of the SFPB are extended eastward toward the Araçuaí Fold Belt, westward beneath the northern Brasília Fold Belt and southwestern beneath southern Brasília Belt, crossing the surface bounds of the Paraná Basin. Although our tomographic maps don't clearly resolve the SFPB from the Paranapanema Block beneath Paraná Basin, this limit is indicated by low gravity anomalies.

5.7.3 Amazonian Craton

The Amazonian Craton is included in the pre-Tonian Amazonian Domain, N-NW of the South American Platform, which is characterized by Archean nuclei larger than the ones in the extra-Amazonian Domain, circumscribed by fold belts from Paleo- and Mesoproterozoic times (Brito Neves and Fuck, 2014). Due to a dense forest cover, the Amazonian Craton is one of the least known Precambrian areas in the world, and therefore geophysical studies play an important role to obtain information concerning it.

In our results, the Amazonian Craton is generally represented by high velocities in every map, consistent with older and relatively stable rocks. In the short period maps, the areas of exposed basement present high velocities, while the basins - Amazonas, Solimões, Marajó, and Parecis - are characterized by low-velocity anomalies. Note that even the Parecis Basin, with a rather thin sedimentary cover (see Table 5.1), was reasonably distinguished from the surrounding exposed basement, especially in the 15 s map (Figure 5.9b)

At lithospheric depths (100 and 150 s maps), the highest velocities beneath the Amazonian Craton are found across its northeastern portion, which is consistent with previous surface wave tomography studies (Heintz et al., 2005; Feng et al., 2007) and correlates with the oldest geochronological provinces; indeed, the youngest province of the Amazonian Craton, Sunsas, located on its western side, presents the lowest velocities of the craton. Figure 5.11 shows our 100 and 150 s period maps overlaid by the geochronological provinces of the Amazonian Craton, proposed by Santos (2003); Schobbenhaus and

Brito Neves (2003). Heintz et al. (2005) found velocities beneath the Amazon Basin to be slightly slower than beneath the shields, while the model of Feng et al. (2007) did not favor such behavior. Our model is more compatible with the one of Feng et al. (2007), where velocities beneath the basin are similar to the shields.

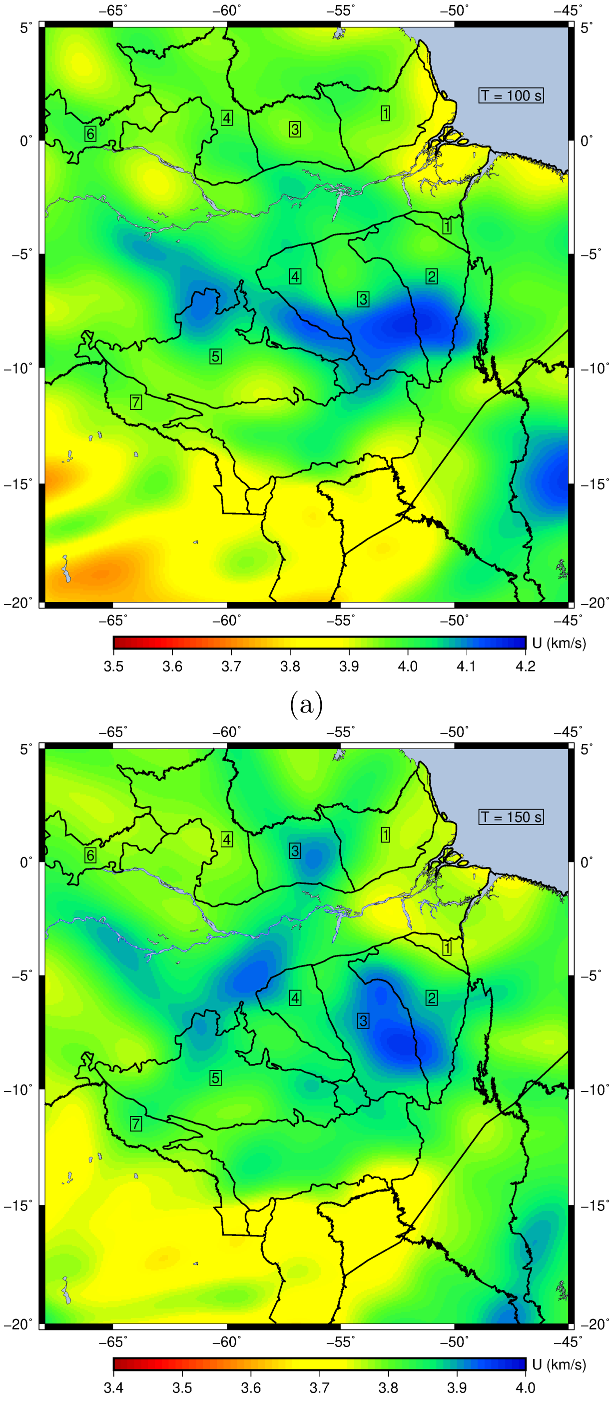

(a)

(b)

Figure 5.11: Geochronological provinces of the Amazonian Craton proposed by the Brazilian Geological Survey overlaying the a) 100 s and b) 150 s tomographic maps. Provinces: 1 - Transamazonas, 2 - Carajás, 3 - Amazônia Central, 4 - Tapajós-Parima, 5 - Rondônia-Juruena, 6 - Rio Negro, 7 - Sunsás.

Such as for the São Francisco Craton, it was not possible to estimate the depth of the cratonic roots of the Amazonian Craton. However, the 150 s image seems to indicate deeper cratonic roots for the Amazonian Craton compared to the São Francisco. Previous studies propose different depths for the cratonic roots of both cratons (Table 5.2), and the value proposed by Costa (2018) seems to be more consistent with our results.

Reference	**Amazonian (km)**	**São Francisco (km)**
Heintz et al. (2005)	200	200
Feng et al. (2007)	200	160
Rocha et al. (2011)	-	200
Azevedo (2017)	-	250
Costa (2018)	250	-

Table 5.2: Maximum depth of the roots of the Amazonian and São Francisco Cratons, according to several authors.

5.7.4 Paranapanema Block and Río de la Plata Craton

Located in central-southeastern South America, the Paraná Basin is a large intracratonic basin, with an area of approximately 1200000 km^2. As emphasized by Table 5.1, the sediment cover of this basin can reach thicknesses of 7 km, and this is reflected in our short period maps, where low velocities are observed for the region of the Paraná, Chaco-Paraná and Pantanal Basins.

Paraná Basin is underlain by a complex orogen system of the Brasiliano collage, and there is still debate concerning whether its basement is composed of a single block or by fragmented blocks. Based on rock samples from deep boreholes, early proposals for a stable nucleus beneath the Paraná Basin were provided by Cordani et al. (1984) and Brito Neves et al. (1984). Milani and Ramos (1998), however, proposed a mosaic of fragmented cratonic rocks surrounded by mobile belts, which seems to be sustained by a study of Julià et al. (2008) using receiver function and Rayleigh wave dispersion. A single block, named Paranapanema Block, was proposed by Mantovani et al. (2005) as the Paraná Basin basement, derived from a high gravity anomaly.

The Chaco-Paraná Basin occupies an area of approximately 500000 km ^{2} and is located to the southwest of the Paraná Basin, with a sedimentary cover thickness of about 5 km. The basement beneath the Chaco-Paraná is formed of the Río de la Plata Craton, whose bounds are still a matter of debate (e.g., Rapela et al., 2007; Oyhantçabal et al., 2010; Rapela et al., 2011; Dragone et al., 2017). Figure 5.12 shows the limits of the Paranapanema Block and Río de la Plata Craton, as proposed by several authors, overlaying the 100 (Figure 5.12a) and 150 s (Figure 5.12b) tomographic maps. A boundary proposal for the Paranapanema Block based on our result is also shown as dark purple contours.

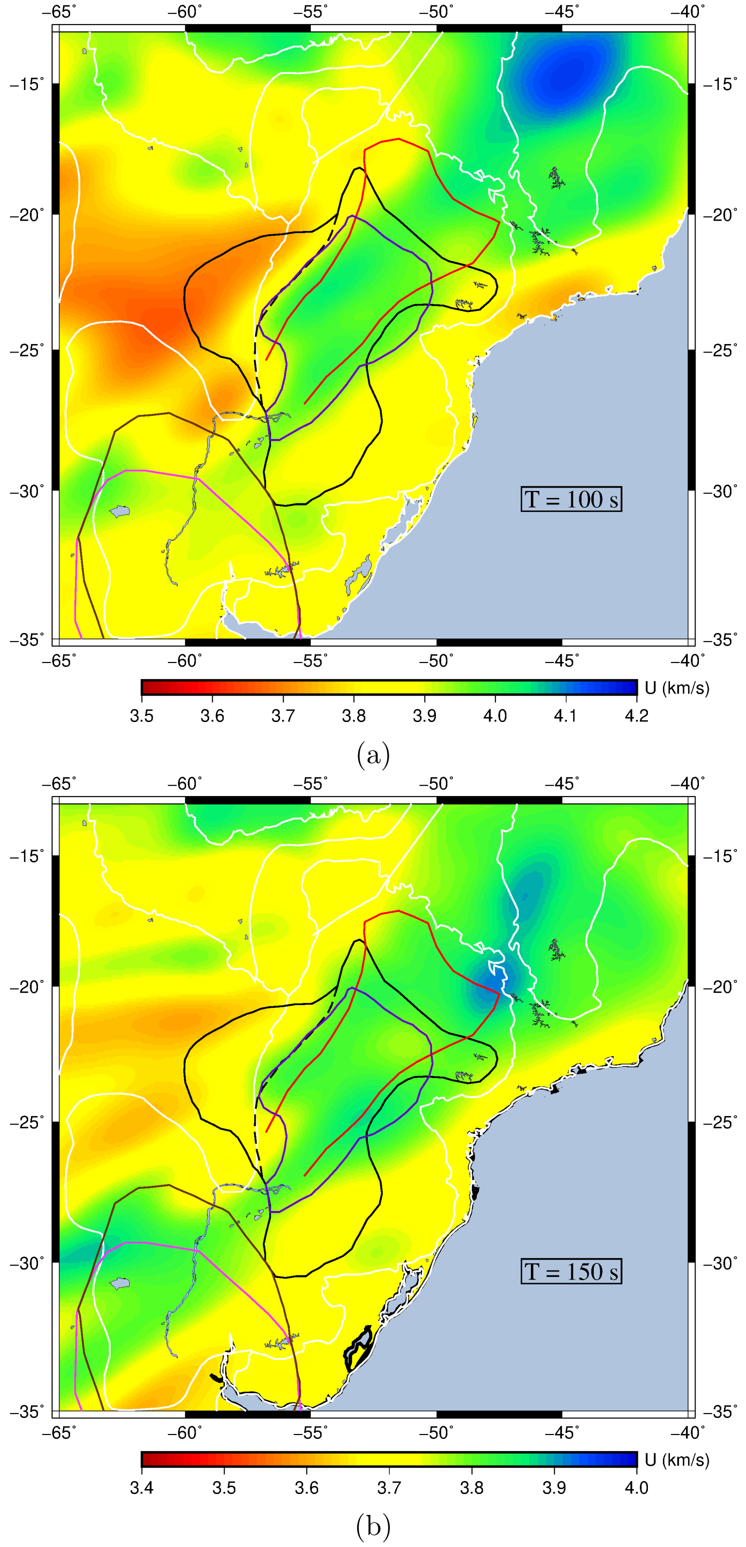

Figure 5.12: Limits for the Paranapanema Block and Río de la Plata Craton overlaying the a) 100 s and b) 150 s tomographic maps. Paranapanema Block in continuous red line according to Mantovani et al. (2005) and in black continuous line according to Rocha et al. (2019a); the dashed black line represents an inferred limit between Paranapanema (on the right) and Rio Apa (on the left) blocks in the proposal of Rocha et al. (2019a). Dark purple contours are the limits of the Paranapanema Block proposed by our study. Río de la Plata Craton according to: (i) Rapela et al. (2011) (continuous brown line) and (ii) Oyhantçabal et al. (2010) (continuous pink line). White lines are the geotectonic features of Figure 5.1.

From Figure 5.12, a single block interpretation for the limits of the Paranapanema

Block seems to be more consistent than a fragmented mosaic of blocks, at least at lithospheric depths. Our proposal for the limits of the Paranapanema Block is in general agreement with the models proposed by Mantovani et al. (2005) and Rocha et al. (2019a). This latter study delimited the Paranapanema Block based on teleseismic P-wave tomography, and the dashed black line in Figure 5.12 represents an inferred limit between the Paranapanema Block on the right and the Rio Apa (to the south of the Pantanal Basin) Block on the left. This limit is consistent with our tomographic image, but we found no high-velocity anomaly that could be related to the Rio Apa Block; this region is entirely composed of low velocities. This is probably caused by the lower resolution of long-period surface waves since the Rio Apa Block has small geometrical dimensions. It is also noteworthy that the model of Rocha et al. (2019a) is inferred from a P-wave velocity anomaly at 200 km, while our 100 s map samples mainly shallower depths (around 100 km depth, see Figure 5.8), which could partially explain the discrepancies between both models.

Our tomographic map presents some high-velocity anomalies in the region of the Río de la Prata Craton, but the lack of stations in this region decreases the resolution and prevents any further interpretation concerning the geometry of this craton.

5.8 Conclusions

Deployment of new seismic stations by the Brazilian Seismographic Network and other temporary projects such as the Pantanal, Chaco and Paraná structural studies network has greatly improved the coverage in the South American Platform, allowing an ever-increasing resolution of tomographic models of deep structure underneath the continent. We used data from 282 receivers to construct surface wave tomography maps for several periods, based on inversion of dispersion curves, obtaining, to our knowledge, the best path coverage in a surface wave study to date. Inversion of this data through a combination of FMM to solve the forward step with a subspace method to solve the inverse step provides a stable and robust way to estimate group velocity lateral variation maps, in which the nonlinearity of the problem is taken into account for iteratively.

A great correlation between areas of exposed basement and high-velocity anomalies, and between sedimentary basins (including thin sedimentary basins, such as Parecis Basin) and low-velocity anomalies is observed in our short period maps, namely 10 and 15 s. The sensitivity kernel shows that 50 s period waves are mostly affected by crustal and upper mantle structure, and we observe that the 50 s map distinguishes the Andes, where a thick crust is found, from the rest of the continent.

At lithospheric depths, our 100 s map presents several interesting characteristics. A low-velocity belt is revealed across central Brazil, roughly correlating with TBL. Previous studies based on P-wave tomography imaged this feature (e.g. Assumpção et al., 2004; Azevedo et al., 2015; Rocha et al., 2016), finding low velocity anomalies as well, and proposing that the high intraplate seismicity in this region (GTSZ) is related to lithospheric thinning. Our results in the GTSZ are consistent with this hypothesis, in which stresses are concentrated in the upper crust due to a hotter geotherm caused by ascension of the asthenosphere. The 100 s map also exhibits this behavior for other areas of the South American Platform, including the Borborema Province, the Porto dos Gaúchos Seismic Zone, and the Pantanal Basin, where high Bouguer and isostatic anomalies are also generally observed.

Due to their cold and stable character, cratonic areas (or at least more rigid portions of the lithosphere) usually present high-velocity anomalies in tomographic studies. This is the case in our results for the São Francisco and Amazon Cratons and the Paranapanema Block. A hypothesis concerning the São Francisco Craton (e.g., Alkmim et al., 1993) is that, at depth, its limits are extended westward, underneath the Northern Brasília belt. This hypothesis is in general agreement with P-wave tomography (Rocha et al., 2019b) and with a deep refraction line by Soares et al. (2006). Our 100 s and 150 s maps also show high velocities in this region, supporting this hypothesis. These maps, together with satellite Bouguer and isostatic gravity anomalies, allowed us to propose new boundaries for the SFPB, that comprises the São Francisco Craton, part of the Northern Brasília belt, but also parts of Southern Brasília and Araçuaí fold belts. The limits of the SFPB suggested by us are in general agreement with the ones proposed by Rocha et al. (2019b).

For the Amazonian Craton, the highest velocities seem to be correlated with the oldest geochronological provinces, while the youngest Sunsas Province, in its western portion, has lower velocities. For the basement of the Paraná Basin, models consisting of a single block or a mosaic of fragmented blocks have been proposed (e.g., Cordani et al., 1984; Milani and Ramos, 1998; Mantovani et al., 2005). Our results indicate that, at least at lithospheric depths, a single block interpretation seems more likely. A high-velocity anomaly in this region is in general agreement with the Paranapanema models proposed by Mantovani et al. (2005) and Rocha et al. (2019a). For the basement of the Chaco-Paraná Basin, that is, the Río de la Plata Craton, although high-velocity anomalies were mapped in this region, it is still too early to infer any interpretations, due to the lack of stations.

References

Aki, K., Christoffersson, A., and Husebye, E. S. (1977). Determination of the three-dimensional seismic structure of the lithosphere. *Journal of Geophysical Research*, 82(2):277–296. 1, 14, 29

Aki, K. and Lee, W. (1976). Determination of three-dimensional velocity anomalies under a seismic array using first p arrival times from local earthquakes: 1. a homogeneous initial model. *Journal of Geophysical research*, 81(23):4381–4399. 14

Alkmim, F., Brito Neves, B., and Castro, A. (1993). Arcabouço tectônico do cráton do são francisco: uma revisão. *O Cráton do São Francisco. DOMINGUEZ, JML & MISI, A.(ed), SBG-Núcleo BA/SE*, pages 45–62. 15, 40, 67

Almeida, F. F. M. d., Brito Neves, B. B. d., and Carneiro, C. D. R. (2000). The origin and evolution of the south american platform. *Earth-Science Reviews*, 50(1-2):77–111. 3, 4, 40, 41, 42

Almeida, F. F. M. d., Hasui, Y., Brito Neves, B. B. d., and Fuck, R. A. (1977). Províncias estruturais brasileiras. *Simpósio de Geologia do Nordeste*, 8(1977):363–391. 5, 42

Almeida, F. F. M. d., Hasui, Y., Brito Neves, B. B. d., and Fuck, R. A. (1981). Brazilian structural provinces: an introduction. *Earth-Science Reviews*, 17(1-2):1–29. vii, 4, 5, 42

An, M. and Assumpção, M. S. (2004). Multi-objective inversion of surface waves and receiver functions by competent genetic algorithm applied to the crustal structure of the parana basin, se brazil. *Geophysical Research Letters*, 31(5). 14

Anderson, D. L. (1967). Latest information from seismic observations. 13

Assumpção, M. and Araujo, M. (1993). Effect of the altiplano-puna plateau, south america, on the regional intraplate stresses. *Tectonophysics*, 221(3-4):475–496. 58

Assumpção, M., Azevedo, P. A., Rocha, M. P., and Bianchi, M. B. (2017). Lithospheric features of the são francisco craton. In *São Francisco Craton, Eastern Brazil*, pages 15–25. Springer. 61

Assumpção, M., James, D., and Snoke, A. (2002). Crustal thicknesses in se brazilian shield by receiver function analysis: Implications for isostatic compensation. *Journal of Geophysical Research: Solid Earth*, 107(B1). 15

Assumpção, M. and Sacek, V. (2013). Intra-plate seismicity and flexural stresses in central brazil. *Geophysical Research Letters*, 40(3):487–491. 58, 60

Assumpção, M., Schimmel, M., Escalante, C., Roberto Barbosa, J., Rocha, M., and Barros, L. V. (2004). Intraplate seismicity in se brazil: stress concentration in lithospheric thin spots. *Geophysical Journal International*, 159(1):390–399. 17, 40, 59, 60, 66

Assumpção, M. and Suárez, G. (1988). Source mechanisms of moderate-size earthquakes and stress orientation in mid-plate south america. *Geophysical Journal International*, 92(2):253–267. 60

Aster, R. C., Borchers, B., and Thurber, C. H. (2019). *Parameter estimation and inverse problems*. Elsevier, 3 edition. 28

Azevedo, P. A. d. (2017). *Estudo do manto superior sob o Brasil utilizando tomografia sísmica de tempo de percurso com ondas P*. Phd thesis, Universidade de Brasília. 41, 61, 64

Azevedo, P. A. d., Rocha, M. P., Soares, J. E. P., and Fuck, R. A. (2015). Thin lithosphere between the amazonian and são francisco cratons, in central brazil, revealed by seismic p-wave tomography. *Geophysical Journal International*, 201(1):61–69. vii, 16, 19, 40, 60, 61, 66

Backus, G. and Gilbert, F. (1970). Uniqueness in the inversion of inaccurate gross earth data. *Philosophical Transactions of the Royal Society of London. Series A, Mathematical and Physical Sciences*, 266(1173):123–192. 1

Backus, G. E. and Gilbert, J. (1967). Numerical applications of a formalism for geophysical inverse problems. *Geophysical Journal International*, 13(1-3):247–276. 1

Barazangi, M. and Isacks, B. L. (1976). Spatial distribution of earthquakes and subduction of the nazca plate beneath south america. *Geology*, 4(11):686–692. 6

Barazangi, M. and Isacks, B. L. (1979). Subduction of the nazca plate beneath peru: evidence from spatial distribution of earthquakes. *Geophysical Journal International*, 57(3):537–555. 6

Barros, L. V., Assumpção, M., Quintero, R., and Caixeta, D. (2009). The intraplate porto dos gaúchos seismic zone in the amazon craton—brazil. *Tectonophysics*, 469(1-4):37–47. 61

Barros, L. V., Assumpção, M., Quintero, R., and Ferreira, V. M. (2011). Coda wave attenuation in the parecis basin, amazon craton, brazil: sensitivity to basement depth. *Journal of Seismology*, 15(2):391–409. 57

Beck, S. L., Zandt, G., Myers, S. C., Wallace, T. C., Silver, P. G., and Drake, L. (1996). Crustal-thickness variations in the central andes. *Geology*, 24(5):407–410. 15

Beyreuther, M., Barsch, R., Krischer, L., Megies, T., Behr, Y., and Wassermann, J. (2010). Obspy: A python toolbox for seismology. *Seismological Research Letters*, 81(3):530–533. 21

Bezerra, F. H., do Nascimento, A. F., Ferreira, J. M., Nogueira, F. C., Fuck, R. A., Neves, B. B. B., and Sousa, M. O. (2011). Review of active faults in the borborema province, intraplate south america—integration of seismological and paleoseismological data. *Tectonophysics*, 510(3-4):269–290. 60

Bhattacharya, S. (1983). Higher order accuracy in multiple filter technique. *Bulletin of the Seismological Society of America*, 73(5):1395–1406. 25, 46

Bianchi, M. B., Assumpção, M., Rocha, M. P., Carvalho, J. M., Azevedo, P. A., Fontes, S. L., Dias, F. L., Ferreira, J. M., Nascimento, A. F., Ferreira, M. V., et al. (2018). The brazilian seismographic network (rsbr): improving seismic monitoring in brazil. *Seismological Research Letters*, 89(2A):452–457. 2, 41, 45

Bonvalot, S., Balmino, G., Briais, A., Kuhn, M., Peyrefitte, A., Vales, N., and Sarrailh, M. (2012). World gravity map. *Bureau Gravimetrique International (BGI), Map, CGMW-BGI-CNES728, IRD, Paris*. 62

Braunmiller, J. and Nábělek, J. (1996). Geometry of continental normal faults: Seismological constraints. *Journal of Geophysical Research: Solid Earth*, 101(B2):3045–3052. 1

Brito Neves, B. B. d. and Fuck, R. A. (2013). Neoproterozoic evolution of the basement of the south-american platform. *Journal of South American Earth Sciences*, 47:72–89. 4, 42, 61

Brito Neves, B. B. d. and Fuck, R. A. (2014). The basement of the south american platform: Half laurentian (n-nw)+ half gondwanan (e-se) domains. *Precambrian Research*, 244:75–86. 5, 42, 61, 62

Brito Neves, B. B. d., Fuck, R. A., Cordani, U. G., and Thomaz Filho, A. (1984). Influence of basement structures on the evolution of the major sedimentary basins of brazil: a case of tectonic heritage. *Journal of Geodynamics*, 1(3-5):495–510. 64

Brito Neves, B. B. d., Fuck, R. A., and Pimentel, M. M. (2014). The brasiliano collage in south america: a review. *Brazilian Journal of Geology*, 44(3):493–518. 5, 42

Buske, S. and Kästner, U. (2004). Efficient and accurate computation of seismic traveltimes and amplitudes. *Geophysical Prospecting*, 52(4):313–322. 31

Cammarano, F., Goes, S., Vacher, P., and Giardini, D. (2003). Inferring upper-mantle temperatures from seismic velocities. *Physics of the Earth and Planetary Interiors*, 138(3-4):197–222. 58

Castro, D. L. d., Fuck, R. A., Phillips, J. D., Vidotti, R. M., Bezerra, F. H. R., and Dantas, E. L. (2014). Crustal structure beneath the paleozoic parnaíba basin revealed by airborne gravity and magnetic data, brazil. *Tectonophysics*, 614:128–145. 61

Cawood, P. A. (2005). Terra australis orogen: Rodinia breakup and development of the pacific and iapetus margins of gondwana during the neoproterozoic and paleozoic. *Earth-Science Reviews*, 69(3-4):249–279. 8, 44

Constable, S. C., Parker, R. L., and Constable, C. G. (1987). Occam's inversion: A practical algorithm for generating smooth models from electromagnetic sounding data. *Geophysics*, 52(3):289–300. 33

Cordani, U. G., Brito Neves, B. B. d., Fuck, R. A., Porto, R., Thomaz Filho, A., and Cunha, F. M. B. (1984). Estudo preliminar de integração do pré-cambriano com os eventos tectônicos das bacias sedimentares brasileiras. *Ciência. Técnica. Petróleo. Seção: Exploração de Petróleo*, (14):1–70. 61, 64, 67

Costa, I. S. L. (2018). Estrutura do manto continental sublitosférico do cráton amazônico por tomografia sísmica de múltiplas frequências. Mestrado, Universidade de Brasília. 64

Dewey, J. F. and Bird, J. M. (1970). Mountain belts and the new global tectonics. *Journal of Geophysical Research*, 75(14):2625–2647. 6, 44

Dias, F. L., Assumpção, M., Facincani, E. M., Franca, G. S., Assine, M. L., Paranhos Filho, A. C., and Gamarra, R. M. (2016). The 2009 earthquake, magnitude mb 4.8, in the pantanal wetlands, west-central brazil. *Anais da Academia Brasileira de Ciências*, 88(3):1253–1264. 57, 60

Dias, R. C., Julià, J., and Schimmel, M. (2015). Rayleigh-wave, group-velocity tomography of the borborema province, ne brazil, from ambient seismic noise. *Pure and Applied Geophysics*, 172(6):1429–1449. 16, 47, 57

Dragone, G. N., Ussami, N., Gimenez, M. E., Klinger, F. G. L., and Chaves, C. A. M. (2017). Western paraná suture/shear zone and the limits of rio apa, rio tebicuary and rio de la plata cratons from gravity data. *Precambrian Research*, 291:162–177. 64

Dziewonski, A., Bloch, S., and Landisman, M. (1969). A technique for the analysis of transient seismic signals. *Bulletin of the seismological Society of America*, 59(1):427–444. 25, 46

Dziewonski, A. M. and Anderson, D. L. (1981). Preliminary reference earth model. *Physics of the earth and planetary interiors*, 25(4):297–356. 14

Dziewonski, A. M., Hager, B. H., and O'Connell, R. J. (1977). Large-scale heterogeneities in the lower mantle. *Journal of Geophysical Research*, 82(2):239–255. 14

Ekström, G., Tromp, J., and Larson, E. W. (1997). Measurements and global models of surface wave propagation. *Journal of Geophysical Research: Solid Earth*, 102(B4):8137–8157. 14

Fang, H., Yao, H., Zhang, H., Huang, Y.-C., and van der Hilst, R. D. (2015). Direct inversion of surface wave dispersion for three-dimensional shallow crustal structure based on ray tracing: methodology and application. *Geophysical Journal International*, 201(3):1251–1263. 1

Fang, H., Zhang, H., Yao, H., Allam, A., Zigone, D., Ben-Zion, Y., Thurber, C., and van der Hilst, R. D. (2016). A new algorithm for three-dimensional joint inversion of body wave and surface wave data and its application to the southern california plate boundary region. *Journal of Geophysical Research: Solid Earth*, 121(5):3557–3569. 38, 53

Feng, M. and An, M. (2010). Lithospheric structure of the chinese mainland determined from joint inversion of regional and teleseismic rayleigh-wave group velocities. *Journal of Geophysical Research: Solid Earth*, 115(B6). 1, 26

Feng, M., Assumpçao, M., and Van der Lee, S. (2004). Group-velocity tomography and lithospheric s-velocity structure of the south american continent. *Physics of the Earth and Planetary Interiors*, 147(4):315–331. 1, 2, 15, 16, 17, 23, 26, 29, 41, 44, 45, 61

Feng, M., Van der Lee, S., and Assumpção, M. (2007). Upper mantle structure of south america from joint inversion of waveforms and fundamental mode group velocities of rayleigh waves. *Journal of Geophysical Research: Solid Earth*, 112(B4). vii, 1, 2, 16, 19, 23, 41, 44, 45, 61, 62, 63, 64

França, G. S. and Assumpção, M. (2004). Crustal structure of the ribeira fold belt, se brazil, derived from receiver functions. *Journal of South American Earth Sciences*, 16(8):743–758. 1

Gansser, A. (1973). Facts and theories on the andes: Twenty-sixth william smith lecture. *Journal of the Geological Society*, 129(2):93–131. 6, 43

Goes, S., Govers, R., Vacher, and P (2000). Shallow mantle temperatures under europe from p and s wave tomography. *Journal of Geophysical Research: Solid Earth*, 105(B5):11153–11169. 1, 58

Goutorbe, B., Coelho, D. L. d. O., and Drouet, S. (2015). Rayleigh wave group velocities at periods of 6–23 s across brazil from ambient noise tomography. *Geophysical Journal International*, 203(2):869–882. 16

Haned, A., Stutzmann, E., Schimmel, M., Kiselev, S., Davaille, A., and Yelles-Chaouche, A. (2015). Global tomography using seismic hum. *Geophysical Journal International*, 204(2):1222–1236. 14

Hasui, Y. (2012). Compartimentação geológica do brasil. *Geologia do Brasil. São Paulo: Beca*, pages 112–122. 4, 8, 42, 44

Heintz, M., Debayle, E., and Vauchez, A. (2005). Upper mantle structure of the south american continent and neighboring oceans from surface wave tomography. *Tectonophysics*, 406(1-2):115–139. vii, 1, 16, 19, 23, 41, 45, 62, 63, 64

Heit, B., Sodoudi, F., Yuan, X., Bianchi, M., and Kind, R. (2007). An s receiver function analysis of the lithospheric structure in south america. *Geophysical Research Letters*, 34(14). 1

Herrin, E. and Goforth, T. (1977). Phase-matched filters: application to the study of rayleigh waves. *Bulletin of the Seismological Society of America*, 67(5):1259–1275. 25, 46

Herrmann, R. and Ammon, C. (2002). Computer programs in seismology: Surface waves, receiver functions and crustal structure. *St. Louis University, St. Louis, MO*. 25, 46

Herrmann, R. B. (1973). Some aspects of band-pass filtering of surface waves. *Bulletin of the Seismological Society of America*, 63(2):663–671. 25

Herrmann, R. B. (2013). Computer programs in seismology: An evolving tool for instruction and research. *Seismological Research Letters*, 84(6):1081–1088. 25, 46

Humphreys, E. D. and Clayton, R. W. (1990). Tomographic image of the southern california mantle. *Journal of Geophysical Research: Solid Earth*, 95(B12):19725–19746. 29

James, D. E., Assumpçăo, M., Snoke, J. A., Ribotta, L. C., and Kuehnel, R. (1993). Seismic studies of continental lithosphere beneath se brazil. In *3rd International Congress of the Brazilian Geophysical Society*. 15

Johnston, A. C. (1989). The seismicity of 'stable continental interiors'. In *Earthquakes at North-Atlantic Passive Margins: Neotectonics and Postglacial Rebound*, pages 299–327. Springer. 58

Julià, J., Assumpção, M., and Rocha, M. (2008). Deep crustal structure of the parana basin from receiver functions and rayleigh-wave dispersion: Evidence for a fragmented cratonic root. *Journal of Geophysical Research: Solid Earth*, 113(B8). 64

Julian, B. R. and Gubbins, D. (1977). Three-dimensional seismic ray tracing. *Journal of Geophysics*, 43:95–113. 30

Kaban, M. K., Schwintzer, P., Artemieva, I. M., and Mooney, W. D. (2003). Density of the continental roots: compositional and thermal contributions. *Earth and Planetary Science Letters*, 209(1-2):53–69. 58

Kennett, B., Sambridge, M., and Williamson, P. (1988). Subspace methods for large inverse problems with multiple parameter classes. *Geophysical Journal International*, 94(2):237–247. 35, 49

Kennett, B. L., Engdahl, E., and Buland, R. (1995). Constraints on seismic velocities in the earth from traveltimes. *Geophysical Journal International*, 122(1):108–124. 13, 53

Khattri, K., Mithal, R., and Gaur, V. (1979). Pattern space of seismic anomalies associated with hydrocarbon deposits. *Geophysical Prospecting*, 27(2):339–359. 1

Krischer, L., Megies, T., Barsch, R., Beyreuther, M., Lecocq, T., Caudron, C., and Wassermann, J. (2015). Obspy: A bridge for seismology into the scientific python ecosystem. *Computational Science & Discovery*, 8(1):014003. 21

Laske, G. and Masters, G. (1996). Constraints on global phase velocity maps from long-period polarization data. *Journal of Geophysical Research: Solid Earth*, 101(B7):16059–16075. 14

Lay, T. and Wallace, T. C. (1995). *Modern global seismology*, volume 58. Elsevier. 9, 30

Lévěque, J.-J., Rivera, L., and Wittlinger, G. (1993). On the use of the checker-board test to assess the resolution of tomographic inversions. *Geophysical Journal International*, 115(1):313–318. 37, 53

Liu, K. H., Gao, S. S., Silver, P. G., and Zhang, Y. (2003). Mantle layering across central south america. *Journal of Geophysical Research: Solid Earth*, 108(B11). 1, 14, 40

Liu, Y., Liu, W., Song, R., and Bucknall, R. (2017). Predictive navigation of unmanned surface vehicles in a dynamic maritime environment when using the fast marching method. *International Journal of Adaptive Control and Signal Processing*, 31(4):464–488. 47

Mantovani, M. S. M., Quintas, M. C. L., Shukowsky, W., and Brito Neves, B. B. d. (2005). Delimitation of the paranapanema proterozoic block: a geophysical contribution. *Episodes*, 28(1):18–22. ix, 64, 65, 66, 67

Matsubara, M., Obara, K., and Kasahara, K. (2008). Three-dimensional p-and s-wave velocity structures beneath the japan islands obtained by high-density seismic stations by seismic tomography. *Tectonophysics*, 454(1-4):86–103. 1

Milani, E. J. and De Wit, M. (2008). Correlations between the classic paraná and cape–karoo sequences of south america and southern africa and their basin infills flanking the gondwanides: du toit revisited. *Geological Society, London, Special Publications*, 294(1):319–342. 57

Milani, E. J. and Ramos, V. A. (1998). Orogenias paleozóicas no domínio sul-ocidental do gondwana e os ciclos de subsidência da bacia do paraná. *Revista Brasileira de Geociências*, 28(4):473–484. 15, 40, 64, 67

Milani, E. J. and Zalan, P. V. (1999). An outline of the geology and petroleum systems of the paleozoic interior basins of south america. *Episodes-Newsmagazine of the International Union of Geological Sciences*, 22(3):199–205. 57

Nakanishi, I. and Anderson, D. L. (1983). Measurement of mantle wave velocities and inversion for lateral heterogeneity and anisotropy: 1. analysis of great circle phase velocities. *Journal of Geophysical Research: Solid Earth*, 88(B12):10267–10283. 12

Nakanishi, I. and Anderson, D. L. (1984). Measurements of mantle wave velocities and inversion for lateral heterogeneity and anisotropy—ii. analysis by the single-station method. *Geophysical Journal International*, 78(2):573–617. 12

Nataf, H.-C., Nakanishi, I., and Anderson, D. L. (1986). Measurements of mantle wave velocities and inversion for lateral heterogeneities and anisotropy: 3. inversion. *Journal of Geophysical Research: Solid Earth*, 91(B7):7261–7307. 12

Oyhantçabal, P., Siegesmund, S., and Wemmer, K. (2010). The río de la plata craton: a review of units, boundaries, ages and isotopic signature. *International Journal of Earth Sciences*, 100(2-3):201–220. ix, 64, 65

Pankhurst, R. J., Rapela, C. W., Loske, W., Márquez, M., and Fanning, C. (2003). Chronological study of the pre-permian basement rocks of southern patagonia. *Journal of South American Earth Sciences*, 16(1):27–44. 8, 44

Pasyanos, M. E., Walter, W. R., and Hazler, S. E. (2001). A surface wave dispersion study of the middle east and north africa for monitoring the comprehensive nuclear-test-ban treaty. *Pure and Applied Geophysics*, 158:1445–1474. 17

Pennington, W. D. (1981). Subduction of the eastern panama basin and seismotectonics of northwestern south america. *Journal of Geophysical Research: Solid Earth*, 86(B11):10753–10770. 6

Qin, F., Luo, Y., Olsen, K. B., Cai, W., and Schuster, G. T. (1992). Finite-difference solution of the eikonal equation along expanding wavefronts. *Geophysics*, 57(3):478–487. 30

Ramos, V. (1999). Plate tectonic setting of the andean cordillera. *Episodes*, 22:183–190. 6, 43, 44

Ramos, V. A. (2009). Anatomy and global context of the andes: Main geologic features and the andean orogenic cycle. *Backbone of the Americas: shallow subduction, Plateau Uplift, and Ridge and Terrane collision*, 204:31–65. vii, 6, 7, 43

Rapela, C. W., Fanning, C. M., Casquet, C., Pankhurst, R. J., Spalletti, L., Poiré, D., and Baldo, E. G. (2011). The rio de la plata craton and the adjoining pan-african/brasiliano terranes: their origins and incorporation into south-west gondwana. *Gondwana Research*, 20(4):673–690. ix, 64, 65

Rapela, C. W., Pankhurst, R. J., Casquet, C., Fanning, C., Baldo, E., González-Casado, J. M., Galindo, C., and Dahlquist, J. (2007). The río de la plata craton and the assembly of sw gondwana. *Earth-Science Reviews*, 83(1-2):49–82. 64

Rawlinson, N. (2005). Fmst: Fast marching surface tomography package–instructions. *Research School of Earth Sciences, Australian National University, Canberra*. 29, 47

Rawlinson, N., Fichtner, A., Sambridge, M., and Young, M. K. (2014). Seismic tomography and the assessment of uncertainty. In *Advances in Geophysics*, volume 55, pages 1–76. Elsevier. 32, 48

Rawlinson, N., Kennett, B., Vanacore, E., Glen, R., and Fishwick, S. (2011). The structure of the upper mantle beneath the delamerian and lachlan orogens from simultaneous inversion of multiple teleseismic datasets. *Gondwana Research*, 19(3):788–799. 1, 38, 53

Rawlinson, N. and Sambridge, M. (2003). Seismic traveltime tomography of the crust and lithosphere. *Advances in Geophysics*, 46:81–199. viii, 29, 30, 31, 34, 35, 48, 50

Rawlinson, N. and Sambridge, M. (2004a). Multiple reflection and transmission phases in complex layered media using a multistage fast marching method. *Geophysics*, 69(5):1338–1350. 47

Rawlinson, N. and Sambridge, M. (2004b). Wave front evolution in strongly heterogeneous layered media using the fast marching method. *Geophysical Journal International*, 156(3):631–647. 31, 47

Rawlinson, N. and Sambridge, M. (2005). The fast marching method: an effective tool for tomographic imaging and tracking multiple phases in complex layered media. *Exploration Geophysics*, 36(4):341–350. viii, 30, 31, 32, 47, 48

Ritzwoller, M. H., Shapiro, N. M., Barmin, M. P., and Levshin, A. L. (2002). Global surface wave diffraction tomography. *Journal of Geophysical Research: Solid Earth*, 107(B12):ESE–4. 14

Rivadeneyra-Vera, J. C., Bianchi, M., Assumpção, M., Cedraz, V., Julià, J., Rodríguez, M., Sánchez, L., Sánchez, G., Lopez-Murua, L., Fernandez, G., et al. (2019). An updated crustal thickness map of central south america based on receiver function measurements in the region of the chaco, pantanal, and paraná basins, southwestern brazil. *Journal of Geophysical Research: Solid Earth*. 57

Rocha, M., Assumpção, M., Affonso, G., Azevedo, P., and Bianchi, M. (2019a). Teleseismic p wave tomography beneath the pantanal, paraná, and chaco-paraná basins, se south america: Delimiting lithospheric blocks of the sw gondwana assemblage. *Journal of Geophysical Research: Solid Earth*, 124(7):7120–7137. iii, iv, ix, 39, 65, 66, 67

Rocha, M. P., Azevedo, P. A. d., Assumpção, M., Pedrosa-Soares, A. C., Fuck, R., and Von Huelsen, M. G. (2019b). Delimiting the neoproterozoic são francisco paleocontinental block with p-wave traveltime tomography. *Geophysical Journal International*, 219(1):633–644. ix, 60, 61, 62, 67

Rocha, M. P., Azevedo, P. A. d., Marotta, G. S., Schimmel, M., and Fuck, R. (2016). Causes of intraplate seismicity in central brazil from travel time seismic tomography. *Tectonophysics*, 680:1–7. 17, 40, 60, 66

Rocha, M. P., Schimmel, M., and Assumpção, M. (2011). Upper-mantle seismic structure beneath se and central brazil from p-and s-wave regional traveltime tomography. *Geophysical Journal International*, 184(1):268–286. vii, 1, 14, 19, 40, 61, 64

Romanowicz, B. (2002). Inversion of surface waves: a review. *International Geophysics Series*, 81(A):149–174. 12, 14, 41

Rosa, M. L., Collaço, B., Assumpção, M., Sabbione, N., and Sánchez, G. (2016). Thin crust beneath the chaco-paraná basin by surface-wave tomography. *Journal of South American Earth Sciences*, 66:1–14. 17, 45

Russo, R. and Silver, P. (1996). Cordillera formation, mantle dynamics, and the wilson cycle. *Geology*, 24(6):511–514. 15

Russo, R., VanDecar, J. C., Comte, D., Mocanu, V. I., Gallego, A., and Murdie, R. E. (2010). Subduction of the chile ridge: Upper mantle structure and flow. *Gsa Today*, 20(9):4–10. 16

Sambridge, M. (1990). Non-linear arrival time inversion: constraining velocity anomalies by seeking smooth models in 3-d. *Geophysical Journal International*, 102(3):653–677. 35, 49

Santos, J. d. (2003). Geotectônica dos escudos das guianas e brasil-central. *Geologia, Tectônica e Recusrsos Minerais do Brasil (texto, mapas & SIG). Brasília, Serviço Geológico do Brasil–CPRM/MME*, pages 169–226. 6, 42, 62

Santos, T. J. S. d., Fetter, A. H., and Neto, J. A. N. (2008). Comparisons between the northwestern borborema province, ne brazil, and the southwestern pharusian dahomey belt, sw central africa. *Geological Society, London, Special Publications*, 294(1):101–120. 5, 42

Saygin, E. and Kennett, B. (2012). Crustal structure of australia from ambient seismic noise tomography. *Journal of Geophysical Research: Solid Earth*, 117(B1). 1

Saygin, E. and Kennett, B. L. (2010). Ambient seismic noise tomography of australian continent. *Tectonophysics*, 481(1-4):116–125. 1, 29, 47, 58

Schimmel, M., Assumpçao, M., and VanDecar, J. (2003). Seismic velocity anomalies beneath se brazil from p and s wave travel time inversions. *Journal of Geophysical Research: Solid Earth*, 108(B4). 14, 40

Schobbenhaus, C. and Brito Neves, B. B. d. (2003). A geologia do brasil no contexto da plataforma sul-americana. *Geologia, Tectônica e Recursos Minerais do Brasil. Brasília, CPRM*, pages 5–25. 6, 42, 62

Schulte, S. M. and Mooney, W. D. (2005). An updated global earthquake catalogue for stable continental regions: reassessing the correlation with ancient rifts. *Geophysical Journal International*, 161(3):707–721. 58

Sethian, J. A. (1996). A fast marching level set method for monotonically advancing fronts. *Proceedings of the National Academy of Sciences*, 93(4):1591–1595. 31, 47

Sethian, J. A. and Popovici, A. M. (1999). 3-d traveltime computation using the fast marching method. *Geophysics*, 64(2):516–523. 31, 47

Shapiro, N. and Singh, S. (1999). A systematic error in estimating surface-wave group-velocity dispersion curves and a procedure for its correction. *Bulletin of the Seismological Society of America*, 89(4):1138–1142. 25, 46

Shearer, P. M. (2009). *Introduction to seismology*. Cambridge university press. vii, 8, 9, 10, 12, 14

Sigloch, K. (2011). Mantle provinces under north america from multifrequency p wave tomography. *Geochemistry, Geophysics, Geosystems*, 12(2). 1

Silveira, G. and Stutzmann, E. (2002). Anisotropic tomography of the atlantic ocean. *Physics of the Earth and Planetary Interiors*, 132(4):237–248. 15

Silveira, G., Stutzmann, E., Griot, D.-A., Montagner, J.-P., and Victor, L. M. (1998). Anisotropic tomography of the atlantic ocean from rayleigh surface waves. *Physics of the Earth and Planetary Interiors*, 106(3-4):257–273. 1, 15, 41

Snoke, J. A. and James, D. E. (1997). Lithospheric structure of the chaco and paraná basins of south america from surface-wave inversion. *Journal of Geophysical Research: Solid Earth*, 102(B2):2939–2951. 12, 14

Soares, J. E., Berrocal, J., Fuck, R. A., Mooney, W. D., and Ventura, D. B. (2006). Seismic characteristics of central brazil crust and upper mantle: a deep seismic refraction study. *Journal of Geophysical Research: Solid Earth*, 111(B12). 61, 67

Stein, S. and Wysession, M. (2003). An introduction to seismology. *Earthquakes, and Earth*. vii, 9, 10, 11

Takeya, M., Ferreira, J. M., Pearce, R. G., Assumpção, M., Costa, J. M., and Sophia, C. M. (1989). The 1986–1988 intraplate earthquake sequence near joão câmara, northeast brazil—evolution of seismicity. *Tectonophysics*, 167(2-4):117–131. 60

Talwani, P. and Rajendran, K. (1991). Some seismological and geometric features of intraplate earthquakes. *Tectonophysics*, 186(1-2):19–41. 58

Thurber, C. H. (1983). Earthquake locations and three-dimensional crustal structure in the coyote lake area, central california. *Journal of Geophysical Research: Solid Earth*, 88(B10):8226–8236. 29

Toksöz, M. N., Chinnery, M. A., and Anderson, D. L. (1967). Inhomogeneities in the earth's mantle. *Geophysical Journal International*, 13(1-3):31–59. 13

Trampert, J., Vacher, P., and Vlaar, N. (2001). Sensitivities of seismic velocities to temperature, pressure and composition in the lower mantle. *Physics of the Earth and Planetary Interiors*, 124(3-4):255–267. 58

Trampert, J. and Woodhouse, J. H. (1995). Global phase velocity maps of love and rayleigh waves between 40 and 150 seconds. *Geophysical Journal International*, 122(2):675–690. 14

Van der Lee, S., James, D., and Silver, P. (2001). Upper mantle s velocity structure of central and western south america. *Journal of Geophysical Research: Solid Earth*, 106(B12):30821–30834. 1, 15, 41

Van der Lee, S., James, D., and Silver, P. (2002). Correction to "upper mantle s velocity structure of central and western south america," by suzan van der lee, david james, and paul silver. *Journal of Geophysical Research: Solid Earth*, 107(B5):ESE–6. 15

Van der Lee, S. and Nolet, G. (1997). Upper mantle s velocity structure of north america. *Journal of Geophysical Research: Solid Earth*, 102(B10):22815–22838. 1, 15

VanDecar, J. C., James, D. E., and Assumpção, M. (1995). Seismic evidence for a fossil mantle plume beneath south america and implications for plate driving forces. *Nature*, 378(6552):25. 1, 14, 30, 40, 58

Vdovin, O., Rial, J. A., Levshin, A. L., and Ritzwoller, M. H. (1999). Group-velocity tomography of south america and the surrounding oceans. *Geophysical Journal International*, 136(2):324–340. vii, 1, 15, 19, 23, 41, 45

Vidale, J. (1988). Finite-difference calculation of travel times. *Bulletin of the Seismological Society of America*, 78(6):2062–2076. 30

Wiggins, R. A. (1972). The general linear inverse problem: Implication of surface waves and free oscillations for earth structure. *Reviews of Geophysics*, 10(1):251–285. 1

Woodhouse, J. and Dahlen, F. (1978). The effect of a general aspherical perturbation on the free oscillations of the earth. *Geophysical Journal International*, 53(2):335–354. 12

Yuan, H. and Romanowicz, B. (2010). Lithospheric layering in the north american craton. *Nature*, 466(7310):1063. 1

Zalán, P. V. and Matsuda, N. S. (2007). Bacia do marajó. *Boletim de Geociências da Petrobras*, 15(2):311–319. 57

Zhao, D. and Kanamori, H. (1992). P-wave image of the crust and uppermost mantle in southern california. *Geophysical research letters*, 19(23):2329–2332. 29

Zhou, Y., Nolet, G., Dahlen, F., and Laske, G. (2006). Global upper-mantle structure from finite-frequency surface-wave tomography. *Journal of Geophysical Research: Solid Earth*, 111(B4). 14

Zhu, H., Bozdağ, E., Peter, D., and Tromp, J. (2012). Structure of the european upper mantle revealed by adjoint tomography. *Nature Geoscience*, 5(7):493. 1

Zouaghi, T., Bédir, M., Abdallah, H., and Inoubli, M. H. (2009). Seismic sequence stratigraphy, basin structuring, and hydrocarbon implications of cretaceous deposits (albian–maastrichtian) in central tunisia. *Cretaceous Research*, 30(1):1–21. 1